A STUDY ON DIELECTRIC, WETTABILITY, AND MECHANICAL PROPERTIES OF Fe-Si BASED THIN FILMS AND DEVICES

NATTAKORN BORWORNPORNMETEE

A THESIS SUBMITTED IN PARTIAL FULFILLMENT OF THE REQUIREMENT FOR THE
DEGREE OF DOCTOR OF PHILOSOPHY IN APPLIED PHYSICS
DEPARTMENT OF PHYSICS SCHOOL OF SCIENCE
KING MONGKUT'S INSTITUTE OF TECHNOLOGY LADKRABANG
2025

KMITL-2025-SC-D-030-047

SCHOOL OF SCIENCE
KING MONGKUT'S INSTITUTE OF TECHNOLOGY LADKRABANG

Thesis Title	A Study on Dielectric, Wettability, and Mechanical Properties of Fe-Si based Thin Films and Devices
Student Name	Mr. Nattakorn Borwornpornmetee
Student ID	65056032
Degree	Doctor of Philosophy (Applied Physics)
Department	Physics
Year	2025
Thesis Advisor	Asst.Prof.Dr. Nathaporn Promros

Abstract

In this study, we explored the potential of iron silicide thin films (nanocrystalline $FeSi_2$ (NC-$FeSi_2$), orthorhombic β-$FeSi_2$, and ferromagnetic Fe_3Si) prepared by face-to-face target DC sputtering (FTDCS) as multifunctional materials. The electrical properties of n-β-$FeSi_2$/p-Si and n-NC-$FeSi_2$/p-Si heterojunctions were evaluated using impedance spectroscopy under various voltage and temperature conditions to clarify the charge transport properties, dielectric behavior, and detailed joining mechanism. The results suggest that these heterojunctions are suitable for storage and optoelectronic device applications. To improve the functionality, β-$FeSi_2$ and Fe_3Si thin films were subjected to rapid thermal annealing treatment to improve the crystallinity and mechanical hardness as well as to control the wettability. In addition, argon plasma etching with varying duration was applied to β-$FeSi_2$ films to induce a surface change from hydrophobic to hydrophilic, suggesting the possibility of self-cleaning applications. Through evaluation of various properties, including structure, morphology, electricity, mechanics, and wettability, it became clear that by appropriately controlling and modifying the Fe–Si compounds, they have great potential for application not only in optoelectronics but also as hard coating materials and self-cleaning surface materials.

Keywords : Fe-Si, heterojunctions, material modification, impedance, dielectric properties, wetting

Acknowledgement

This doctoral research project was successfully completed thanks to the warm support and expert guidance of my supervisor and thesis committee members. First of all, I would like to express my sincere gratitude to my supervisor, Asst.Prof.Dr. Nathaporn Promros, for his technical advice and dedicated guidance throughout the research. His guidance, which is well-versed in a wide range of fields, provided me with many suggestions in formulating my research question and establishing my methodology, greatly improving the quality of this research.

I would also like to express my deep gratitude to the thesis committee members Dr. Mati Horprathum, Assoc.Prof.Dr. Pattareya Damrongsak, Asst.Prof.Dr. Pisan Srirach, and Asst.Prof.Dr. Bhanupol Klongratog, for their time in reviewing my thesis and for their constructive comments and encouragement. Their advice has led to a more refined content of this thesis.

I would also like to express my sincere gratitude to Professor Tsuyoshi Yoshitake of Kyushu University for providing me with valuable research and training opportunities as part of this research project. His advice and support in writing the thesis was of great help to me in this research project. I would also like to thank Asst.Prof.Dr. Hiroshi Naragino, Dr. Phongsaphak Sittimart, Dr. Sreenath Mylo Valappil, and all the students in the Yoshitake Laboratory for their help in carrying out the experiments and daily research activities during my research stay in Japan.

I would like to convey my appreciations to Dr. Rungrueang Phatthanakun from Synchrotron Light Research Institute for his assistance on methodology and excellent research recommendations in improving the quality of my study. It was a privilege to have his assistance

I would also like to express my deep gratitude to the members of my laboratories at King Mongkut's Institute of Technology Ladkrabang for their great help in carrying out the experiments. In particular, I would like to express my gratitude to Dr. Peerasil Charoenyuenyaoa and Dr. Rawiwan Chaleawpong, who provided me with a lot of advice and support regarding the experimental procedures and methodology, as well as writing the thesis.

Mr. Nattakorn Borwornpornmetee

Table of contents

Table of contents (cont.)

Table of contents (cont.)

Page

Table of contents (cont.)

List of tables

List of figures

List of figures (cont.)

List of figures (cont.)

Figure **Page**

List of figures (cont.)

List of figures (cont.)

Figure **Page**

List of figures (cont.)

List of figures (cont.)

Figure **Page**

List of figures (cont.)

Figure **Page**

Chapter 1

Introduction

1.1 Signification of the research

The semiconductor phase of the iron disilicide ($FeSi_2$) compound with an orthorhombic (β) structure (β-$FeSi_2$) possesses desirable characteristics [1-3]. Its absorption coefficient value is over 10^5 cm^{-1} for the photon energy range that exceeds 1.2 eV, and it has an 0.76 eV indirect bandgap as well as an 0.85 eV direct bandgap for the optical transition [1-3]. Both of these are in adherence to the wavelength for optical telecommunications ranging from 1.3 to 1.5 microns [1-3]. Nanocrystalline $FeSi_2$ (NC-$FeSi_2$) with a 10 nm crystalline size or lower in diameter holds unique characteristics like those of β-$FeSi_2$ [4,5]. Both of Its optical band gap values are mostly identical to that of β-$FeSi_2$, while its absorption coefficient values greater compared to β-$FeSi_2$ [4,5]. Lattice parameter of ferromagnetic iron disilicide (Fe_3Si) features a slightly mismatch of +4.2% and -2.5% with Si and semiconducting phase β-$FeSi_2$ [6,7]. The Fe_3Si films have high spin polarization of 45% and high Curie temperature level of 840 K, while have a small magnetic coercivity of 7.5 Oe [6,7]. Furthermore, Fe_3Si films have a cubic DO_3 structure which also be able to considered as a Heusler type alloy (Fe_2FeSi) [6,7]. Fe_3Si also possesses good hardness and resistance to corrosion [8].

Heterojunctions consisted of n-type β-$FeSi_2$ or n-type NC- $FeSi_2$ on p-type Si have been created on p-type Si substrates using face-to-face targeted direct current sputtering (FTDCS) [9-11]. Although these structures have been initially evaluated for their electrical properties, including their applications in photodiodes and light detectors, detailed studies on the electrical behavior and mechanisms of the junction are limited [9-11]. Impedance spectroscopy is a prevailing technique to probe electrical phenomena within semiconductor devices, such as charge transport, carrier accumulation and recombination, junction response, and relaxation behavior [12-14]. With changing the applied voltage, it can be observed from the curves of real component of complex impedance (Z') and imaginary component (Z'') that the parallel resistance (R_p) decreases and the capacitance (C) increases, resulting from the shrinkage of the depletion layer [15-17]. Furthermore, increasing the voltage also increases the carrier density in the material [15-17]. This results in a higher direct current conductivity (σ_{DC}) [17,18]. The analysis of the dielectric properties also helps to understand the role of polarization in the electrochemical process of heterojunctions [19]. Therefore, the experiments under a varying voltage would be appropriate for acquiring response of impedance and related electrical properties to the biased signal with high precision. In addition to voltage, temperature is another important factor affecting the behavior of the device, as temperature can induce complex mechanisms, such as the change of the electrical conductivity, relaxation processes, carrier recombination, and the change of the interface state. In general, as the temperature increases, the total resistance and the grain boundary's resistance decrease due to the shrinkage of depletion layer [19-21]. However, at very high or low temperatures, the carrier density may decrease [19-21]. Therefore, to fully understand the behavior of heterojunctions under real operating conditions, it is necessary to analyze the impedance response under different voltages and temperatures, and systematically evaluate both electrical and dielectric properties [19-21]. To extend the knowledge on electrical mechanism of $FeSi_2$ heterojunctions and decide possible scenario for electronic applications, the impedance, conductivity, and dielectric properties under varying voltages and temperatures needed to be studied.

Moreover, both variations of $FeSi_2$ along with Fe_3Si were reported to possess hydrophobic surface [22-24]. They could be grown on to a wide array of substrates and also possess an extremely smooth surface while created from eco-friendly elements like Si and Fe that are ample on the planet earth [22-24]. Based on these properties, β-$FeSi_2$, NC-$FeSi_2$ and Fe_3Si is a potential contender for use as self-cleaning coating and hard coating material [22-24]. In the past, there are sparsely report on mechanical properties of Fe-Si namely Fe_3Si and a few of $FeSi_2$. T. Murakami et al [25] reported friction and wear properties of Fe–Si intermetallic compounds through sintering reveal their films possess microhardness around 8.5 GPa for Fe_3Si, 11.5 GPa for FeSi and 7 GPa for $FeSi_2$. T. Chang-bin et al [26] reported on Fe_3Si created by molten-salt which showed hardness for different derivative of Fe_3Si(2), Fe_3Si(2Cr13), and Fe_3Si(0Cr18Ni9) at 10.353 GPa, 10.944, and 12.763 GPa, respectively. S. Nakamura et al [27] reported on β-$FeSi_2$ created by FTDCS where obtained nano-indentation hardness is about 10 GPa moderately compared to various diamond-like carbon (DLC) films. However, there was limited study on wettability of Fe-Si material such as; Y.T. Chen et al [28] who study Fe_2Si films created by DC magnetron sputtering which have surface energy correlate with around 90°+ contact angle at 500 nm and the energy gradually decreased after annealing at 150 °C and 250 °. B. Nunes et al [29] studied $FeSi_2$ make from Fe implant into Si where the as implant films show contact angle around 70° and decrease to between 40-50° after annealed at 550 °C, 800 °C, 1000 °C. Hence, wettability along with mechanical of Fe-Si created through FTDCS as well as effect of heat on the films to unlock potential for multifunctional self-cleaning and hard coating applications on top of study on electrical properties for optoelectronic applications firstly were reported. P. Charoenyuenyao et al [30] The influence of conventional thermal annealing on the β-$FeSi_2$ film's surface created through FTDCS was then studied, revealing that the hydrophobic surface of unannealed β-$FeSi_2$ with contact angle of 93.25° possess lower contact angle of 91.60° after 200 °C annealing. Then, β-$FeSi_2$ turned into a hydrophilic surface with contact angle of 88.85° and 82.15° after annealing at 400 and 600 °C. P. Charoenyuenyao et al. [22] measured the contact angle of β-$FeSi_2$ thin films with deionized water under conditions of varying substrate temperatures to examine the wettability of the thin films. The contact angle was 91.15° at 525°C, and increased to 94.43° at 550°C, 99.48° at 600°C, and 103.80° at 660°C. In addition, P. Charoenyuenyao et al. [13] also reported that the β-$FeSi_2$ thin film formed at 525°C showed a nanohardness of 12.8 GPa and an elastic modulus of 191.0 GPa, which were significantly improved to 21.3 GPa and 248.7 GPa, respectively, by increasing the substrate temperature to 660°C. In general, materials with self-cleaning properties are known to be either superhydrophobic (contact angle 150° or more) or superhydrophilic (contact angle less than 10°) [31, 32]. On a superhydrophobic surface, water droplets roll off the surface, whereas on a superhydrophilic surface, water spreads and flows off the surface [31, 32]. Therefore, in order to give Fe-Si a self-cleaning function, the introduction of more advanced surface treatment techniques than conventional ones are required.

To unlock the possibility of Fe-Si for new applications, a usage of the optimal modification methods along with investigation into their wetting and mechanical properties is necessary. The conventional thermal annealing (CTA) has been reported to be able to improve the atomic mobility and rate of diffusion, resulting to an increase in nucleation density and uniform distribution of surface atoms [30,33]. Thus, it also affects the wettability and mechanical properties of the material [30,33]. Further, there is rapid thermal annealing (RTA) which provide added benefit of faster grain growth, more accurate control over time-temperature heating cycles, shorter non-gradient isothermal cycles, less chance of dopant infusion, and lower cost on top of as benefit that CTA already presented [34-36]. Building on previous studies showing the advantages of rapid thermal annealing (RTA), X. W. Lin et al. [37] demonstrated that cubic metallic $FeSi_2$ can be crystallized into the β-$FeSi_2$ phase by RTA treatment at 600 °C for only 20 seconds. This treatment promoted the diffusion of iron during rapid heating, improved the consistency and stability of the crystal structure, and also produced a uniform surface morphology. Such control of the microstructure and surface state is a key factor in improving mechanical hardness through internal stress and wettability through tuning the surface roughness. Meanwhile, P.-H. Wu et al. [38] investigated the mechanical properties of SiN thin films subjected to RTA treatment at different temperatures (400, 600, and 800 °C) for 10 minutes. The results showed that the hardness, Young's modulus, and residual stress could be significantly controlled with increasing temperature. These changes were probably caused by the gradual relaxation of the initially existing compressive stress by RTA and its transformation into tensile stress after treatment at higher temperatures. Y.-J. Chiu et al [39] reported on Characteristics of FePd alloy thin films deposited by magnetron sputtering. The RTA at 400 and 750 °C resulted in the noticeable increment of contact angle to 52 and 75° from origin of 20° for as-deposited FePd. However, the usage of RTA to the modify the wetting and mechanical traits for Fe-Si films for multifunction hard coatings with self-cleaning has not been reported up until now.

Another method among various techniques have been reported about the modification of physical characteristics for thin films, plasma etching has attracted particular attention because it can precisely control the interaction of ions with the material surface to tailor the material properties [23,24]. This process effectively improves the quality and performance of films by removing contaminants through interaction of plasma ion with bound particles present on the surface [23,24]. The results of plasma treatment are highly dependent on several process parameters, including the type of ionized gas used, electrical power, treatment time, and chamber pressure. Among these, Ar plasma is widely used, since it has the ability to physically roughen the surface and can also remove oxide films by breaking the bonds between material and oxygen atoms [23,24]. Such surface modification significantly improves the surface reactivity and functional performance of materials, making plasma etching an essential process technology in advanced materials engineering [23,24]. Ar plasma etching under increasing power can also turn the Fe-Si based surface into highly hydrophilic state at higher power as reported in the previous works [23,24]. N. Borwornpornmetee et al [23] reported the effect of microwave Ar plasma treatment under variation of its power on the physical features of the Fe_3Si films, where the hydrophobic condition of 101.70° for the original Fe_3Si layer turned into a hydrophilic surface of 67.05° contact angle after exposing to Ar etching. Next, N. Borwornpornmetee et al [24] reported the effect of microwave Ar plasma etching under different powers on the NC-$FeSi_2$ films which share the similar trend but can more effectively turn hydrophobic surface of 100.55° to highly hydrophilic of 35.65° rivaling less durable self-cleaning material like polymethyl methacrylate. However, the duration used to etch the sample with the plasma is also one of important factors for controlling the hydrophilicity of the material by controlling degree of interaction of ions [40]. According to the literature related to plasma surface modification, the time taken to etch the sample with the plasma is among the important factors for controlling the hydrophilicity of the material. Ru et al. [41] studied the effect of changing the time taken to etch Ar plasma on the properties of Polyvinyl Chloride (PVC) sheets. The findings reveal that PVC has hydrophobic wetting properties and a contact angle of more than 100°, which tends to decrease with increasing etching time, resulting in a decrease in hydrophilic groups such as carbon and chlorine, while the oxides become more hydrophilic, resulting in a rise in the surface free energy until the contact angle is less than 25° after eight minutes of etching. Zajíčková [42] studied the etching of a polycarbonate surface with Ar gas plasma and found that a longer etching time can increase the surface free energy and hydrophilicity from a hydrophilic surface of 70° to a superhydrophilic surface at a contact angle below 10°. Moreover, Ting et al. [40] studied the etching of an aluminum surface with Ar gas plasma at different etching times. They found that the plasma at 1000 W etching for 30 s could reduce the high hydrophilic contact angle from approximately 20° to approximately 13°, and when etched for a longer time of 10 minutes, the contact angle of 13° reduced to approximately 4°, resulting in a superhydrophilic surface. Using the above-mentioned approach, it can be concluded that changing the duration of plasma etching can reduce the contact angle down to the superhydrophilic level. From these results, alteration of time should significantly increase hydrophilicity of the films.

Consequentially, all films will be deposited onto Si wafers by FTDCS In this research to then perform impedance spectroscopy on the junctions created from NC-$FeSi_2$ and β-$FeSi_2$ films under different voltages and temperatures to further investigate their electrical characteristics, junction behaviors and mechanisms as response to working environment and deduct representative equivalent circuit and its parameters. More importantly, there might be possibility to adopt these heterojunction devices as storage devices based on electrical conductivities and dielectric properties that can be extracted from impedance. Then, RTA at different temperatures will be introduced to β-$FeSi_2$ and Fe_3Si films to enhance its mechanical properties and modify their wettability. Finally, the objective is to introduce the plasma etching process to β-$FeSi_2$ films using different etching durations to determine their surface for self-cleaning surface application. The crystalline structure, chemical composition, morphological properties, wettability, and mechanical properties of all as-deposited, RTA, and plasma-etched films will be provided. This research is aim to understand deeper about the NC-$FeSi_2$, β-$FeSi_2$ and Fe_3Si composites as well as unlock their potential to applied in several fields such as storage devices, self-cleaning, and hard coating materials.

1.2 Purposes of the study

1) To explore the impedance as well as permittivity and conductivity under varying temperatures for p-Si /n-β-$FeSi_2$ and p-Si/n-NC-$FeSi_2$ heterostructures created through FTDCS.
2) To study the surface wetting behavior and nanomechanical properties of β-$FeSi_2$, and Fe_3Si films created through FTDCS using RTA under different temperatures.
3) To study the surface wetting behavior and nanomechanical properties of β-$FeSi_2$ films created through FTDCS using microwave plasma etching under different times.

1.3 Scopes of the study

1) β-$FeSi_2$ films were created onto Si substrate through FTDCS at 600 °C substrate temperature, while NC-$FeSi_2$ and Fe_3Si films were created onto Si substrate at room temperature using FTDCS. Al-electrodes were deposited onto β-$FeSi_2$ and NC-$FeSi_2$ films, while Pd-electrodes were deposited onto Si side by radio-frequency sputtering to form completed heterojunction devices.
2) The impedances under board frequency of 20 Hz to 2 MHz in dark were performed under biased voltage of -1 to 0 V at ambient temperature then performed at 160-400 K under biased voltage of 0.01 V.
3) β-$FeSi_2$ and Fe_3Si films were annealed by RTA at different temperatures (200, 400, 600, and 800 °C) for 10 minutes.
4) β-$FeSi_2$ films were etched by plasma at varied times (5, 10, and 15 minutes) under 300 W power in Ar atmosphere.
5) The investigation on crystalline structure, chemical composition, morphological properties, wettability, and mechanical properties of all as-deposited, RTA, and plasma-etched films will be provided.

1.4 Research Organization

Table 1.1 Steps in research process

Research step	Academic year		
	2022	2023	2024
Research on study materials related to the research topic.	🟦	🟦	🟦
Learn about the fabrication process of β-$FeSi_2$, NC-$FeSi_2$, and Fe_3Si films onto Si by FTDCS.	🟦		
Examine the impedance profiles and simulate associated parameters at various temperatures for n-β-$FeSi_2$/p-Si and n-NC-$FeSi_2$/p-Si heterostructures.	🟦		
Anneal β-$FeSi_2$ and Fe_3Si films at varied temperatures by RTA, including characterization of their crystalline structure, chemical composition, morphological properties, wettability, and mechanical traits.		🟦	
Etch β-$FeSi_2$ films at various times in Ar atmosphere, including characterize their crystalline structure, chemical composition, morphological properties, wettability, and mechanical properties.			🟦
Perform plasma diagnosis for the plasma use during etching for plasma parameters.		🟦	🟦
Provide the essential data for publication and thesis.			🟦

1.5 Benefits of the study

1) Impedance and associated properties of n-β-$FeSi_2$/p-Si and n-NC-$FeSi_2$/p-Si junctions were revealed which help further realize their electrical characteristics, junction behaviors and mechanisms as well as realized their new possible application as storage devices.

2) Effects of RTA on wettability and mechanical properties of β-$FeSi_2$ and Fe_3Si films were demonstrated and revealed their potential to develop into hard coating surface.

3) Effects of Ar plasma on wetting and mechanical traits of β-$FeSi_2$ films were demonstrated and revealed their potential to develop into self-cleaning surface.

Chapter 2

Theory and Literature Reviews

Contents of his chapter review the essential background for discussing the physical properties of Fe-Si based materials as well as the basic concepts of impedance and wettability properties. It starts with a discussion of the semiconducting properties of NC-$FeSi_2$, β-$FeSi_2$, and Fe_3Si are then discussed. Next, the backgrounds of the deposition method, impedance, wettability, annealing and plasma etching are described. Previously published papers related to this study are discussed and compared with the current research.

2.1 The properties of Fe-Si system [41-45]

The Fe-Si system can be categorized into various phase. It can be seen as displays in a phase diagram below (Figure 2.1) that there are several phases including the intermediate phase (Fe_5Si_3), metal-rich silicide (Fe_3Si), monosilicide (FeSi), and disilicide ($FeSi_2$).

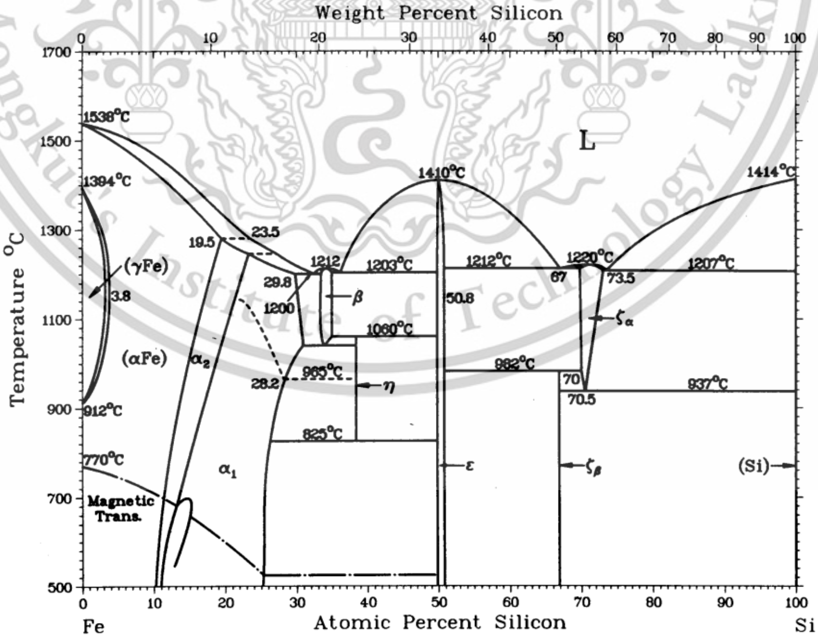

Figure 2.1 A phase diagram of the Fe-Si composite [45].

2.1.1 Physical Features of β-FeSi$_2$ [46-50]

In the area of the FeSi$_2$, three phases are separated as follows: cubic (γ-FeSi$_2$), orthorhombic (β-FeSi$_2$), as well as tetragonal (α-FeSi$_2$). The cubic γ-FeSi$_2$ phase of F-Si falls under a metastable phase that appears through polymorphic transformation of β-FeSi$_2$ at low-temperature of 650 °C. The metallic α-FeSi$_2$ phase stays stable when temperature is > 950 °C. It can be transformed into the orthorhombic β-FeSi$_2$ phase when the temperature is < 950 °C. Recently, β-FeSi$_2$, which is a semiconductor, has attracted significant attention owing to its potential as candidate for application in optoelectronic devices. Components of β-FeSi$_2$ is contained Fe and Si, which are both eco-friendly, non-toxic, and plentiful in nature. The compound holds an orthorhombic structure having 48 atoms per unit cell (Si 32 atoms and Fe 16 atoms) and lattice parameters value at c = 0.788 nm, b =0.778 nm, and a = 0.986 nm, as depicted in Figure 2.2. One unit cell possesses two Fe sites, both are inhabited by 8 atoms each and two Si sites each inhabited by 16 atoms.

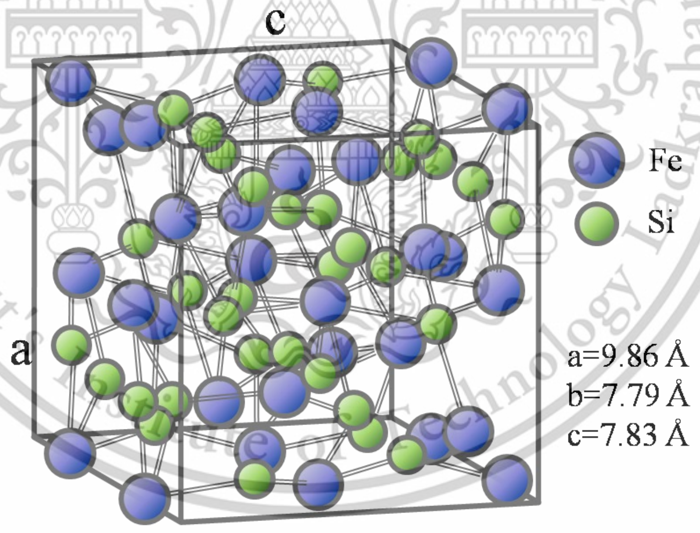

Figure 2.2 Primitive cell of orthorhombic β-FeSi$_2$ structure [46].

Band diagram of β-FeSi$_2$ is displayed in Figure 2.3(a). The nature of the gap inside the band structure is indirect with small difference between the calculated direct and indirect gaps based on absorption spectrum showed in Figure 2.3(b). From indirect gap, the part of absorption found under the direct-gap transition energy level could be explained. As revealed in the inset of Figure 2.3(b), β-FeSi$_2$ possesses an indirect band gap of around 0.76 eV, which is less than the value of direct optical band gap of round 0.85 eV and matches to the fiber optic telecommunication's wavelengths as well as specifically huge optical absorption coefficient that values bigger than 10^5 cm^{-1}. The absorption coefficient is more than two magnitudes higher than what possessed by crystalline Si at 1.2 eV.

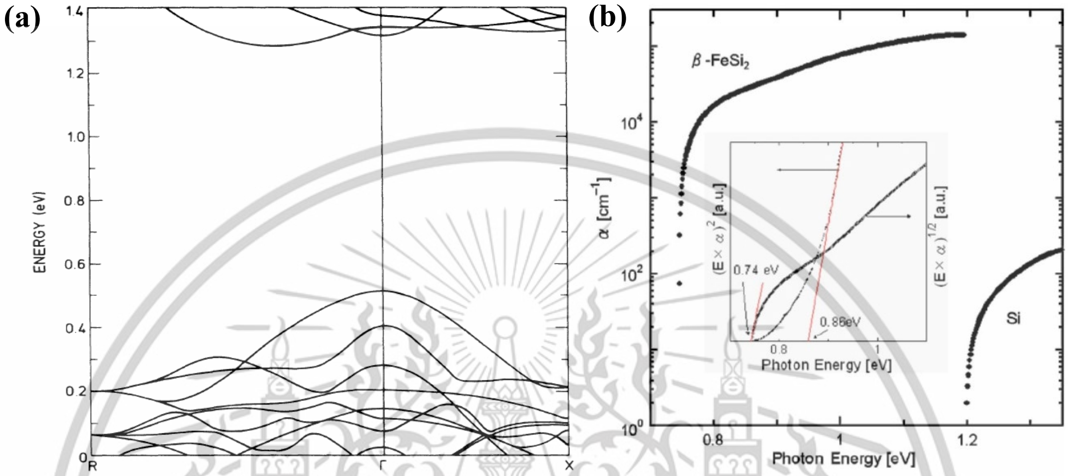

Figure 2.3 (a) Band diagram and (b) absorption spectrum for β-FeSi$_2$ with the interpolated line drawn for the indirect and the direct optical band gaps of the β-FeSi$_2$ as its inset [50].

2.1.2 Physical Features of NC-FeSi$_2$ [51-53]

The formation of amorphous FeSi$_2$ was first reported by M. Milosavlijevic et al. They created a Fe layer on a Si substrate at 300 °C by ion beam mixing (IEM) with Ar^{8+} ions, producing a uniform amorphous layer. Optical absorption measurements confirmed that the material was a semiconductor with a direct band gap of around 0.88 eV, and rapid surface diffusion of Si atoms was deemed to be the main cause of the creation of the amorphous phase. Nanocrystalline FeSi$_2$ (NC-FeSi$_2$) films were subsequently prepared by pulsed laser deposition (PLD) through an FeSi$_2$ target, and their properties were investigated. NC-FeSi$_2$ has properties similar to β-FeSi$_2$ and amorphous FeSi$_2$ and is of interest as a semiconductor and coating material for near-infrared (NIR) applications. The component elements Fe and Si are ample and non-toxic on Earth, making them promising materials with low environmental impact. NC-FeSi$_2$ has an optical band gap of about 0.87 eV as well as a high extinction coefficient of light beyond 10^5 cm^{-1} at 1.2 eV. Another major advantage is that its ability to be coated on various solid substrates at ambient temperature. The structure of NC-$FeSi_2$ films prepared by PLD and FTDCS was inspected by X-ray diffractometer (XRD) and transmission variant of electron microscope (TEM). In the XRD pattern revealed in Figure 2.4, a broad peak was detected from 40° to 50° in the 2θ scan mode with a static incident angle of 4°. Due to the nanocrystalline structure, the board peak is likely the result of overlapping diffraction from multiple crystal planes of β-$FeSi_2$ (e.g., 422, 511, 313, etc.). Interestingly, the FTDCS-prepared film shows a slightly stronger peak than the PLD film, suggesting a slightly larger crystallite size. This trend is also seen in the microelectron diffraction (MD) results of the PLD film, which shows a weak, broad ring corresponding to a lattice spacing of 2.03 Å. Furthermore, the dark-field TEM image in Figure 2.5 shows that the PLD film is composed of nanocrystals with diameters of 3-5 nm, which are likely β-$FeSi_2$ nanocrystals.

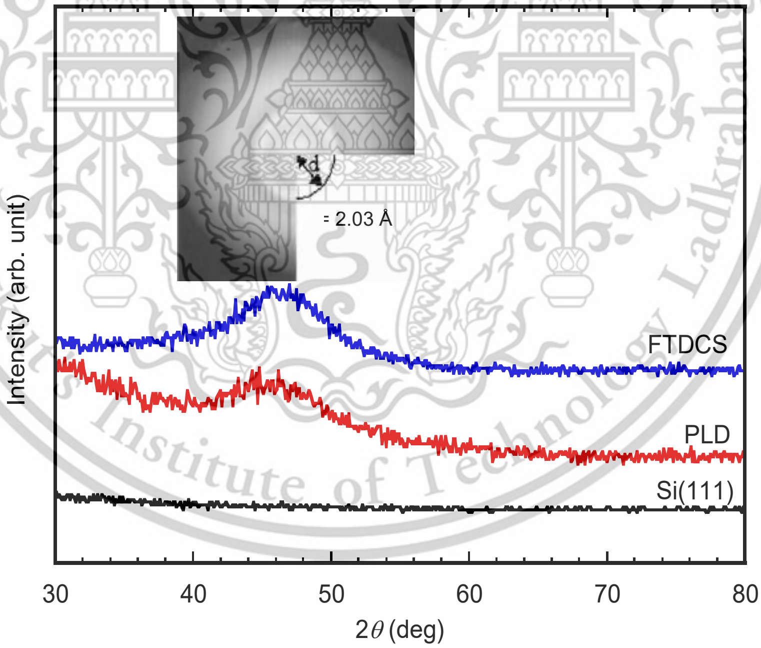

Figure 2.4 XRD graphs of NC-$FeSi_2$ films formed via PLD and FTDCS. The inset is the micro-area electron diffraction (MD) pattern of the NC-$FeSi_2$ film produced via PLD [51].

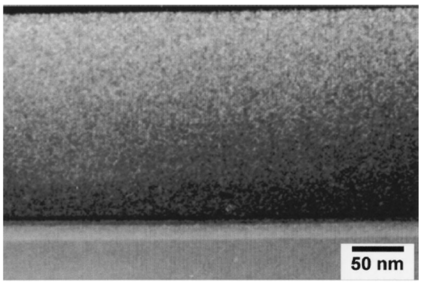

Figure 2.5 Dark-field imaging TEM result of the NC-FeSi$_2$ films formed via PLD [51].

2.1.3 Physical Features of Fe$_3$Si [56-60]

Fe$_3$Si is the sole phase among homogeneous iron silicide phases that has well-ordered iron-rich composition (sees Figure. 2.6). It belongs to the bulk phase diagram at ambient temperature and remains steady up to its melting point with crystal's structure is of D0$_3$ type which can be deemed as a Heusler type alloy: Fe$_2$FeSi. Due to Fe and Si randomly inhabit the C sites while retain its symmetric structure, silicon atoms in this phase have maximized their mutual distance and dominate an impressively large chunk of the phase diagram from the idyllic Si concentration of 25% and below. When Fe or Si randomly inhabit C and B sites, B$_2$ (CsCl) phase will take over DO$_3$ phase when Si concentration less than about 10%. At even lower Si composition, Fe or Si will randomly inhabit all atomic sites and the A$_2$ (bcc) phase emerge. At the phase beyond the idyllic composition of the D0$_3$, Fe$_3$Si undergo a sudden transition into an inhomogeneous phase, where its phase boundary ranges from 26% to 31% at room temperature to 1200 °C.

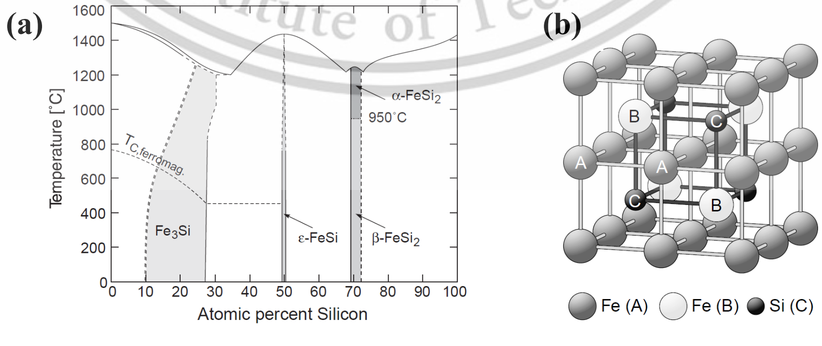

Figure. 2.6 (a) Phase diagram for iron silicide where well-ordered homogeneous phase's regions highlighted in the grey highlight. (b) Unit cell represents the D0$_3$ structured Fe$_3$Si consist of bcc and CsCl sub-cubic structure [56].

Alloys in Fe-Si system have captivated extensive attention for technological and fundamental purposes. Naturally, iron-rich composition displays ferromagnetism, which immediately made it promising candidate as magnetic devices in silicon-based semiconductor device. The ferromagnetic layer offering new potentials abilities to inject and manipulate electric spin inside a layer of semiconductor in semiconductor device. Ferromagnetic iron silicide or Fe_3Si has lattice constant a=5.653 Å, which is almost the same as that for GaAs. Its lattice constant also slightly mismatches with lattice of semiconducting Si by +4.2% and high Curie temperature level of 840 K. At the Fermi stage, the low polarization threshold and high spin polarization is predicted, and it is an attractive electrical spin injection material. Hypothetically, similar properties with DO_3 Fe_3Si can manifest within a Fe_3Si of different atomic arrangement like B_2 structure. The efficiency of electrical spin injection from the ferromagnet to the semiconductor is highly dependent on their interface quality. To prevent the interlayer diffusion between Fe_3Si/Si, this material needs low-temperature growth to limit the generation of high velocity Fe species. Yoshitake et al. reported on the method of epitaxially creating ferromagnetic Fe_3Si films via FTDCS at room temperature onto Si(111) substrate. This method allowed them to create Fe_3Si films at a low-pressure sputtering with a lower rate of deposition with more precision. In exchange, the films created this way possess B_2 structure instead of DO_3. This evidenced by from superlattice reflection appear as (222) orientation XRD pattern, where h, k, and l are all odd number (see Figure 2.7).

.

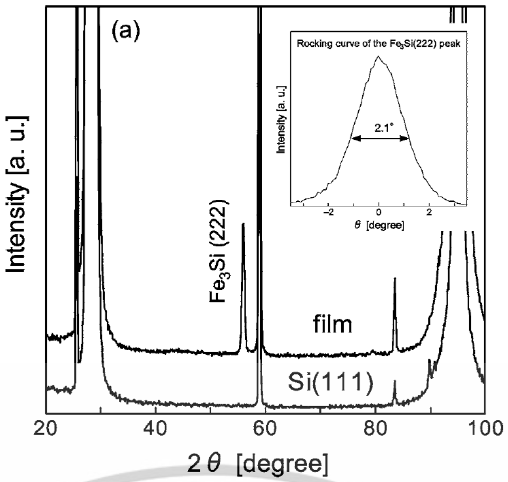

Figure 2.7 XRD pattern of Fe$_3$Si expitaxially deposited onto Si(111) via FTDCS by Yoshitake et al [6].

2.2 FTDCS [61-64]

Sputtering belongs to a physical vapor deposition (PVD) technique that is utilized for the growth of thin film layers as well as cleaning and etching of the surface of the thin film. This process is generated by the bombardment of accelerated ions on the surface of a sputtering target. After the accelerated ions reach the surface of the target with energy above the surface binding energy, a target atom can be expelled from a target and deposited on a substrate. FTDCS is a modified sputtering system having the advantages of low-substrate temperature and high deposition rate during sputtering. A graphic of the FTDCS schematic is revealed in Figure 2.8. The FTDCS system consists of two circular-shaped targets with the same dimension. Each target is situated opposing the other. Permanent magnets are arranged in a division behind the pair of targets to form a magnetic field spreading from one target to the other. Such a magnetic field confines plasma, generated by a discharge process, within the discharge area. A sputtering particle formed by the discharge process is deposited on a substrate attached in isolation from the discharge space.

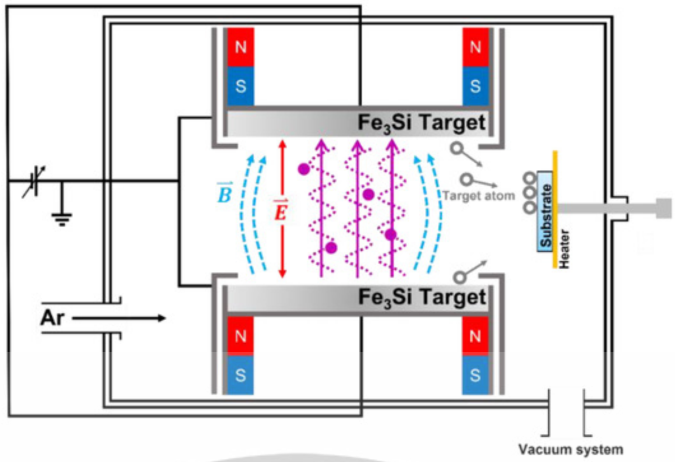

Figure 2.8 The schematic diagram of the FTDCS system [23].

FTDCS has the following advantages: (i) high plasma density generated from the sputtering process; (ii) sputtering at low pressure operation; (iii) low increment of substrate temperature; (iv) low damage from plasma; and (v) acquired films with low stoichiometric difference comparing to thier target owing to the substrate being safe from plasma. Besides, the energy of particles that deliver to the surface of the substrate is raised when compared to the use of other methods due to sputtering at low pressure.

2.3 Heterostructure diode [65-67]

Heterostructure diodes are typically dictated by the interface between two types semiconductors. Typically, these semiconductors would possess similar lattice constants to eliminate interface stress, but differ in energy bandgap and electronic relationships. This is different from using the same type of semiconductor on both sides of a homostructure. The difference in electronic structure leads to the generation of electric field at the connection point. When two types of semiconductors have the same type of conductivity condition (e.g., both types are n-type or both types are p-type), if there are opposite types of conductivity conditions, the connection point is called isotopic hybridization. The connection point between a p-type and an n-type is called isotopic ectopic element, which is different from the curvature of flat bands in isotopes. The energy band structure of an ectopic element diode shows discontinuity at the interface due to differences in electronic affinity, work functions, and characteristics of other materials. Such discontinuities can cause interface states or band offsets that act as recombination centers inside devices. Heterostructure diodes can be categorized into three types based on the arrangement of the valence and conduction bands as portrayed in Figure 2.9.

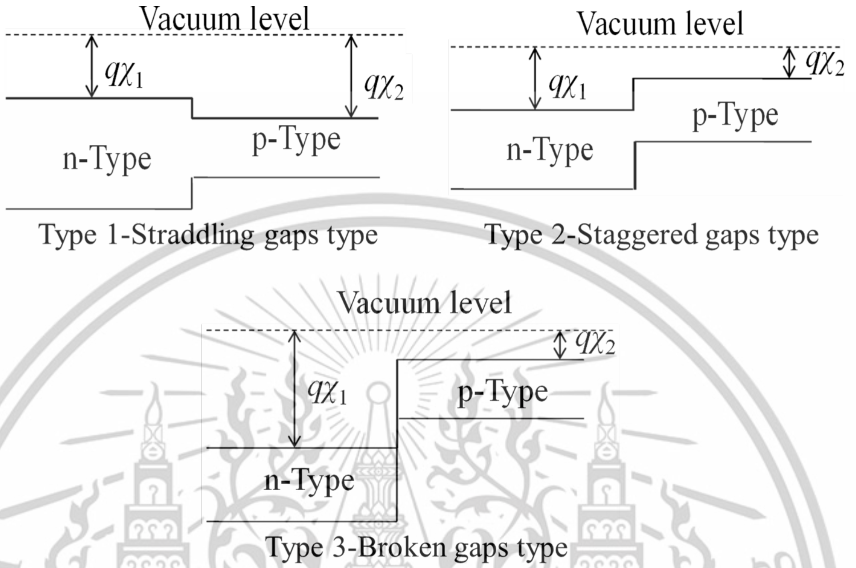

Figure 2.9 Several kinds of heterojunctions based on alignment of band gap [66].

Heterojunction's Charge transport models are developed from original models used in homojunctions. A spike in the band edges in Figure 2.10 arises from electron affinities ($\chi_{1,2}$), optical band gaps ($E_{g1,2}$), and work function ($\Phi_{1,2}$) mismatch between two different types of semiconducting materials. The inset figure in Figure 2.10 displays discontinuity of conduction band and valance band. The band offset of the conduction band is defined by equation based on Anderson's rule as seen below:

$$\Delta E_c = q\chi_2 - q\chi_1 \tag{2.1}$$

Meanwhile, the band offset appeared on the valance band is defined as follows

$$\Delta E_{\mathrm{V}} = \left(Eg_1 - Eg_2\right) - \Delta E_{\mathrm{C}} = \Delta E_{\mathrm{g}} - \Delta E_{\mathrm{C}} \tag{2.2}$$

Barrier in the heterojunction, which increases the rate of recombination of the carriers born from photogeneration and affect the carrier movement, is originated from band offsets of the heterojunction. To minimize the influence of band offset in a heterojunction, value of electron affinity and band gap need to be similar to minimize ΔE_c value.

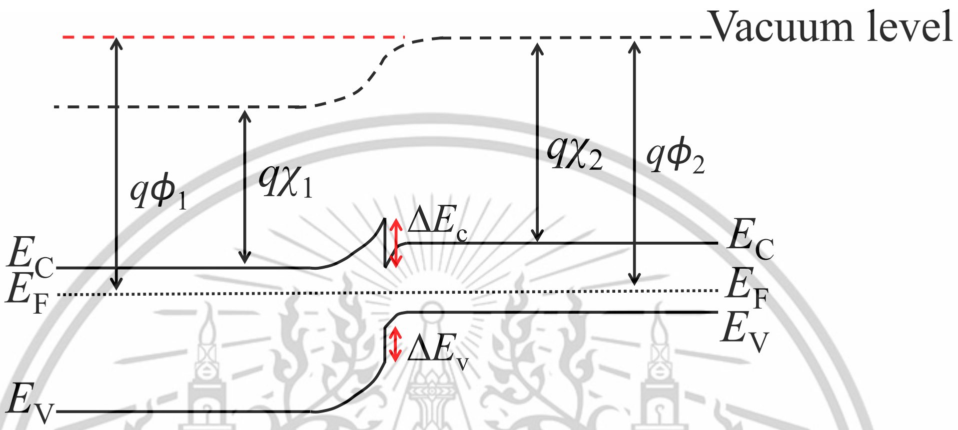

Figure 2.10 Diagram for band structure of Type 1 heterojunctions in thermal equilibrium state [66].

Photodiodes are optical sensors that generate either current or voltage when photons strike the pn junction of a semiconductor. While this term can broadly include solar cells, it typically refers to sensors that detect light intensity. In photoconductive mode, the photodiode is reverse biased, expanding the depletion layer and reducing junction capacitance, which improves response speed. Though only a small saturation current flows in reverse bias, the photocurrent increases proportionally with light intensity. This mode responds faster than the photovoltaic mode but produces more electronic noise.

Photodiodes are generally categorized into four types based on structure and function: pn junction, pin junction, Schottky, and avalanche. Each type is suited for detecting light intensity, position, color, or presence. Photons from incident light excite electrons in the semiconductor and induced the electron to move to the conduction from the valence band, relinquishing a hole If a photon's energy exceeds the bandgap energy (E_g). Electron-hole pairs can form in the p-layer, depletion region, and n-layer. Inside the space-charge zone, an internal electric field drives negative charges onto the n-layer and positive charges onto the p-layer. Electrons and holes are collected in their respective bands, generating an electron in the n-layer and a hole in the p-layer. When an external circuit connects these two layers of semiconductors, electrons inside n-layer and holes inside p-layer move to opposite electrodes. These charge carriers are responsible for the resulting electric current.

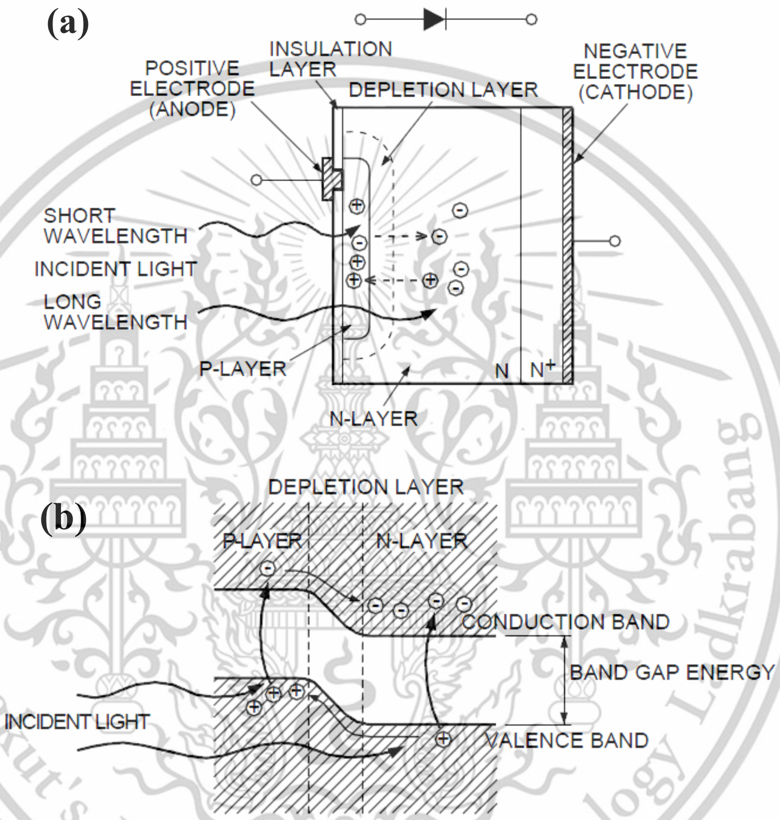

Figure 2.11 (a) Photodiode in cross section model and (b) diagram of p-n junction state in photodiode [67].

2.4 Impedance spectroscopy [12-14,68,69]

Impedance spectroscopy is a procedure for analyzing the electrical response of a system using small amplitude AC signals over a board frequency range. *Z'* and *Z"* in response to AC signals through the shape and number of arcs on the Nyquist diagram to get information about the internal electrical processes that occur internally.

This method is very effective to understand the electrical behavior of solar cells, optoelectronic devices, solid multilayer films, and heterojunction systems. For optoelectronic devices and heterojunction devices in particular, this technique help reveal detailed dynamics related to charge transfer, interfacial behavior, carrier relaxation, accumulation, recombination, and other factors affecting device performance.

This technique is based on Ohm's law, which is a basis for understanding basic electrical properties based on the relationship between voltage and current in an ideal resistor as following:

$$V = IR \tag{2.3}$$

Here *V* is the applied voltage existed throughout the resistor, *I* is electrical current that through, and *R* is resistance magnitude.

The impedance presents in the form of vector and complex depiction. Phase difference is source of complexity for the concept of electrical impedance comparing to the common concept of the resistance. The impedance spectroscopy is managed with aforementioned small amplitude AC signal under frequency in an extensive range. Commonly, the function of complex impedance links to the relation as following:

$$Z\left(j\omega\right) = Z\left(\omega\right) = Z' + Z'' \tag{2.4}$$

$$Z\left(\omega\right) = Z' - jZ'' \tag{2.5}$$

The impedance for a resistor is defined by formula below:

$$Z_R(\omega) = \frac{V\left(\omega,t\right)}{I\left(\omega,t\right)} = R \tag{2.6}$$

Thus, the impedance for a capacitor is defined by relation below:

$$Z_C(\omega) = \frac{V\left(\omega,t\right)}{I\left(\omega,t\right)} = \frac{1}{\omega C} \tag{2.7}$$

And the capacitor-based impedance defined in complex form is as follows:

$$Z_C(\omega) = \frac{1}{j\omega C} \tag{2.8}$$

Furthermore, the common component, the constant phase element (CPE), Warburg impedance, and Warburg short impedance are basis to the system model. CPE commonly used to represent non-ideal behavior of capacitor to deal with imperfect interfaces when model the equivalent circuit. The impedance based on CPE follows given equation:

$$Z_{\mathrm{CPE}}(\omega) = \frac{1}{(j\omega)^a \mathrm{CPE}} \tag{2.9}$$

The number and shape of semicircular arcs in a *Z"*-*Z'* (Nyquist) graph depend on the material properties, layer structure, and interface characteristics, which can be used to model an equivalent circuit to reflect the performance of a heterojunction. The elements in the model can be built on resistors, capacitors, and/or inductors, depending on how the devices react to an AC signal's disruption. In the basic case, a parallel circuit between R_p and C gives a symmetric semicircular arc starting from the origin. As shown in Figure 2.12(a), where R_p represents the resistance to charge movement across the junction interface, and the capacitance can be due to either the chemical capacitance or the capacitance of the depletion layer. If the curve is shifted to higher values on the *Z'* axis, the equivalent circuit must add a series resistance (R_s) together with $R_p||C$, as shown in Figure 2.12(b), where R_s comes from the ohmic contact resistance as well as the active layer resistance. In the case where the curve is asymmetric, with its center below the *Z'* axis and shifted towards higher values, it indicates non-ideal behavior. This can be modeled with a CPE connected in parallel with R_p and in series with R_s as shown in Figure 2.12(c), where CPE represents an imperfect capacitor caused by non-uniformities such as porous interfaces or surface states. The formulaic expression for complex impedance of the equivalent circuit model from Figure 2.12(c) is based on the equation below:

$$Z(\omega) = R_s + \frac{R_p}{1 + R_p (j\omega)^a \mathrm{CPE}} \tag{2.10}$$

where ω displays frequency in angular term. CPE is the value of constant phase element and a refers to a deviation of CPE from the ideal capacitor in ranging from 0 to 1. If $a = 1$, CPE can be substitute for an ideal capacitor.

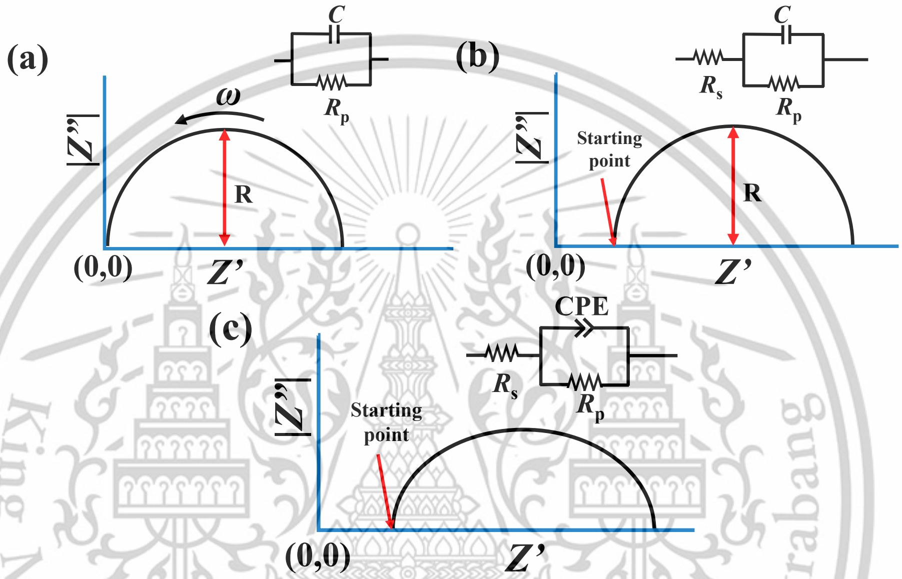

Figure 2.12 Nyquist diagram with related equivalent circuit models: (a) parallel circuit of R_p and C, (b) parallel circuit of R_p and C that serially combined with R_s, and (c) parallel circuit of R_p and CPE that serially connected with R_s [69].

The τ parameter defines as the characteristic relaxation time in relation to the characteristic frequency (f_{max}). τ can be used to characterize the relaxation process. Also, τ can applied to explain the charge carrier transport as well as the decay of its polarization throughout time in a discrete field. The assessment of τ can be achieved from the apex of the Z''-f spectrum per the utilization of the following equation:

$$\tau = 1/\omega_{\max} = 1/2\pi f_{\max} \tag{2.11}$$

Where τ is the carrier relaxation time, ω_{max} regards as the maximum angular frequency of relaxation, and f_{max} is the maximum relaxation frequency.

2.5 Dielectric Properties [70-73]

Dielectric properties relate to the polarization and dielectric relaxation inside specific material. Complex permittivity ($\varepsilon(\omega)$) can be separated to real term (ε') and imaginary term (ε''). The parts of complex impedance can be used to obtained both terms following equation between the $\varepsilon(\omega)$ and $Z(\omega)$ as portrayed in:

$$\varepsilon' = \left(\frac{-Z''}{Z''^2 + Z'^2}\right)\frac{1}{\omega C_0}\ ,\ \varepsilon'' = \left(\frac{Z'}{Z''^2 + Z'^2}\right)\frac{1}{\omega C_0} \tag{2.12}$$

where C_0 is capacitance in vacuum derived from the permittivity in vacuum (ε_0) of 8.8542×10^{-12} F m^{-1} proportion to the area of electrode (E) per film's thickness (t).

According to the Maxwell-Wagner model, in materials in which high conductivity grains are separated by high resistance grain boundaries, interfacial and space charge polarizations occur. This explains the frequency-dependent actions of the ε' term in the measurement range. The high values of ε' are due to the polarization phenomenon caused by the capture of charge carriers from the grain interior by the high resistance grain boundaries due to the external electric field. On the other hand, the ε'' parameter mainly reflects the dielectric loss due to electrical conduction, and its peak position can be used to estimate the conduction mechanism in the material. Meanwhile, the dielectric loss tangent (tan δ) values is the relative dielectric loss from electrical energy used to induce the charge movement and the loss from thermal dissipation of dipole relaxation. Hence, tan δ could be obtained by the equation showed below:

$$tan(\delta) = \frac{\varepsilon''}{\varepsilon'} \tag{2.13}$$

2.6 Conductivity [74,75]

AC conductivity (σ_{AC}) profiles are obtained from impedance data. These data help to distinguish between the conduction models (e.g. band theory, jump relaxation model, variable range hopping model) for inorganic and organic materials. The frequency dependent behavior of σ_{AC} offers valuable information on the charge transport mechanism in semiconductor materials and reveals the nature of the conduction process and relaxation mechanism. Furthermore, the σ_{AC} characteristics at high frequencies provide clues to understand the relaxation phenomenon and jump relaxation model.

The roughly estimated σ_{AC} for the heterojunction devices can be derived through the formula seen below:

$$\sigma_{AC} = \frac{t}{E}\left(\frac{Z'}{Z''^2 + Z'^2}\right) \tag{2.14}$$

where σ_{AC} is to the AC electrical conductivity, *t* is the film thickness, and *E* is the area of the electrode. *Z'* and *Z"* respectively are the real and imaginary terms of the complex impedance.

The σ_{DC} value can be acquired from the y-intercept in the low frequency domain of the σ_{AC} value vs. frequency plot. This value helps to comprehend the conduction mechanism and electrical transport behavior in the material.

The hopping frequency (f_H) at each voltage value can be determined using a universal relationship and the point where the frequency corresponding to σ_{AC} is equal to σ_{DC} can also be used as an indicator to estimate f_H:

$$\left(\frac{\sigma_{DC}}{A}\right)^{\frac{1}{S}} = f_H \tag{2.15}$$

where σ_{DC} is the DC conductivity based on interpolation of the characteristic σ_{AC} against voltage at a low frequency range. *A* is the dispersion parameter. *S* is interaction degree between the mobile ions and the lattices.

Jonscher's power law describes how σ_{AC} increases at high frequencies following the displayed equation:

$$\sigma_{AC} = \sigma_{DC} + A\omega^{S} \tag{2.16}$$

Here, σ_{AC} is AC electrical conductivity, ω implies the angular frequency, σ_{DC} indicates the conductivity that does not depend on frequency, and *A* denotes the dispersion parameter. The exponent of *S* means interaction degree between the transporting ions and the lattices. The dispersion parameters and the degree of interaction of the mobile ions with their lattice play a substantial role in this process. The exponent value indicates the type of charge carrier movement, with *S* values below 1 indicating translational motion and rapid hopping, and *S* values above 1 indicating localized hopping over short distances between adjacent positions.

2.7 Heat treatment [76,77]

Post-coating heat treatment is a process that utilizes various sources of thermal energy such as furnaces, flashlights, or lasers to alter the properties of thin films. However, there are differences in the coefficient of thermal expansion (CTE) of the film compared to the substrate, as well as phase transitions within the film. May cause stress within the film structure. This stress may result in permanent deformation or cracking at the joint between the film and substrate.

Despite these risks, heat treatment is still an important process for improving the quality of thin films. It promotes atomic diffusion, helps eliminate residual stress, and reduces structural defects that occur during the coating process. In addition, heat treatment stimulates particle growth. The phase transition and structural adjustment of materials directly affect the optimization of thin films.

2.7.1 CTA [76]

Annealing is commonly a means of softening in which samples are heated to create the steadiness high-temperature state and then allowed to moderate very slowly. For certain purposes, annealing is the standard method for developing mechanical, structural, stress reduction of materials, and surface morphology modification of samples with temperature and time.

2.7.2 RTA [77]

RTA relies on radiative heat transfer involving multiple bodies at varied temperatures, each emitting characteristic energy spectra. The process includes: (1) radiation emission of source, (2) absorption radiation, (3) conversion to heat, and (4) thermal conduction within the sample. RTA enables precise time-temperature control, ensuring reproducible results with minimal thermal stress and dopant diffusion—crucial for maintaining material hardness, which depends on internal stress without deformation. Its rapid heating cycles also enhance crystallization and grain growth, improving surface morphology and influencing wetting behavior. RTA typically uses tungsten-halogen lamp arrays (above, below, or on both sides of the wafer) to emit infrared radiation. Chambers are designed to reduce reflection using reflector array and often equipped with thermal shields. Temperature is monitored via thermocouples, one usually in direct contact with the wafer.

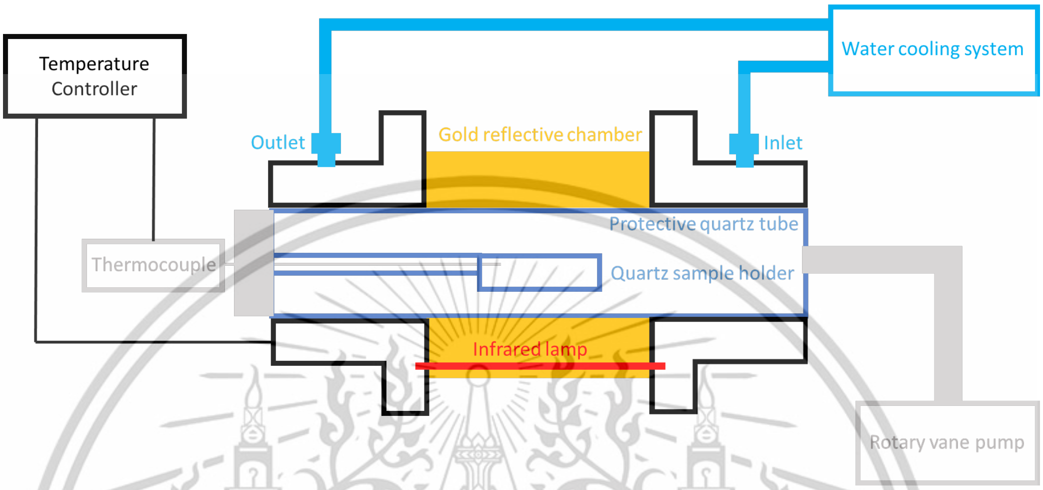

Figure 2.13 Schematic of RTA apparatus

2.8 Plasma etching [78,79]

A definition of plasma as state defines as an ionized gas comprises positive ions and free electrons in proportional amount resulting in no more or less number of overall electric charge either at low pressures or at very high temperatures in most case. There are two main classifications for plasmas based on the state of thermal equilibrium. First of the two is called hot plasma, whose ions and electrons nearly achieve thermal equilibrium creating fully ionized plasmas. Latter of the two is called cold plasmas which are weakly ionized plasmas due to non-equilibrium generation.

2.8.1 Conventional set up for plasma procedure

Plasma etching chamber have many iterations throughout the years, the more recent one is the microwave excited downstream etcher or microwave etcher, which is widely use due to its versatility. Microwave etcher is the more refined version of normal downstream etcher equipped with microwave source, which mostly operated at 2.45 GHz input. Due to its ability to operate at extremely low pressure (10^{-5} Torr at maximum). The microwave etcher could carry out the etching process that have relatively slow charge-particle recombination in comparison to diffusion and flow while having high plasma density. The microwave etcher offers also better control over the etching process by the subtraction of ions from the plasma area prompted by magnetic field. Contrary to the benefit of ability to easily adjust the condition of the etching process due to being less damaging, the low energy of the ions come with the downside of having lower etching rate. Some of microwave etcher may also equipped with auxiliary magnet coil for even better electron confinement. Schematic of Microwave etcher is presented in Figure 2.14. In this set up, the accelerated energetic charge species within the plasma are charged straight onto the substrate surface and cause the ion bombardment effect. Furthermore, this plasma apparatus can be utilized for material sputtering deposition as well as induce structural and chemical change if flux densities or energy of plasma ion exceed certain level needed for surface bombardment process.

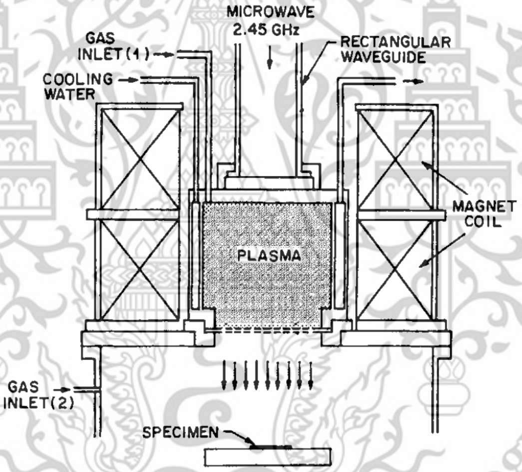

Figure 2.14 Schematic of Microwave etcher [78].

2.8.2 Mechanism behind the plasma etching

Plasma etching can proceed through various processes of physical sputtering or chemical reaction or ion-enhanced mechanisms. The common methods of plasma etching are schematically grouped into 3 categories as shown

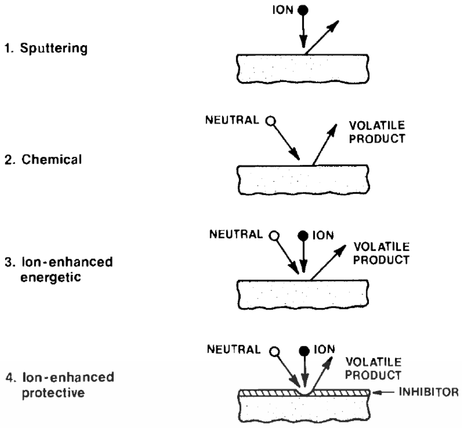

Figure 2.15 Variation of plasma interaction [78].

Plasma etching is a purely physical processes of material removal, where energetic ions transfer impact on the substrate and transfer their massive energy and momentum to it and ejected its material. Sputtering etching requires high plasma ion energies, existing in low pressure of lower than 50 mTorr. The long mean free paths of low-pressure plasma prevent the reflection and redeposition of the sputtered species when collisions in the gas phase happening. Also, the long mean free paths allow ejected sputtered material to reach opposing walls across the reactor. However, purely physical method like this requires high energy, resulting in low efficiency, such as low etching rate, surface faceting and trenching as well as electrical damage to the substrate and ion implantation from ion bombardment. In contrast, chemical etching method only relies elementary interaction of gas species a surface. The only requirement of chemical etching process is the formation of a volatile product through chemical reaction. Due to inherently sensitivity to the chemical consistency and variations of bonds, chemical etching is the most selective process of its kind. the occasionally downside of this process is regularly its isotropic or non-directional nature, which vertically and horizontally remove material at the same rate. The fine lines cannot be formed during this removal procedure. When a high energy ion flow contacts with the surface concurrently, energetic ion-enhanced etching causes less ion damage but gains improved reactivity. It creates a quick reaction that forms chemical species and removes material at a pace quicker than physical sputtering. This cause flaws and dislocations in the lattice or dangling bonds on the surface, resulting in occasion where surface compound can become partially separated. In general, the conventional etching process is based on the transfer of ion energy to the surface, which modifies the surface and makes the impact zone and its surroundings more reactive.

2.9 Wettability of surface [80]

Figure 2.16 presents a liquid drop located on a solid surface. Fundamentally, the contact angle (θ_{CA}) is determined by the juncture between the interface of liquid-solid (γ_{sl}) compared to the interface of liquid-vapor (γ_{lv}) (geometrically earned by employing a tangent line from the contact area that closes to the γ_{lv} in the droplet contour). In Figure 2.16, the three phases of the contact line are shown, representing solid, liquid, and vapor. A small θ_{CA} value is noticeable when the liquid flattens on the exterior layer of the substrate, while a high θ_{CA} value is noted when the liquid forms on the surface in round-shape.

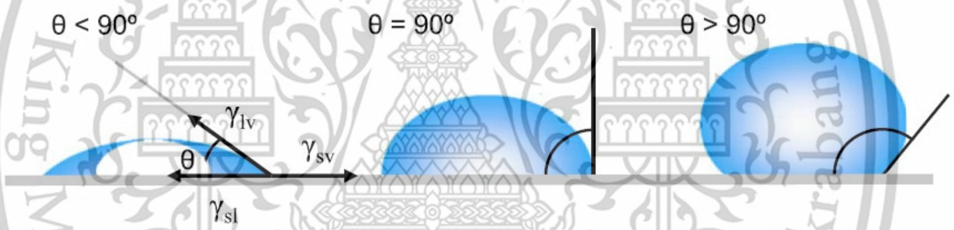

Figure 2.16 Illustration of contact angles on a fully flat surface of substrate [80].

The material's surface was indicated as a hydrophilic surface where the θ_{CA} values between the droplet and contact area of the surface were in a range from 5° to 90°. Namely, the drop will cover a large area on the surface. When the values of θ_{CA} range from 90 to 150°, it can be determined that the surface is hydrophobic. In other words, the contact area between the water droplets is minimal, resulting in maintaining the drop in a sphere. In the case of θ_{CA} evaluated in excess of 150°, the contact surface is shown to have nearly no contact between the drops, called a "Superhydrophobic surface". Conversely, the surface will show superhydrophilic properties where the contact angle values are lower than 5°. In this case, the drop is almost covering the entire contact regime of the substrate surface and showing a flat-shape for the drop on the substrate surface. The wetting behavior of the surface is uncovered in Figure 2.17.

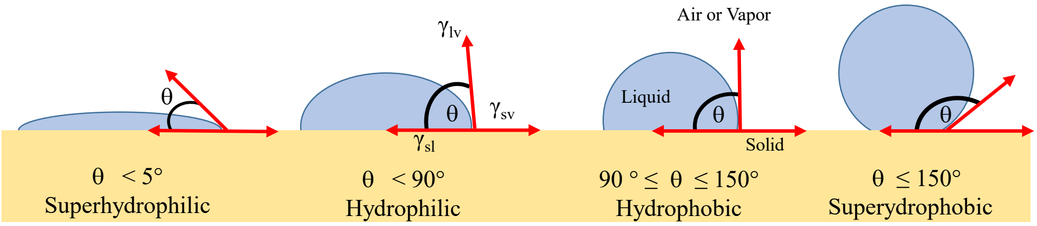

Figure 2.17 The illustration of the liquid shape on the smooth surface substrate in different range of contact angle [80].

2.9.1 Contact angle [31,32]

Atoms on a solid surface possess higher energy due to lack of bonds with its neighboring atoms in comparison to its interior. This surface energy or surface tension (γ) is the work mandatory to produce a unit area of individual surface under constant temperature and pressure. As displayed in Figure 2.18, the surface equilibrium will be established at a specific angle as a liquid drop contact with a solid. This angle is denoted to as the static contact angle (θ_0), which is given by Young's equation:

$$\cos\theta_0 = \frac{\gamma_{sv} - \gamma_{sl}}{\gamma_{lv}} \tag{2.17}$$

Where γ_{sv} refers to the surface energies of solid compared to air, while γ_{sl} represents the surface energies of solid compared to liquid, and γ_{lv} is the surface energies of liquid compared to air.

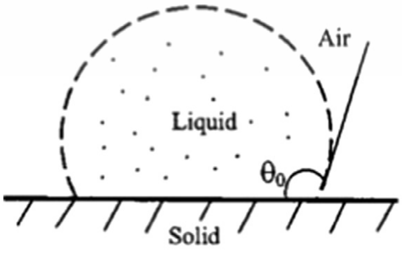

Figure 2.18 Illustration of contact line for liquid on a flat surface [32].

2.9.2 Wetting model of Wenzel and Cassie-Baxter [32,81-83]

In the case of a surface with roughness, two wetting models are usually seen: Wenzel's model and Cassie-Baxter's model. These two models are utilized for explanation of the θ_{CA} parameter of the drop versus the rough surface, where the drop and air can infiltrate into the groove on the surface area. The Wenzel and Cassie-Baxter interface are revealed in Figure 2.19 (a) and (b), correspondingly.

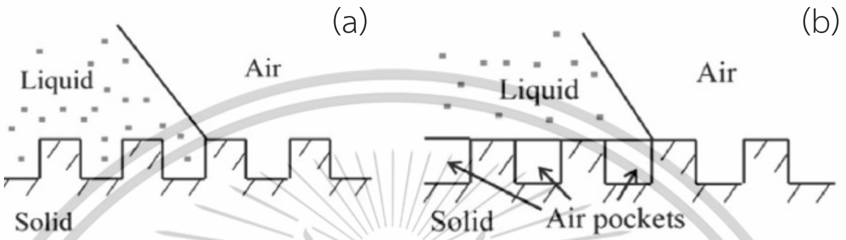

Figure 2.19 Illustration of (a) Wenzel interface and (b) Cassie-Baxter interface [32].

For the Wenzel model, the surface grooves are soaked by liquid drops, resulting in higher surface wettability due to the larger contact area. Wenzel's model describes the θ_{CA} on a rough surface in comparison to the flat solid surface. This model modifies Young's equation as seen below:

$$\cos\theta_0 = r\left(\frac{\gamma_{sv} - \gamma_{sl}}{\gamma_{lv}}\right) = r\cos\theta \tag{2.18}$$

Where *r* represents the surface roughness factor in non-dimensional term.

The *r* is the proportion of the actual area presented on the rough surface compared to the flat projection area, as symbolized by A_{sl} and A_F, respectively.

$$r = \frac{A_{sl}}{A_F} \tag{2.19}$$

The Cassie-Baxter model explains that an air pocket occurs underneath the liquid drops, resulting in a larger θ_{CA} value. This model assumes a composite surface is comprised of two kinds of patches. The resulting equation is for the apparent θ_{CA} on such a metrial's surface. Cassie-Baxter's model explains the θ_{CA}

value with two parameters of fractional area (f), and θ_{CA}. The contact angle of this model is given by:

$$\cos\theta = f_1 \cos\theta_1 + f_2 \cos\theta_2 \tag{2.20}$$

Where
$$f_1 + f_2 = 1 \tag{2.21}$$

For composite interface, the first fraction links to the solid–liquid interface, f_{sl} and $\theta_1 = \theta_0$. The second fraction corresponds with the liquid-air interface, $1 - f_{sl}$ and $\theta_2 = 180°$. Combining (2.20) with (2.21), the Cassie-Baxter model can be presented as:

$$\cos\theta = rf_{sl} \cos\theta_0 - 1 + f_{sl} \tag{2.22}$$

2.10 Characterization methods [84-89]

The basic principle of different characterization techniques used in this research to examine film's properties is presented this topic.

2.10.1 XRD

XRD is a technique commonly utilized for the characterization of crystalline structure. This technique detects the crystal of the coated layer in relation to a single wavelength of an X-ray source. The crystal structure can be categorized as either a monocrystalline or a polycrystalline. Myriad of structural characteristics, such as crystalline structure, crystalline diameter, and atomic spacing can be clarified using XRD. In general, cathode ray tube with a heated filament generates the X-ray This results in the Bragg's Law related scattering and absorption as presented below:

$$n\lambda = 2dsin(\theta) \tag{2.23}$$

where n is an order of diffraction, λ refers to a wavelength of the generated X-ray, d represents a length between the atomic layers, and θ is an incident angle.

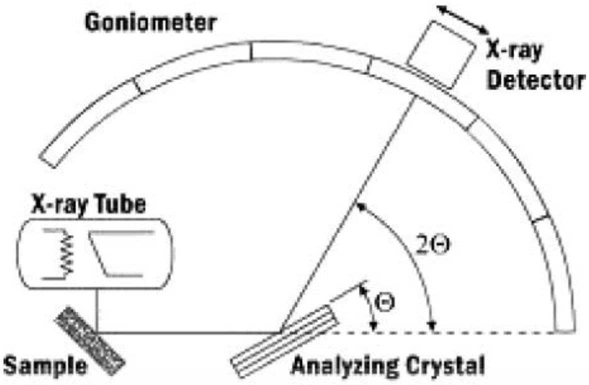

Figure 2.20 Diagram of XRD method.

2.10.2 X-ray photoelectron spectroscopy (XPS)

The XPS is one the most prevailing methods measuring the chemical composition (both qualitative and quantitative) and bond structure of tested surfaces. At the first step the X-Ray gun generates a directed flow of X-ray with defined energy to the sample surface. A flow of photoelectrons and Auger electrons departed from the sample surface as a result of interaction between an X-Ray beam and tested surface. For the most cases an analysis depth about 1-5 nm can be considered. A loss of kinetic energy due to collisions and scattering occurred for the depth more than 5 nm. Then the ejected photoelectrons focused to the entrance of hemispherical analyzer, where a kinetic energy of photoelectrons can be evaluated. Principal schema of XPS apparatus is shown in Figure 2.21. The XPS spectrum is representing a dependence of counts per unit of time (or intensity) from binding energy (can be recalculated directly from kinetic energy of photoelectrons). Analyzing the peak positions with help of XPS handbooks or XPS spectra databases, a conclusion about chemical elements can be done. Atomic concentrations can be further calculated, bond structure can be analyzed by peak fitting routines.

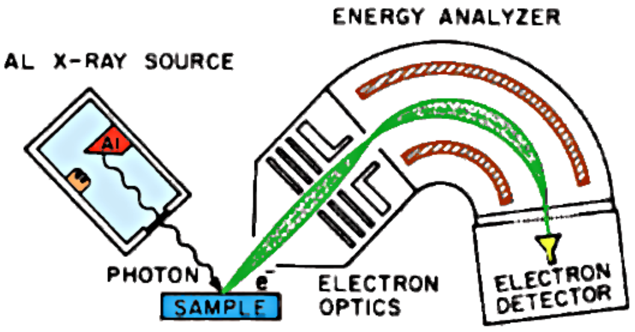

Figure 2.21 Principal schematic of the XPS device.

2.10.3 Scanning electron microscope (SEM)

Figure 2.22 illustrates a 2D-diagram for SEM. SEM is a microscope that shot an electron beam to strike the atoms of the object of interest to create the morphological image of the sample’s surface. The backscattered and secondary electrons produce from the source with a sufficient energy had a potential to hit the inner electron of the sample, causing the atom to be excited. Following the excitation of atom, the atom may release Auger electrons or X-ray photons to achieve relaxation process. The electron beam is guides toward the sample through electromagnetic lens. Then, the scanned signal that scatter from the incident electron beam was recorded from each scanning point. Finally, the scanning signal was detected by detector, where the signal will be translated into an image and displayed on the screen.

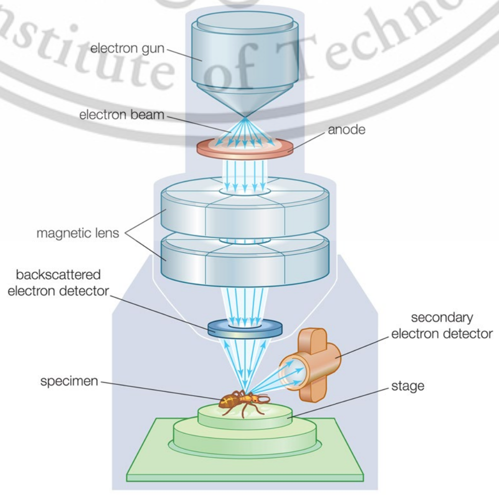

Figure 2.22 2D-schematic for SEM machine.

2.10.4 Atomic force microscopy (AFM)

An AFM is a nano-resolution microscope which uses a Van der Waals force for an observation of the topological properties of the sample surface. The measurement starts by moving a scanning probe over the scanning area. The AFM probe is typically made up of a Si tip and a cantilever set on a spring with a spring constant smaller than that of the atomic bond. Van der Waals force attracts and repels the scanning probe tip to the surface. The AFM probe is then pulled down the scanning path, while a laser focused on it is reflected by a reflector on the reverse of the cantilever. Then, the reflected beam is directed into a photodetector, which tracks the location of the beam to form an AFM picture. A piezoceramic scanner controlled by an electrical feedback loop voltage, maintaining the force between the probe's tip of AFM and the surface of the sample. AFM can be typically categorized into (i) contact mode, (ii) non-contact mode, and (iii) tapping mode.

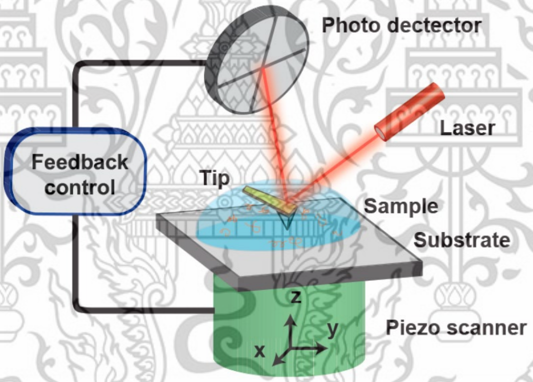

Figure 2.23 Basic diagram for AFM equipment.

2.10.5 Contact angle measurement

This technique measures θ_{CA} using a droplet of test liquid including the polar and non-polar liquids, such as deionized water, alcohol and oil, to determine a wetting properties of sample surface through a contact angle between the solution and the surface. It can be used for various task such as study of self-cleaning surface, non-stick pans, and waterproof fabrics etc. The contact angle measurement technique that is mostly used is the direct measurement of the static angle of wetting at point of contact known as sessile drop method. These measurements can be taken with various liquids and may be conducted on goniometers. A drop with a well-defined volume is positioned on the sample, and then several photographs are taken and the θ_{CA} between the tangent to the drop and the sample is measured for each frame.

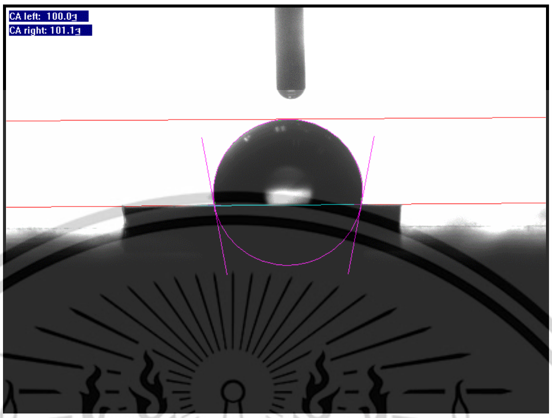

Figure 2.24 Photograph taken from sessile drop contact angle measurement.

2.10.6 Nanoindentation

Nanoindentation is performed to study the mechanical traits, such as hardness, stiffness, elasticity, wear resistance and adhesion force of the sample by applying a micro- or nanoscale force on to sample. Figure 2.25 expresses the schematic diagram for a nanoindenter. The nanoindentation is performed by the indenter attached to load-controlled instrument. The sample is placed on piezoelectric stage which can be precisely positioning throughout the x-y-z axis. The applied load from a coil and magnet assembly leads the indenter to penetrate the sample’s surface under measurement of displacement sensors. The most common indenter is diamond indenter with a three-sided pyramidal geometry called Berkovich tip.

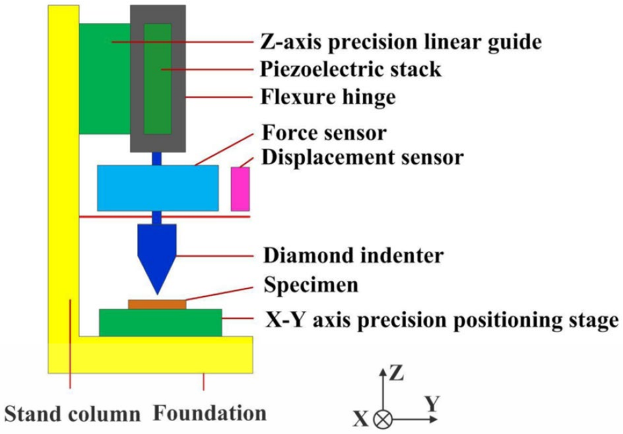

Figure 2.25 2D-schematic diagram for a nanoindentation machine.

2.11 Related research

This section presents the related research of this thesis.

In the previous works, heterojunctions consisted of n-type β-FeSi$_2$ or n-type NC- FeSi$_2$ on p-type Si have been created on p-type Si substrates using face-to-face targeted direct current sputtering (FTDCS) [9-11]. M. Shaban et al [9] reported photovoltaic Properties of β-FeSi$_2$/Si Heterojunctions under different substrate temperature which revealed that the epitaxial growth of the heterojunctions requires at least 600 °C substrate temperature to reduce the electrical leakage by suppress atomic diffusion of Fe atoms into the space charge region. N. Promros et al [10] reported transportation mechanisms of carriers were investigated by analyzing the dark J–V characteristics at temperatures ranging from 60 K to 300 K. The ideality factor was almost 2 at 140-300 K suggesting that the recombination process is the dominant. Meanwhile, the value is above 2 when temperature below 140 K, implying that a trap-assisted multi-step tunnelling process. R. Chaleawpong et al [11] estimate the interface state density of n-β-FeSi$_2$/p-Si heterojunctions. Based on the estimation, the values of interface state density were 4.68×10^{11} eV^{-1} cm^{-2} and 3.48×10^{12} eV^{-1} cm^{-2} at 1 MHz and 5 kHz. This interface state at the interface of the heterojunctions which behaves as a trap center for photo-generated carriers and the source of electrical leakage. Despite that, detailed studies on the electrical phenomena within semiconductor devices, such as charge transport, carrier accumulation and recombination, junction response, and relaxation behavior through Impedance spectroscopy are limited

In report by S. Sil et al. [70], the impedance analysis of hydrothermally synthesized Bornite showed that the Nyquist curves were characterized by a single hemispherical arc, indicating that the electrical response originated mainly from the bulk region, without significant influence from grain boundaries nor electrode interfaces. The total resistance decreased with increasing DC forward bias (0–0.8 V), indicating an increase in the carrier conductivity. The σ_{AC} analysis showed a frequency-independent part of conductivity within the low-range frequency (σ_0) and increased after passing a f_H. This behavior is consistent with Jonscher’s power law, where the exponent n (between 0 and 1) indicates the nature the charge transport involving charge carrier jumping between sites, facilitated by the electric field. Therefore, the investigation of impedance under varying voltages in fine-tuned range of ±1 V could expose precise mechanism behind conduction of heterojunctions.

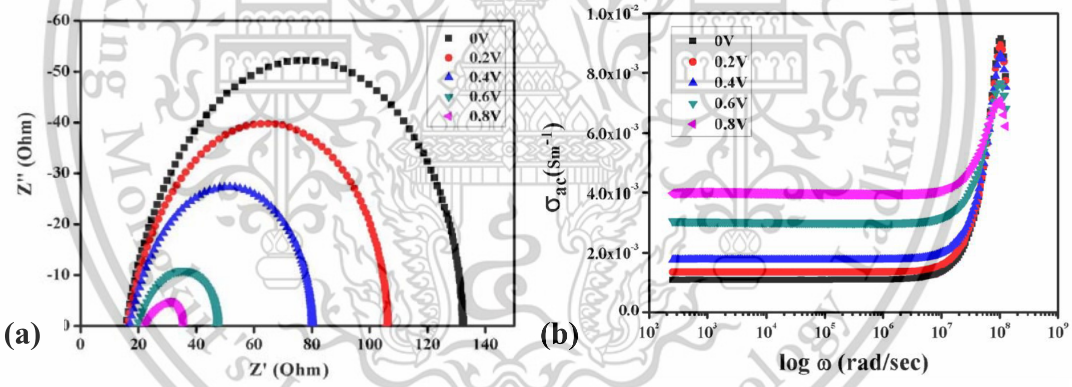

Figure 2.26 (a) Complex Nyquist plot of bornite composite and (b) σ_{AC} plot angular frequency for bornite material under different bias voltages [70].

Thakur et al. [21] reported the thermal transition of dielectric properties of $Bi_{0.8}Tb_{0.1}Pb_{0.1}Fe_{0.9}Ti_{0.1}O_3$ ceramics to decides the temperature range where the material can be utilized for application as an basis for electrical device. Based on dielectric results, variations of the ε' values of under increasing temperature at an frequency of 1 kHz, 10 kHz, and 0.1 MHz display seperate peaks at 200 and 350 °C. Contrarily, tan δ only display a abrupt rise at the last portion of the plot around of 350 to 400 °C. These results indicate that opertion range of $Bi_{0.8}Tb_{0.1}Pb_{0.1}Fe_{0.9}Ti_{0.1}O_3$

ceramics as dielectric material is 200 °C. This experiment regime show that study of impedance and by extension dielectric properties is crucial to determined possible practical range of application of material/devices. However, this work will be with in range formerly reported by N. Promros who reported transportation of in β-$FeSi_2$/Si Heterojunctions 60 K to 300 K but found tunnel effect when with temperature under 140 K and M. Shaban et al [90] who reported impedance of N-doped UNCD/Si under 300-400 K which is stable high temperature range for devices containing Si. Hence, 160-400K would be suitalbe range for the experiment.

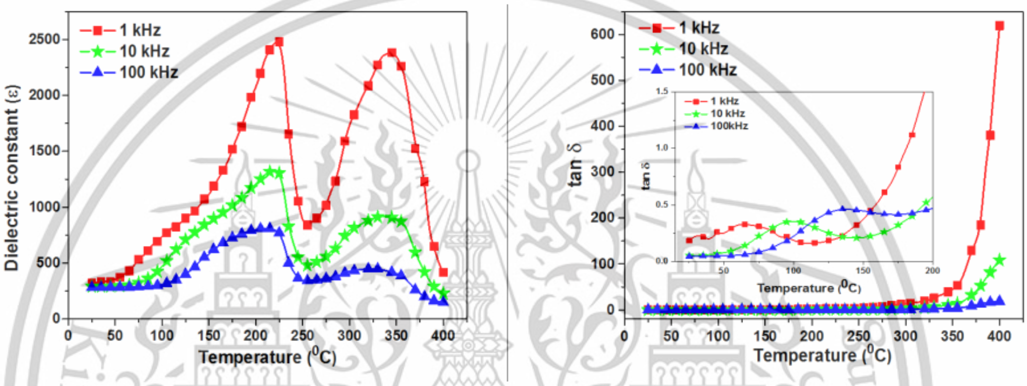

(a) (b)

Figure 2.27 (a) ε' and (b) tan δ of $Bi_{0.8}Tb_{0.1}Pb_{0.1}Fe_{0.9}Ti_{0.1}O_3$ ceramics at different frequencies of 1 kHz, 10 kHz and 100 kHz vs temperature [21].

In the past, there are sparsely report on mechanical properties of Fe-Si namely Fe_3Si and a few of $FeSi_2$ [25-27]. However, there was limited study on wettability of Fe-Si material [28,29]. Hence, wettability along with mechanical of Fe-Si created through FTDCS as well as effect of heat on the films to unlock new potential for multifunctional self-cleaning and hard coating applications on top of study on electrical properties for optoelectronic applications were reported [30,33]. The comparison of hardness from the past research and other research groups alongside commercial hard coating materials like DLC [91] can be found in figure 2.28. Meanwhile, the comparison of contact angle of the past works against value reported by other research group for Fe-Si based material can be found in figure 2.29.

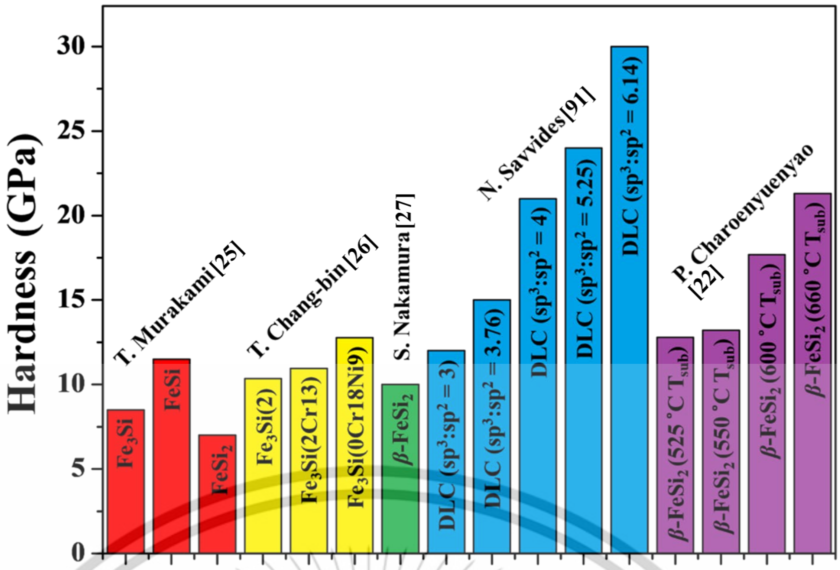

Figure 2.28 Comparison of hardness from the past researches and other research groups.

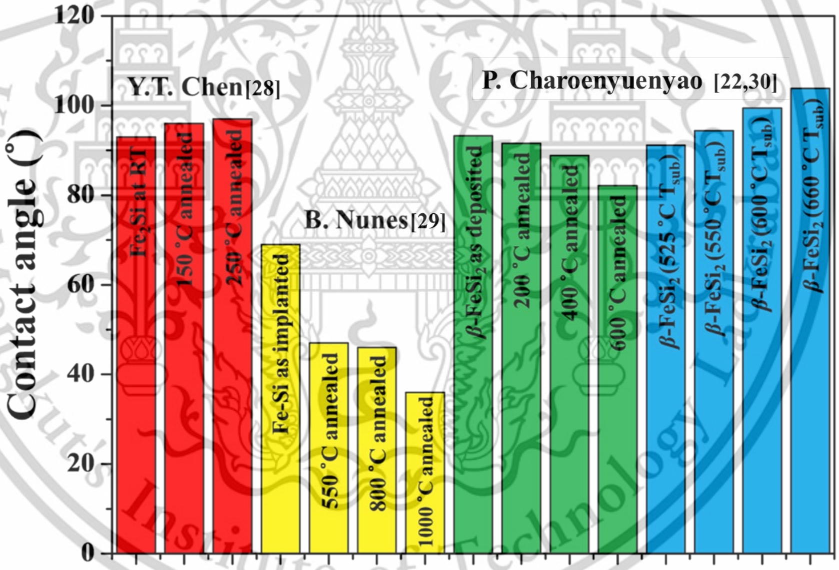

Figure 2.29 Comparison of contact angle from the past researches and other research groups.

To maximize the potential of new applications of Fe-Si, it is important to comprehensively evaluate its wettability and mechanical properties and identify the optimal surface modification method. RTA has many advantages over CTA, including enhanced grain growth, precise control of heating time and temperature, uniform isothermal treatment with less thermal gradient, reduced dopant diffusion risk, and cost advantages [34–36]. Focusing on these advantages, P.-H. Wu et al. [38] subjected SiN thin films to RTA at 400, 600, and 800 °C for 10 min and examined their mechanical properties. The results showed that with increasing RTA temperature, the hardness, Young's modulus, and residual stress control were significantly improved. This is attributed to the gradual release of the initial compressive stress, which turned into tensile stress at higher temperatures. In addition, Y.-J. Chiu et al. [39] performed RTA on FePd alloy thin films prepared by magnetron sputtering and reported that the contact angle increased from 20° before treatment to 52° and 75° after RTA treatment at 400 °C and 750 °C, respectively. These previous studies suggest that RTA is an effective surface modification method to improve the wettability and mechanical properties of Fe-Si thin films and can also be applied to the development of multifunctional hard coatings with self-cleaning capabilities. However, the annealing temperature should be limited to 800 °C to prevent the transformation to the undesirable α-$FeSi_2$ phase.

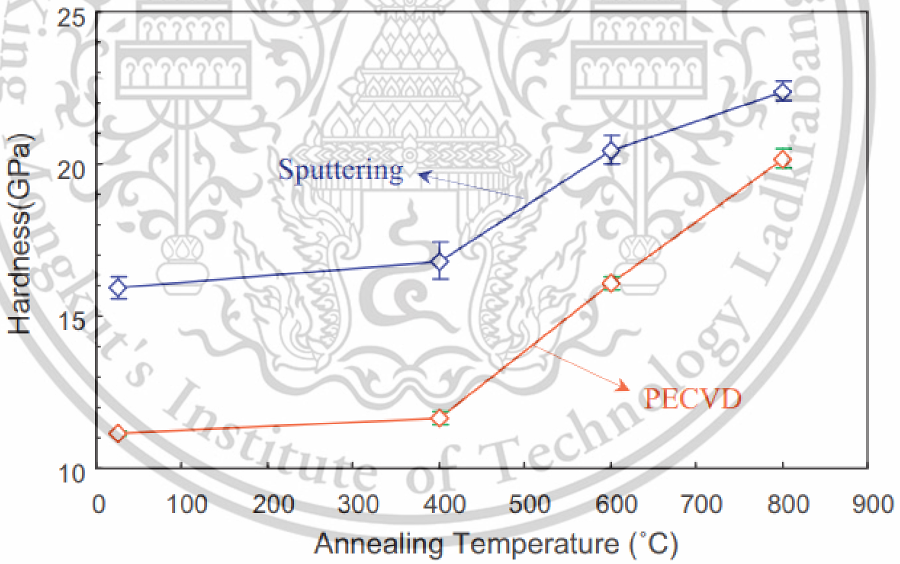

Figure 2.30 The values of hardness of SiN films versus RTA temperature [38].

Figure 2.31 Contact angle of FePd films versus RTA temperature [39].

Self-cleaning materials can be or really close to either a superhydrophobic surface (contact angle > 150°) or a superhydrophilic surface (contact angle < 10°) [31,32]. Hence, the surface modification should be more effective method for Fe-Si to reach its potential as the self-cleaning surface. Plasma etching has attracted particular attention because it can precisely control the interaction of ions with the material surface to tailor the material properties [23,24]. Ar plasma is widely used, since it has the ability to physically roughen the surface and can also remove oxide films by breaking the bonds between material and oxygen atoms [23,24]. Such surface modification significantly improves the surface reactivity and functional performance of materials, making plasma etching an essential process technology in advanced materials engineering [23,24]. In the previous works, N. Borwornpornmetee et al [23,24] reported the effect of microwave Ar plasma etching under variation of power on the physical traits of the Fe_3Si films and NC-$FeSi_2$ films to tailor their surface for self-cleaning application. The contact angle of the etching works in comparison to commercial self-cleaning material like polymethyl methacrylate [92] can be found in figure 2.32.

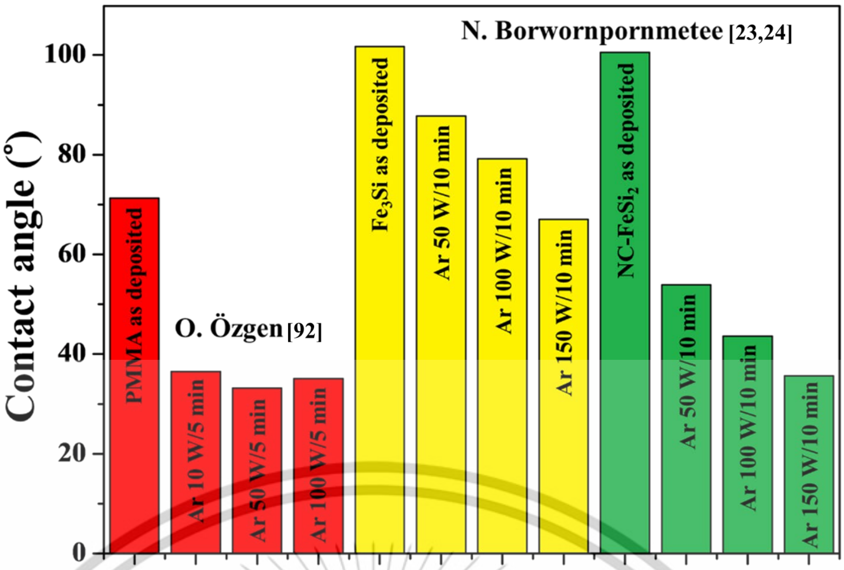

Figure 2.32 Comparison of contact angle from Fe-Si etching and PMMA.

However, the duration used to etch the sample with the plasma is also one of important factors for controlling the hydrophilicity of the material by controlling degree of interaction of ions [40]. According to the literature, Ting et al. [30] studied the etching of an aluminum surface with Ar gas plasma at different etching times. They found that the plasma at 1000 W etching for 30 s could reduce the high hydrophilic contact angle from approximately 20° to approximately 13°, and when etched for a longer time of 10 minutes, the contact angle of 13° reduced to approximately 4°, resulting in a superhydrophilic surface. Using the above-mentioned approach, it can be concluded that changing the duration of plasma etching can reduce the contact angle down to the superhydrophilic level. From the result, alteration of time should significantly increase hydrophilicity of the films.

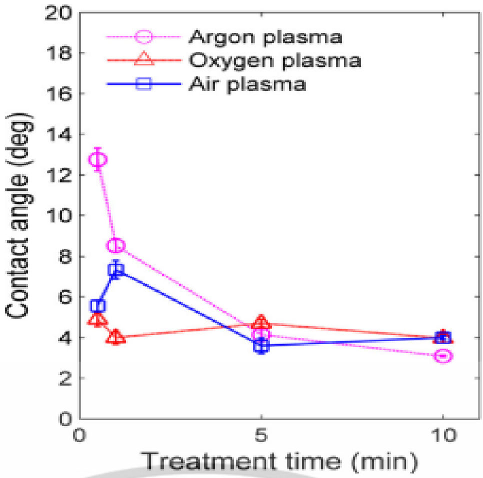

Figure 2.33 Contact angles of Al samples etched air, O_2 and Ar as working gases under varying plasma treatment duration [40].

Chapter 3

Research methodology

This chapter describes the details of film production, etching and characterization of film properties. It begins by describing the conditions for the creation of the NC-$FeSi_2$, β-$FeSi_2$, and Fe_3Si films by FTDCS. Next, the system and process for deposit electrode to complete heterojunction device, annealing of the films, and etching of the films are described. The last section of this chapter provides the details of several measurement methods for characterization of the electrical and physical properties of the films.

3.1 Creation of Fe-Si based films and heterojunction devices

In this research, NC-$FeSi_2$, β-$FeSi_2$, and Fe_3Si films were formed onto the surfaces of Si(111) substrates by Asst. Prof. Dr. Nathapron Promros and Japanese students at Kyushu University, Japan. The FTDCS system for the production of NC-$FeSi_2$, β-$FeSi_2$, and Fe_3Si films is demonstrated in Figure 3.1.

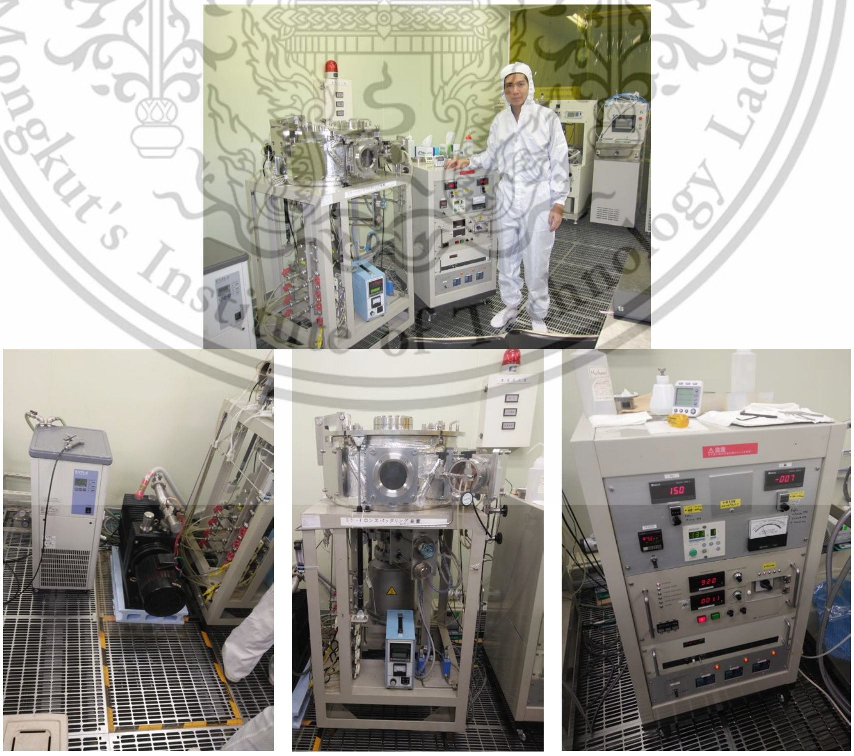

Figure 3.1 FTDCS system for the production of NC-$FeSi_2$, β-$FeSi_2$, and Fe_3Si films.

3.1.1 Production of NC-$FeSi_2$ thin films on the Si(111) wafer substrates

Using FTDCS, n-type NC-$FeSi_2$ films (film thickness of approximately 350 nm) were coated on Si(111) wafer substrates at ambient temperature. Prior to deposition, p-type silicon substrates were cleansed three times using acetone, methanol, and deionized water for 5 min each to remove surface oils and organic contaminants. The Si substrates were then submersed in a 1%-diluted hydrofluoric acid (HF) solution for the purging the layer of oxide from wafer, then quickly rinsed with deionized water. After finished the cleaning, the substrates were fixed on the holder of the FTDCS apparatus, and the chamber was evacuated to 10 μPa. Thin films were created under a mixed atmosphere of 15 sccm Ar gas and 10 sccm hydrogen gas. During sputtering, a DC voltage of 950 V and a discharge current of 1.2 mA were applied under a sputtering pressure of 133 mPa. Specifics of the sputtering conditions are shown in Table 3.1. Samples were separated into 2 batches one for heterojunction and another for surface modification.

Table 3.1 Coating conditions for the creation of NC-$FeSi_2$ films

Substrate	p-Si (111)
Target of sputtering	$FeSi_2$ (Purity: 6N)
Temperature of substrate	Room temperature
Base pressure	10 μPa
Sputtering pressure	133 mPa
Rate that Ar gas flow	15 sccm
Rate that H_2 gas flow	10 sccm
Applied voltage	950 V
Applied current	1.2 mA
Thickness of the films	350 nm

3.1.2 Fabrication process for β-$FeSi_2$ on Si(111) wafer substrates

To prepare n-type β-$FeSi_2$ films, cleaned p-type Si substrates, prepared by same procedure as previous section, were placed in a sputtering chamber. The chamber was evacuated to 30 μPa using a rotary vacuum pump in tandem with a turbomolecular pump. Then, Ar gas was then introduced at a gas flow rate of 15 sccm to stabilize the working pressure in the chamber at 133 mPa. The deposition of the thin film was performed by applying a discharge voltage of 1 kV and a direct current of 1.5 mA while maintaining the substrate temperature at 600 °C. The deposition conditions of $FeSi_2$ films by the FTDCS method, as well as the details of the post-deposition rapid thermal processing (under different temperature conditions) and etching process, are shown in Table 3.2. Samples were separated into 2 batches one for heterojunction and another for surface modification.

Table 3.2 Production condition for β-$FeSi_2$ films formed via FTDCS

Substrate	Si(111) wafer
Sputtering target	$FeSi_2$ (Purity: 6N)
Substrate temperature	600 °C
Ultimate pressure	30 μPa
Rate of Ar gas feeding	15 sccm
Working pressure	133 mPa
Applied voltage	1 kV
Applied Current	1.5 mA

3.1.3 Production of Fe_3Si films onto the Si(111) wafer substrates

Fe_3Si thin films with an estimated thickness of about 1000 nm were coated on p-type Si(111) wafer substrates by FTDCS. A pair of Fe_3Si alloy targets was used. The substrate temperature was kept at ambient temperature during production. Before sputtering, the Si(111) substrate was cleaned in three steps with acetone, methanol, and deionized water for about 5 minutes in each step, then the native oxide was then removed by a 1% HF solvent and immediately washed with demineralized water to prevent HF residue. The cleaned Si wafer substrate was placed onto a holder in the FTDCS chamber, with a distance of 7.5 cm from the target. Sputtering was performed using 6N Ar gas under a working pressure of 133 mPa and a gas flow rate of 15 sccm. The applied voltage was 1 kV and the applied current was about 1.2 mA. The details of the sputtering conditions used to form the Fe_3Si thin film are revealed in Table 3.3.

Table 3.3 Production conditions for the creation of Fe_3Si films

Substrate	Si (111)
Target of sputtering	Fe_3Si (Purity: 4N)
Temperature of substrate	Room temperature
Base pressure	30 μPa
Sputtering pressure	133 mPa
Rate of Ar gas flow	15 sccm
Applied voltage	1 kV
Applied current	1.2 mA
Thickness	1 μm

3.1.4 Fabrication of metallic contacts

The quality of the Al and Pd ohmic contacts was evaluated by their respective *I-V* characteristics. As shown in Figure 3.2, both the Al/β-$FeSi_2$ (or Al/NC-$FeSi_2$) and Pd/p-Si contacts showed linear *I-V* curves in the low current region, confirming the formation of good ohmic contacts. Formation of stable contacts on both sides of the $FeSi_2$/Si heterojunction ensures efficient flow of electrical current. The important factor for the formation of ohmic contacts are work function of the metal electrode (Φ_m), the electron affinity of the semiconducting material (χ), and the barrier height (Φ_b). For p-type semiconductors, Φ_m value should be higher than that of χ. For n-type semiconductors, Φ_m value should be as close as possible or lower than χ. Meanwhile, it is important to make Φ_b as small as possible to reduce the contact resistance. Hence, Pd with a Φ_m value of 5.12 eV was used on the p-type Si (χ = 4.05 eV) side and Al with a Φ_m value of 4.10 eV was used on the n-type $FeSi_2$ (χ = 4.16 eV) side to achieve a proper ohmic contact. Before the contact deposition, the native oxide was removed with 1% diluted HF, rinsed with deionized water, then dried with N_2 gas. Pd and Al electrodes (both with 4N purity) were deposited at ambient temperature by means of RF magnetron sputtering (Cesar-133). The active area of the completed device is about 1.0 mm² and no post-deposition annealing was performed. The deposition conditions are shown in Table 2 and the device structure is shown below:

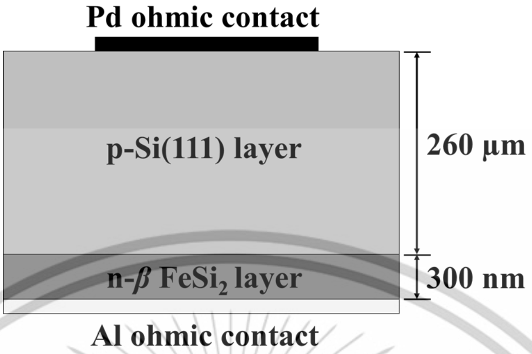

Figure 3.2 Schematic for Fe-Si/Si based heterostructures constructed by FTDCS.

Table 3.4. Fabrication conditions utilized in the fabrication of Al and Pd electrodes

	Al electrode	Pd electrode
Metallic target	Al (purity: 4N)	Pd (purity:4N)
Substrate heating	none	none
Ultimate pressure	10 µPa	10 µPa
Working pressure	266 mPa	133 mPa
Rate of Ar gas flow	10 sccm	10 sccm
Applied power	200 W	200 W
Rate of puttering	252 nm/hour	498 nm/hour
Thickness	500 nm	500 nm

3.2 Modification methods

3.2.1 RTA procedure

β-FeSi$_2$ and Fe$_3$Si Thin film Advance Riko Made MILA-5000 Rapid thermal annealing (RTA) was performed using the system. RTA temperature (T_{rta}) is 200 ˚C, 400 ˚C, 600 ˚C, 800 ˚C. The annealing duration of each RTA session was 10 minutes. The infrared gold image furnace variant of RTA (manipulated by the maker's programable temperature controller) quickly heated the sample within a minute from room temperature to the target temperature. RTA pressure in the chamber during process was control by Edwards Company RV series rotary vane pump to maintain at 0.6 Pa. EYELA Company’s CA-1116A cooling water circulation equipment ensured temperature stability of the whole system. After annealing, the system stopped automatically and the sample was cooled for 10 minutes.

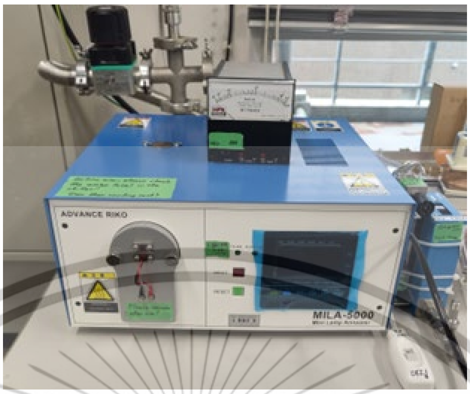

Figure 3.3 Rapid Thermal Annealing machine (ADVANCE RIKO,Inc, MILA-5000)

Table 3.5 RTA conditions of the β-$FeSi_2$ and Fe_3Si films formed by FTDCS

Samples	Pressure (Pa)	T_{RTA} (°C)	time (minutes)	Samples	Pressure (Pa)	T_{rta} (°C)	time (minutes)
β-$FeSi_2$	-	-	-	Fe_3Si	-	-	-
β-$FeSi_2$	0.6	200	10	Fe_3Si	0.6	200	10
β-$FeSi_2$	0.6	400	10	Fe_3Si	0.6	400	10
β-$FeSi_2$	0.6	600	10	Fe_3Si	0.6	600	10
β-$FeSi_2$	0.6	800	10	Fe_3Si	0.6	800	10

3.2.2 Plasma etching apparatus

In the current research, the etching process of β-$FeSi_2$ films produced via FTDCS method was carried out using Microwave (MW) plasma apparatus installed at Beamline 6a, Synchrotron Light Research Institute (SLRI), Thailand. The plasma etching apparatus is shown in Figure 3.4(a). This apparatus consists of three main parts: a plasma cleaning machine (Diener electronic, model: Pico) connected with a microwave source (Diener electronic, model: MWG 1200) and a gas relaying system. For the study, the film surfaces of the produced β-$FeSi_2$ films were modified at varied duration in Ar atmosphere by utilizing this etching apparatus. Before loading samples into the stage inside the plasma chamber, the β-$FeSi_2$ films were divide for each condition and cleaning up with methanol rinsing at the preparation room. Next, the prepared samples were moved into cleaned room where the etching apparatus stationed, as shown in Figure 3.4(b). Inside the vacuumed etching chamber, the plasma was built up through the microwave from the magnetron head. The fed Ar gas was ionize by the microwave and generated Ar plasma within vacuum chamber. The etching conditions for all films are depicted in Table 3.6. The etching times for the β-$FeSi_2$ were set to 10, 20, and 30 minutes operating under fixed 300 W.

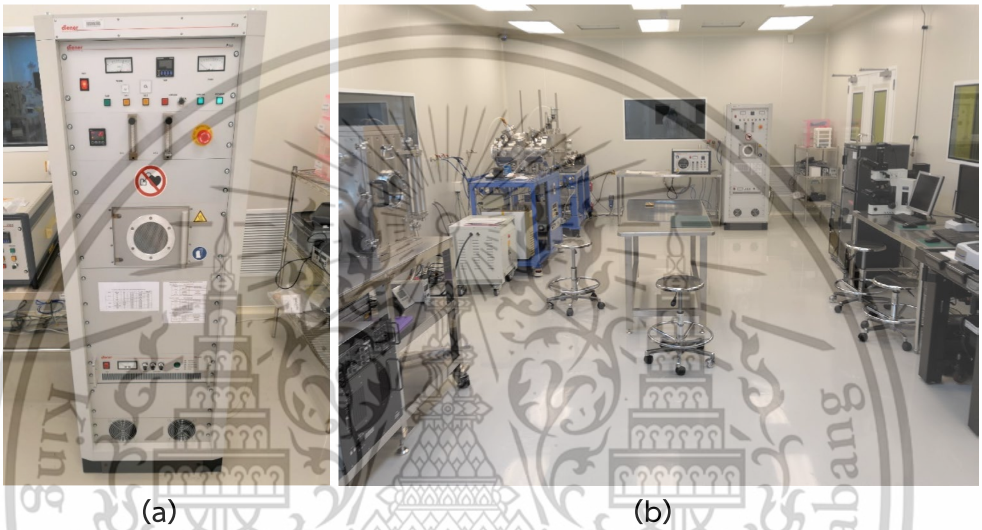
(a) (b)

Figure 3.4 (a) Plasma etching apparatus and (b) cleaned room at Beamline 6a, Synchrotron Light Research Institute, Thailand.

Table 3.6 Etching conditions for the NC-$FeSi_2$ and Fe_3Si films

Materials	Etching pressure (Pa)	Ar flow rate (sccm)	Etching power (°C)	Etching time (mins)
β-$FeSi_2$	-	-	-	-
β-$FeSi_2$	50	50	300	10
β-$FeSi_2$	50	50	300	20
β-$FeSi_2$	50	50	300	30

3.3 Electrical measurement

Figure 3.5 shows the experimental setup used for measuring *I-V* and *Z”-Z’* characteristics. All electrical measuring instruments were carried out at Kyushu

University in Japan. The system comprises a measurement station, temperature controller, liquid nitrogen container, rotary vacuum pump, personal computer, highly-stable power source, source meter, LCR meter, and a sealed chamber. The chamber's lid was kept closed during measurements to block ambient light and minimize other external interference. As shown in Figure 3.6, both the work station and the liquid nitrogen container were housed inside the chamber. Figure 3.7 displays the heterojunction device placement on the copper electrode inside the work station and the probes were carefully aligned to make contact with both the heterojunction device's electrode and the copper plate.

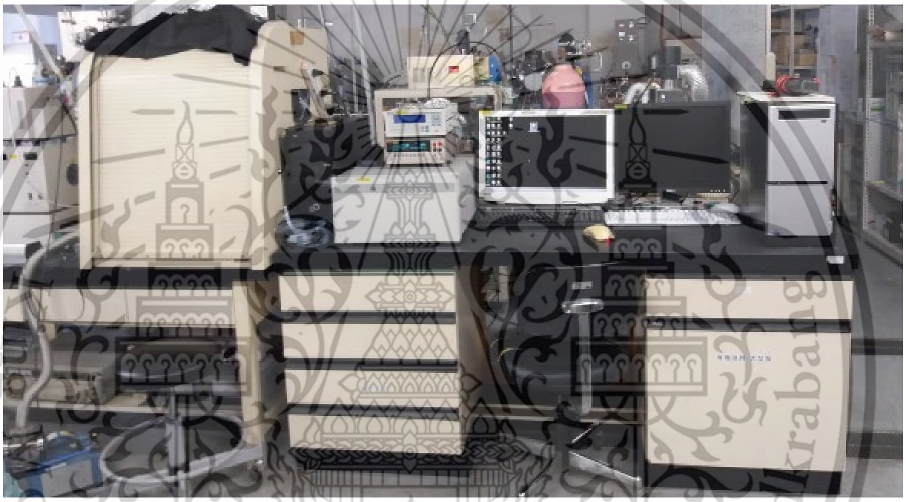

Figure 3.5 Electrical measurement system for examining the *I-V* and *Z”-Z’* characteristics.

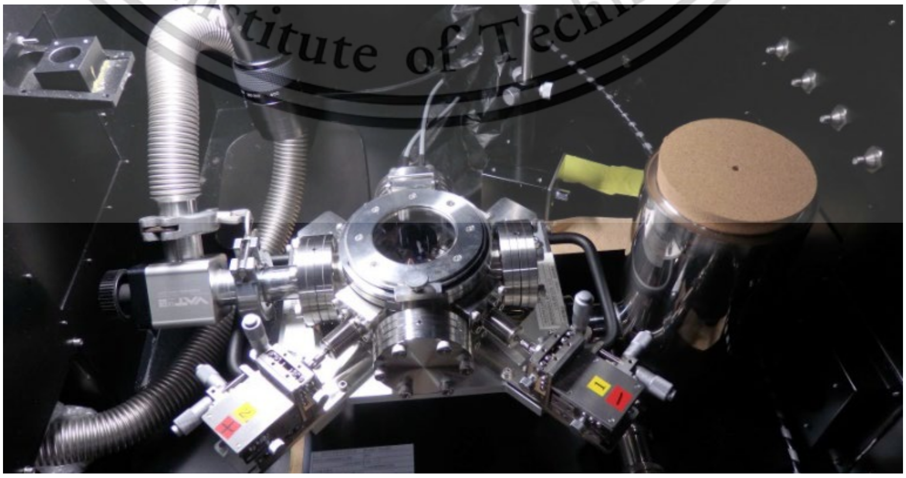

Figure 3.6 Inside of the chamber for electrical measurement.

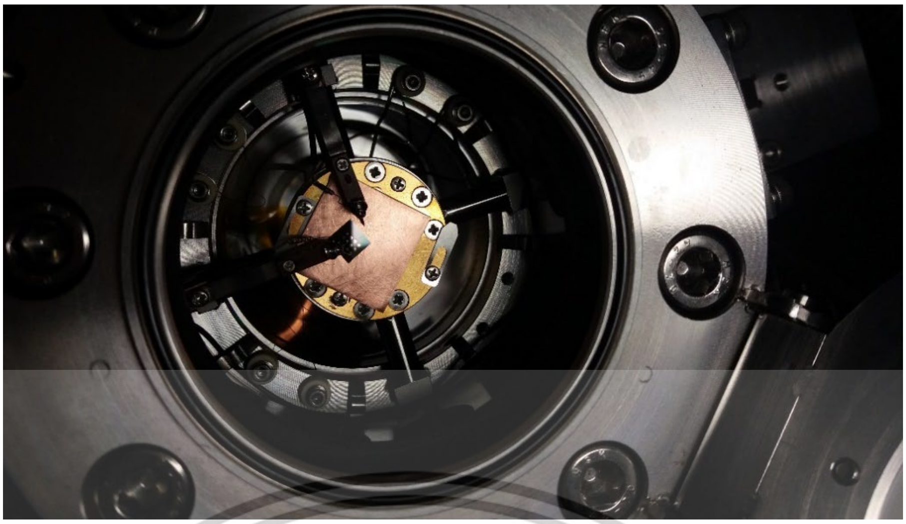

Figure 3.7 Placement of the sample inside the work station.

Impedance spectroscopy inspections were executed using a high-precision LCR meter (Agilent, model: E4980A). Before the measurements, *I-V* measurements were performed to confirm the rectifying properties of the fabricated heterojunction devices as mention in prior section. All impedance measurements were achieved in the dark environment under a frequency spanning from 20 Hz to 2 MHz. The data of n-type $FeSi_2$/p-type Si devices were acquired in the voltage range of -1 V to 0 V. Both experiments were carried on at ambient temperature. Based on the obtained impedance spectra, equivalent circuit were constructed to translate the electrical response of each device in to model representation. Circuit parameters such as R_s, R_p, and CPE were extracted using EC-Lab software. In addition, the dielectric and conductive properties such as τ, ε', ε'', and σ_{AC} were resulting from derivative of the Z' and Z'' data. The tan δ was calculated as the ratio of $\varepsilon''/\varepsilon'$ and was used as an index of relaxation loss. The σ_{DC} was obtained by linear extrapolation of the low frequency region of the σ_{AC}-f spectrum. In addition, the σ_{DC} and S value were also evaluated by applying the Jonscher power law to the σ_{AC} data. Then, temperature dependent impedance characteristics were inspected in the extent of 160–400 K, with the temperature controlled using a Model 335 temperature controller. The baised voltages was fixed to 0.01 V to induced the minimal response without causing conduction through electrical mean.

Figure 3.8 Precision LCR Meter : Agilent E4980A.

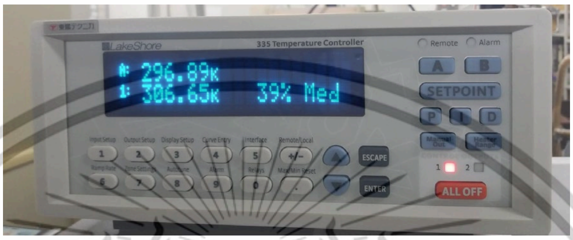

Figure 3.9 Temperature controller.

3.4 Characterization of the properties of Fe-Si films

Physical properties such as crystallinity, surface morphology, and wettability for the as-deposited and modified films were characterized using the following measurements:

3.4.1 Structure of films

The epitaxial production and crystallinity of the films were examined by utilization of XRD measurement using 2θ for the NC-FeSi$_2$ and 2θ-θ for Fe$_3$Si and β-FeSi$_2$ films were measured through this apparatus. The XRD results of as-produced and modified Fe-Si films were characterized by Rigaku TTRAX III XRD diffractometer at the National Metal and Materials Technology Center (MTEC) as shown in Figure 3.10.

Figure. 3.10 The XRD diffractometer (Rigaku, TTRAX III) at MTEC.

3.4.2 Surface composition of films

The atomic concentration of the as-deposited and modified films were monitored by means of XPS (Kratos Analytical, Axis Ultra DLD) at Analytical and Testing Service Center (ATC), The Petroleum and Petrochemical College, Chulalongkorn University, as displayed in Figure 3.11. The atomic concentration and XPS spectra was analyzed through CasaXPS software.

Figure 3.11 XPS equipment (Kratos Analytical, AXIS Ultra DLD).

3.4.3 Surface morphology of the films

The plane surface views of the as-created and modified Fe-Si films produced via FTDCS were displayed by utilizing a FESEM (Hitachi, SU 8230) with magnitude in a range from 30k to 300k. Figure 3.12 displays the FESEM apparatus used for examination of the surface morphology of the as-created and modified films.

Figure 3.12 The Hitachi SU 8230 FESEM apparatus.

3.4.4 Surface roughness of the films

The roughness mesurement of the surface for as-produced and modified films was carried out by means of AFM. Figure 3.13 illustrates the AFM apparatus (Park system, XE-120) for observing surface roughness under 5 X 5 μm^2. The surfaces of as-coated and modified Fe-Si films were scanned in non-contact mode.

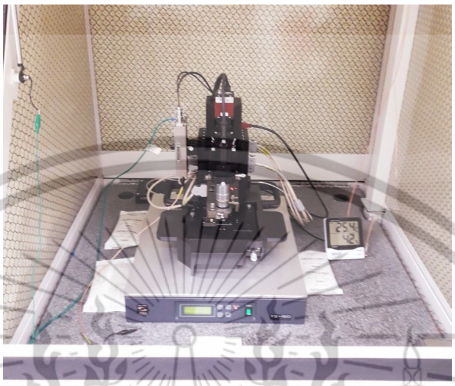

Figure 3.13 AFM apparatus (Park system, XE-120).

3.4.5 Contact angle measurement

To observe the wetting behaviors of the Fe-Si films prior and after the modification process, the θ_{CA} values of dropped deionized water on the surface of films were captured by contact angle analyzer (model: OCA 20), as shown in Figure 3.14. In this measurement method, the deionized water was dropped from a syringe with a volume of 5 μl under liquid dosing rate of 1 μl/s. Images of the drop on the film surface were captured by a camera on the instrument. The contact angle values were analyzed through built-in SCA 20 Software.

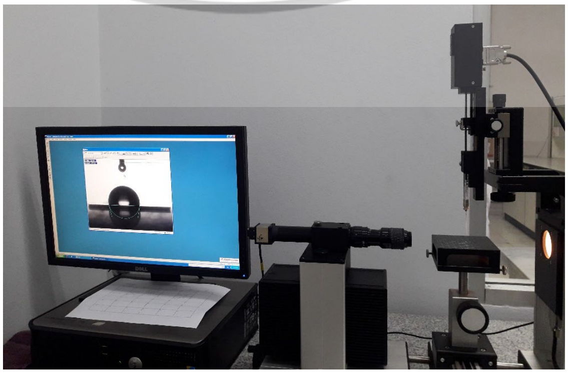

Figure 3.14 OCA20 Optical contact angle analyzer and a computer with SCA 20.

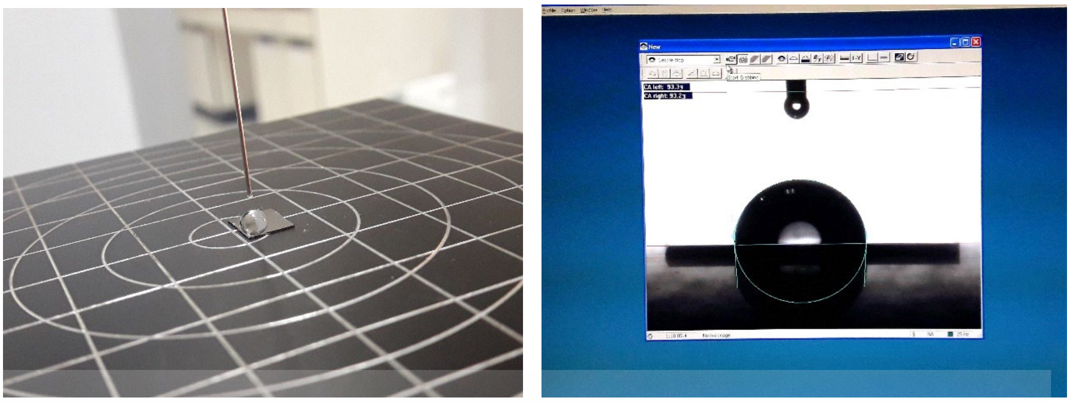

(a) (b)

Figure 3.15 Drop on the surface of films in (a) visible view and (b) software view to demostrate estimated θ_{CA} values.

3.4.6 Mechanical investigation

The mechanical traits for the surface of as-created and modified Fe-Si films produced via FTDCS were investigated through a nanoindentaion test with a Berkovich indenter's tip. (Bruker Hysistron, model Ti Primier) at National Nanotechnology Center, as portrayed in Figure 3.16.

Figure 3.16 Nanoindentation machine (Bruker Hysistron, model Ti Primier).

Chapter 4

Results and discussion

4.1 Effect of bias voltage on n-$FeSi_2$/p-Si devices formed via FTDCS

Based on the various parameters reported in previous studies, the fabricated p-Si/n-NC-$FeSi_2$ and p-Si/n-β-$FeSi_2$ heterostructures can be represented by the band diagrams shown in Figure 4.1 [93-95]. The Fermi level of n-type $FeSi_2$ is located near the conduction band due to the high carrier concentration and shallow donor levels [93-95]. The built-in potential (V_{bi}) of the junction is about 1.02 eV, which is reasonable for a heterojunction. However, the valence band offset (ΔE_v) hinders hole transport, and the transport occurs mainly through the interface states, especially when the interface is not ideal [93-95]. This leads to the formation of band spikes at the interface due to imperfect bonding and lattice mismatch [93-95]. In both structures, the depletion region mainly extends to the p-Si side due to its lower carrier concentration [96]. When a reverse bias is applied, the built-in potential increases and the band bending near the interface becomes more pronounced [97]. This causes the depletion region to extend further, increasing the barrier to carrier transport [97]. As a result, minority carrier injection is more suppressed, the potential well for electrons in n-type $FeSi_2$ becomes deeper, and thermionic emission becomes more difficult [97]. The interface state density (N_{ss}) has been previously evaluated from the frequency-dependent capacitance-voltage (C–V) and conductance-voltage (G–V) characteristics, and it acts as a carrier trapping center under reverse bias, which can also cause leakage current [10]. The N_{ss} is estimated to be 3.48×10^{12} $eV^{-1}{\cdot}cm^{-2}$ at 1 MHz and 4.68×10^{11} $eV^{-1}{\cdot}cm^{-2}$ at 5 kHz [10], and in particular, NC-$FeSi_2$ has a very high N_{ss} of 2.70×10^{14} $eV^{-1}{\cdot}cm^{-2}$ at 60 kHz, and shows a tendency to exponentially decrease with increasing frequency up to 2 MHz [98]. Due to the high N_{ss} of NC-$FeSi_2$, the local band fluctuations and inhomogeneity of the electric field were presence across the junction [98]. In addition, the high carrier density of NC-$FeSi_2$ slightly raises the conduction threshold, resulting in a slightly wider effective band gap (about 0.87 eV) [95, 97]. The carrier density may increase the resistance to carrier injection from the Si side hence larger space charge region. Overall, the application of reverse bias makes the electronic inhomogeneity at the interface more pronounced, and the influence of the interface states and doping profile on device operation becomes more pronounced.

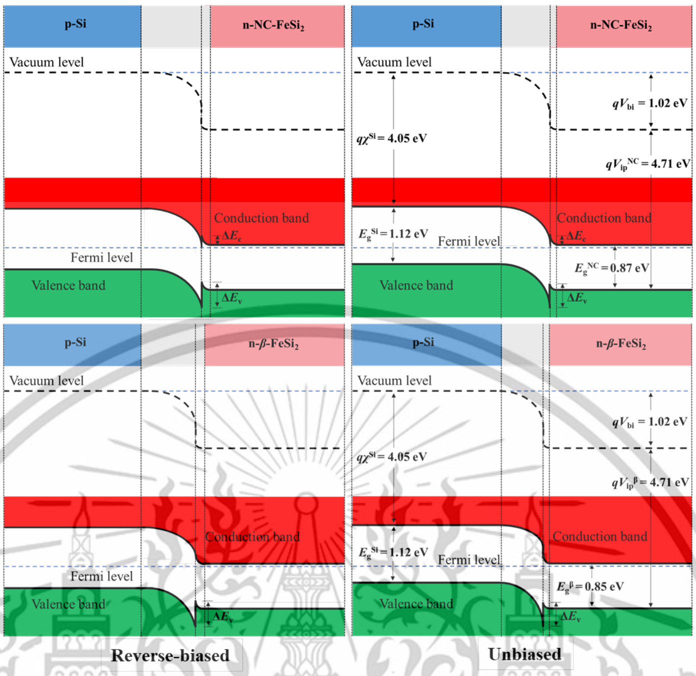

Figure 4.1 Band diagram behavior of -1 to 0 V of *p*-Si/*n*-NC-FeSi$_2$ heterojunctions and *p*-Si/*n*-*β*-FeSi$_2$ heterojunctions.

4.1.1 Impedance spectroscopy of n-FeSi$_2$/p-Si devices under voltage

In Figure 4.2(a), as voltage increases in the low frequency region, magnitude of *Z'* decreases and the *Z'* value trend downward with *f* until *f* reaching about 500 kHz and then becomes almost constant. On the other hand, *Z'*-*f* result of fabricated *β*-FeSi$_2$ heterojunction also shown similar behavior but *Z'* is almost constant regardless of bias voltage at *f* above 10 kHz instead. These trends are attributed to the release of space charge polarization due to the bias change [74]. The two plateau regions at low and high *f* indicate the existence of two types of resistance components [99, 100]. In the low frequency region, R_s due to the ohmic contacts, electrodes, and bulk is dominant, while in the high frequency region, R_p corresponding to the charge transfer resistance is dominant [99, 100]. In Figure 4.2(b), a relaxation peak appears at *Z"* for all voltage conditions. This peak shifts to the high frequency side as voltage increases, and the magnitude of the peak also decreases from 8.824 kΩ to 1.294 kΩ. Meanwhile, the peak at -1 V is around 1.896 kΩ, then decreases to about 250.171 Ω at 0 V for *β*-FeSi$_2$ heterojunction. From this, it is inferred that the *Z”* response shows bias-dependent electrical relaxation behavior and is non-Debye type due to the wide distribution of relaxation times (τ) which shorten by voltage [101,102]. *Z”* increases with increasing frequency and decreases after passing the peak. At higher *V*, *Z”* becomes smaller at low frequencies and shows a convergence tendency at *f* above 1 MHz for NC-FeSi$_2$ heterojunction and at *f* region above 100 kHz *β*-FeSi$_2$ heterojunction. This is likely related to the space charge polarization caused by the transfer of electrons from n-FeSi$_2$ side to the space charge region of p-Si [100, 101].

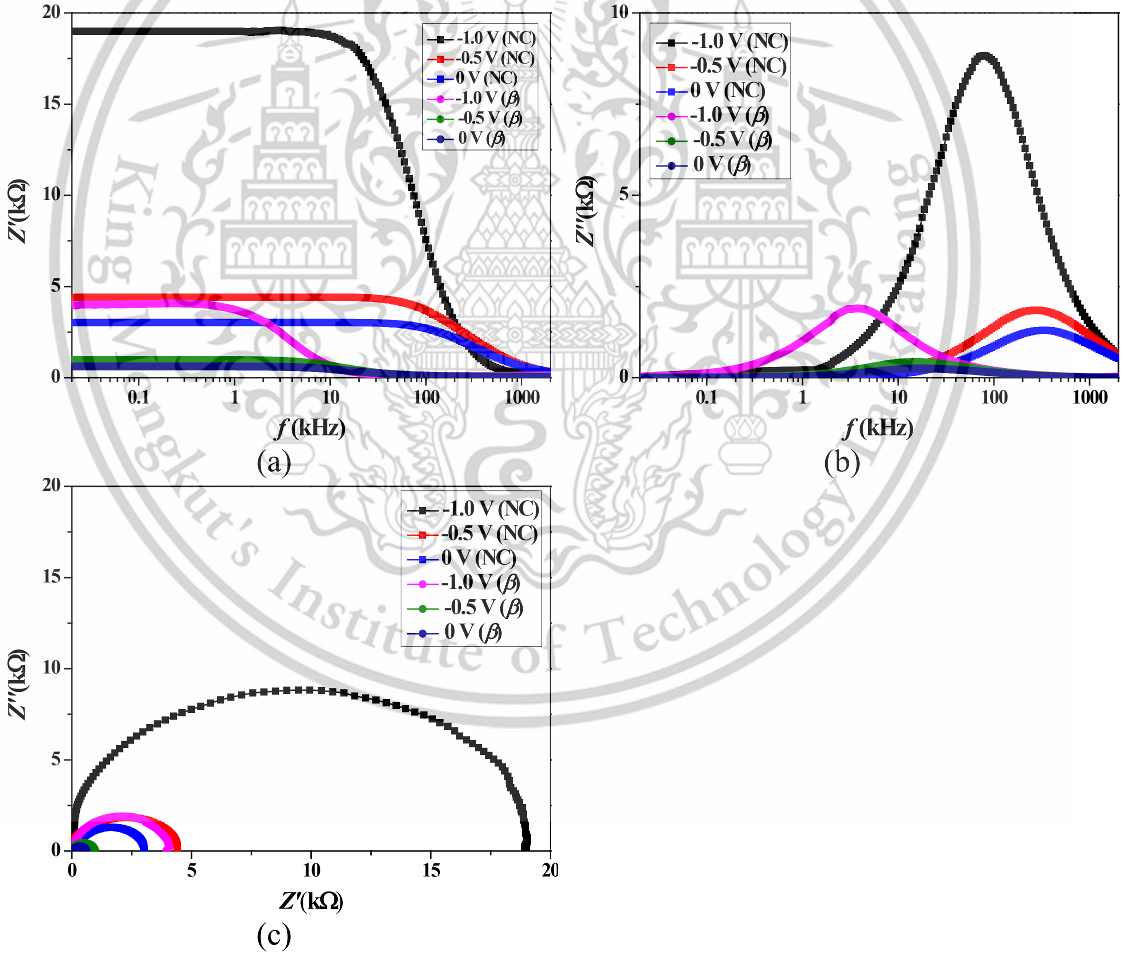

(a)

(b)

(c)

Figure 4.2 (a) *Z’*-*f* and (c) *Z”*-*f* under the variation of applied voltage for *p*-Si/*n*-NC-FeSi$_2$ heterojunctions along side (b) *Z’*-*f* and (c) *Z”*-*f* for *p*-Si/*n*-*β*-FeSi$_2$ heterojunctions.

The τ value is defined as the reciprocal of the frequency (f_{max}) of the maximum in the Z'' component of spectrum, which correlate to the time taken for the dielectric polarization, once disturbed by the conduction phenomenon, to return to equilibrium. τ value is an important parameter for evaluating the relaxation process and the transport properties of charge carriers. It also indicates how the dielectric polarization decays with time as result of the application of an AC electric field [103,104]. The value of τ can be calculated based on a Z''-f plot using the following relationship [105]:

$$\tau = 1/\omega_{\max} = 1/2\pi f_{\max} \tag{4.1}$$

where ω_{max} represents the maximum relaxation angular frequency, f_{max} denotes the maximum relaxation frequency, and τ shows the carrier relaxation time value.

Figure 4.3 shows the estimated τ of p-Si/n-NC-FeSi$_2$ heterojunctions at applied voltage from -1V to 0V. At -1V, τ was calculated to be around 1.999 μs, then τ was significantly reduced to 0.427 μs at 0V. Figure 4.3 also shows the applied voltage dependency of τ for the p-Si/n-β-FeSi$_2$ heterojunction. The longest τ was 4.223×10^{-5} s at -1 V, and the shortest was 1.190×10^{-5} s at 0 V. The higher τ of may orginated from higher polarisability. With increasing bias V, the τ of the mobile charge carriers decreases, suggesting that the release of space charges at high voltage ranges is promoted [99]. This is due to the fast charging and discharging of electrons at the interface between the n-type FeSi$_2$ thin film and the p-type Si substrate, which accelerates the exciton generation at the interface and the charge transport in the active layer [99].

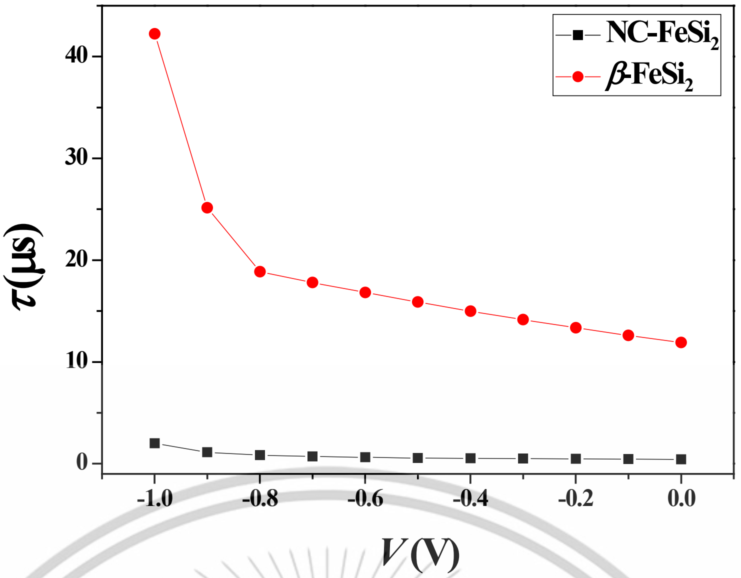

Figure 4.3 Relationship between τ vs the applied voltage for the formed *p*-Si/*n*-NC-FeSi$_2$ and *p*-Si/*n*-β-FeSi$_2$ heterojunctions.

Figure 4.4(c) presents Nyquist plots (Z'' vs Z') for bias voltage ranging from 0 V to –1 V for *p*-Si/*n*-NC-FeSi$_2$ heterojunctions and 0 V to -1 V for *p*-Si/*n*-β-FeSi$_2$ heterojunctions. In all cases, the frequency decreases from left to right. Each plot forms a single semicircular arc, indicating a dominant single relaxation process within the heterostructures [99]. At lower *V*, the arc becomes smaller, suggesting a decrease in charge transfer R_p and thus improved electrical conduction due to increased carrier activation. Frequency shifts from right to left, reaffirming the presence of a single relaxation mechanism across all temperatures [99]. These observations are well-explained by the equivalent circuit model shown in Figure 4.4, which includes a R_s in combination with three parallel R_p–CPE circuits. These circuits represent contributions from the grain interior (R_g–CPE$_g$), grain boundary (R_{gb}–CPE$_{gb}$), and junction interface (R_j–CPE$_j$) [90]. R_s accounts for resistance from the electrodes and ohmic contact. Each R_p represents resistance due to charge transport at a specific structural region, while the constant phase elements (CPEs) model non-ideal capacitive behavior caused by microstructural inhomogeneities [90]. The impedance of a CPE is described by the following function [106]:

$$Z(\omega) = Z' - iZ'' = R_s + \frac{i}{\omega CPE} \tag{4.2}$$

where

$$Z' = \frac{R_{\mathrm{g}}}{\left(\omega CPE_{\mathrm{g}} R_{\mathrm{g}}\right)^2 + 1} + \frac{R_{\mathrm{gb}}}{\left(\omega CPE_{\mathrm{gb}} R_{\mathrm{gb}}\right)^2 + 1} + \frac{R_{\mathrm{j}}}{\left(\omega CPE_{\mathrm{j}} R_{\mathrm{j}}\right)^2 + 1} + R_{\mathrm{s}} \tag{4.3}$$

$$Z'' = \frac{\omega CPE_{\mathrm{g}} R_{\mathrm{g}}^2}{\left(\omega CPE_{\mathrm{g}} R_{\mathrm{g}}\right)^2 + 1} + \frac{\omega CPE_{\mathrm{gb}} R_{\mathrm{gb}}^2}{\left(\omega CPE_{\mathrm{gb}} R_{\mathrm{gb}}\right)^2 + 1} + \frac{\omega CPE_{\mathrm{j}} R_{\mathrm{j}}^2}{\left(\omega CPE_{\mathrm{j}} R_{\mathrm{j}}\right)^2 + 1} \tag{4.4}$$

Here, R_s is a series resistance. R_g, R_{gb}, and R_j are the R_{p} of the crystallite grain, boundary between the grains, and junction‘s interface. CPE_g, CPE_{gb}, and CPE_j are the imperfect capacitance of the crystallite grain, boundary between the grains, and junction‘s interface. ω is an angular frequency. i is an imaginary element. Finally, n parameter ranges from 1 for ideal capacitor to 0 for pure resistor.

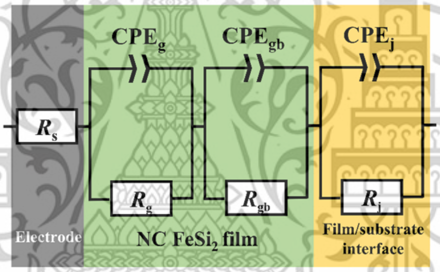

Figure 4.4 An equivalent circuit for both p-Si/n-NC-FeSi$_2$ heterojunctions and p-Si/n-β-FeSi$_2$ heterojunctions.

To extract the equivalent circuit parameters from the Nyquist plot of p-Si/n-NC-FeSi$_2$ heterojunctions, nonlinear least-squares fitting was performed using EC-Lab software. As shown in Figure 4.5(a), the R_{s} decreased with the reverse bias from –1 V to 0 V with p-Si/n-β-FeSi$_2$ heterojunctions has slightly lower value likely due to less defect. This can be attributed to the decrease in contact resistance and the improvement of charge transport at 0 V [107]. The R_{g}, R_{gb}, and R_{j} also decreased with increasing bias voltage, suggesting the promotion of electron transfer and the improvement of carrier mobility [99]. Meanwhile, the CPE parameters (CPE$_{\mathrm{g}}$, CPE$_{\mathrm{gb}}$, and CPE$_{\mathrm{j}}$) all exhibited capacitive behavior with n values close to 1. The magnitude of the CPE is in the nF range for CPE$_{\mathrm{gb}}$ and in the pF range for CPE$_{\mathrm{g}}$ and CPE$_{\mathrm{j}}$. These results are consistent with other studies on nanocrystalline materials such as ZnS nanoparticles [74], and α-CuSCN [71], supporting the nanocrystalline nature of the *p*-Si/*n*-NC-FeSi$_2$ heterostructure. The increase in the CPE value with the change from −1 V to 0 V can be attributed to the reduction in the depletion layer width and the increase in charge accumulation at the transport layer/active layer interface. These decreases in R_p and increases in CPE indicate improved conductivity with increasing bias [12,13]. Similarly, the R_g, R_{gb}, and R_j also decrease with increasing voltage. However, the values for *p*-Si/*n*-β-FeSi$_2$ heterojunctions are significantly lower do to lack of grain boundary and interface state. As for the CPE, the exponents *n* of CPE$_g$, CPE$_{gb}$, and CPE$_j$ are all close to 1 throughout the voltage range, indicating nearly ideal capacitance. The CPE values also show the same trend with more reverse voltage but with lower magnitude likely due to aforenoted longer τ value.

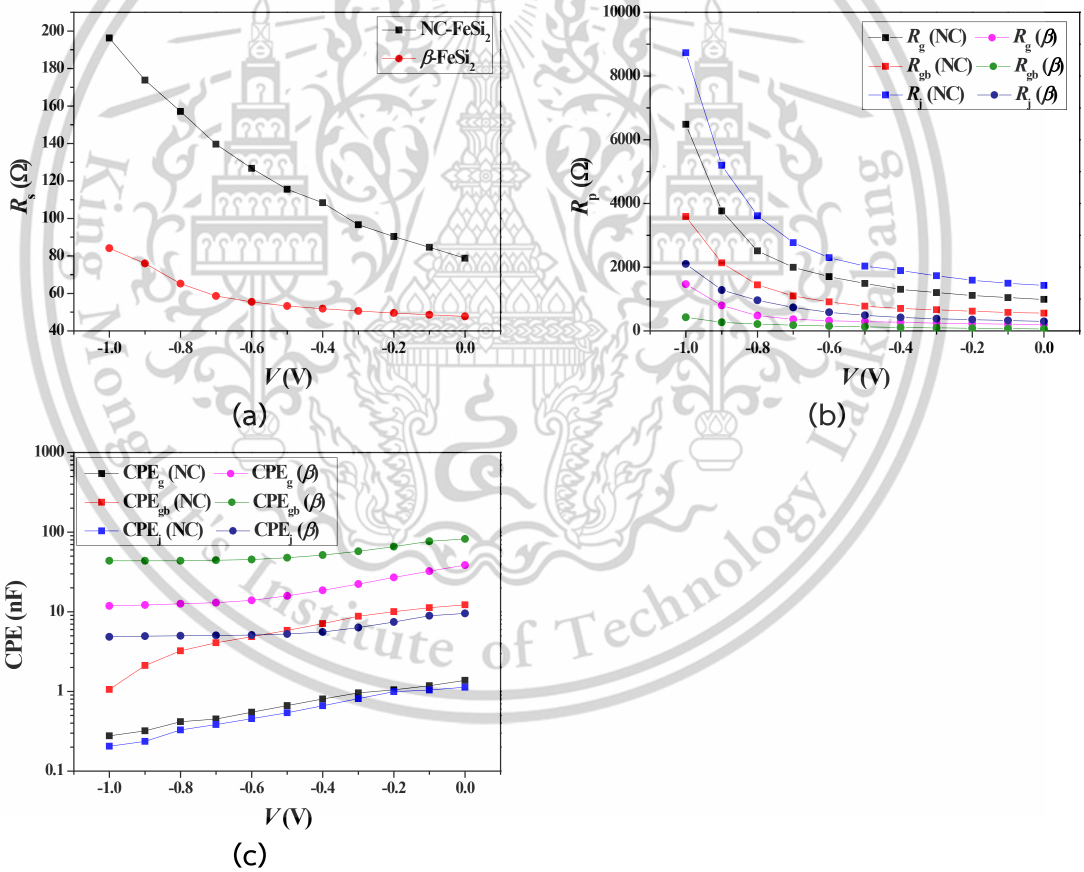

(a) (b)

(c)

Figure 4.5 Comparison of each type of fitted (a) R_s and (b) R_p characteristics of the manufactured *p*-Si/*n*-NC-FeSi$_2$ and *p*-Si/*n*-β-FeSi$_2$ heterojunctions monitored by changing the temperature. Figure (c) is trend of CPE at different temperatures for *p*-Si/*n*-β-FeSi$_2$ heterojunctions.

4.1.2 Dielectric properties of n-FeSi$_2$/p-Si devices under voltage

Figure 4.6(a) shows that the real part of the ε' of the fabricated p-Si/n-NC-FeSi$_2$ heterostructures remains high and nearly independent of frequency at low *f*. At 100 Hz, ε' was 20.216 at −1 V and 86.696 at 0 V, indicating enhanced dielectric response under zero bias. At the characteristic frequency (fc = 1/2$\pi\tau$), ε' dropped to 4.16 (−1 V) and 5.54 (0 V). This behavior is well explained by the Maxwell-Wagner polarization model, where conductive grains separated by resistive grain boundaries lead to space charge accumulation at interfaces [72,73]. At low *f*, migrating carriers accumulate at these boundaries, increasing ε' [72,73]. As frequency rises, the ability of dipoles to follow the external field diminishes, leading to charge relaxation and a sharp decrease in ε' [72,73]. In comparison, the ε' of *p*-Si/*n*-β-FeSi$_2$ heterojunctions forms a broad plateau at *f* below 10^4 Hz. At 100 Hz, ε' reaches 612.306 at 0 V and 441.982 at -1 V. When the *f* exceeds 10^4 Hz, the charge carriers are unable to keep up with the rapid change in the electric field, and ε' drops sharply. This suggests that the interfacial polarization due to charge accumulation at grain boundaries and interfaces is also dominant but *p*-Si/*n*-β-FeSi$_2$ heterojunctions have better polarizability.

As shown in Figure 4.6(b), the frequency dependence of the tan δ plot for *p*-Si/*n*-NC-FeSi$_2$ heterojunctions has trend of high magnitude at low frequencies and decreasing steadily as frequency increases. Since tan δ is defined as the ratio of ε'' to ε', it reflects both resistive losses from mobile charges and relaxation losses from dipolar alignment [70]. The high value of tan δ in low *f* range mean ε'' values of *p*-Si/*n*-NC-FeSi$_2$ heterojunctions were 2 magnitudes higher than ε', reflecting dominant dielectric loss due to conduction [70]. At low frequencies, space charges accumulate at grain boundaries, enhancing interfacial polarization [70]. However, as frequency increases, carrier mobility is hindered, suppressing polarization and reducing tan δ [70]. A shoulder peak observed around 10^3–10^4 Hz may indicate carrier hopping under the influence of the electric field [109]. The high tan δ values at low frequencies also suggest a leaky capacitive nature of the heterojunction [73]. The decrease in ε' and tan δ under reverse bias is likely due to reduced interface density [71]. The tan δ–*f* curve of *p*-Si/*n*-β-FeSi$_2$ heterojunctions also reflects the interfacial polarization due to the accumulation of space charges based on the Maxwell-Wagner effect [73]. As the f increases, the carrier movement is restricted and the tan δ value decreases, but it increases again above 10^5 Hz, suggesting absorption due to dipolar relaxation [73]. Overall, the tan δ value is high and there is a certain degree of leakage, but it is lower than that of the nanocrystalline system. Regardless, the change in dielectric properties due to the bias voltage is mainly due to the accumulation of interface states [71].

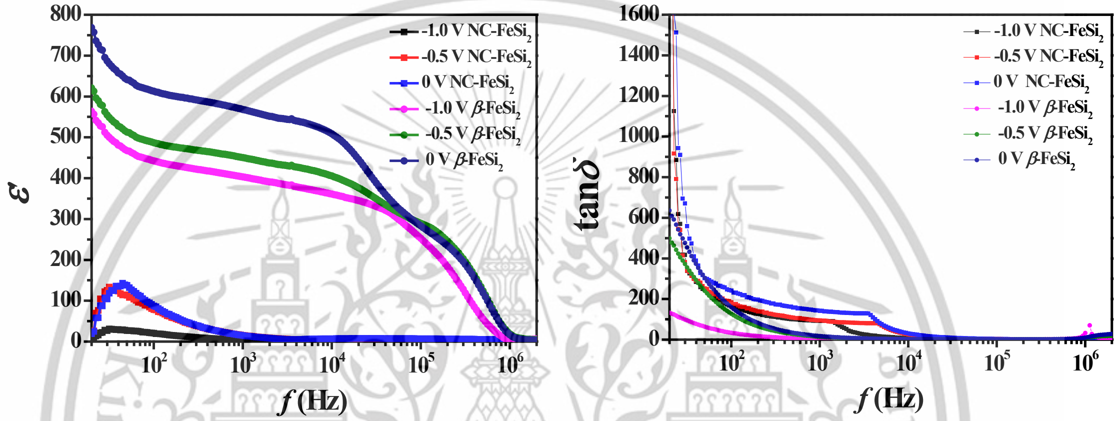

(a) (b)

Figure 4.6 The (a) ε'-f and (b) tan δ-f plot at various voltage variances for the formed *p*-Si/*n*-NC-FeSi$_2$ and *p*-Si/*n*-β-FeSi$_2$ heterojunctions.

4.1.3 Conductivities of n-FeSi$_2$/p-Si devices under voltage

Figure 4.7 reveals the dependent plot of estimated σ_{AC} value for the formed heterostructures extracted from impedance parameters.

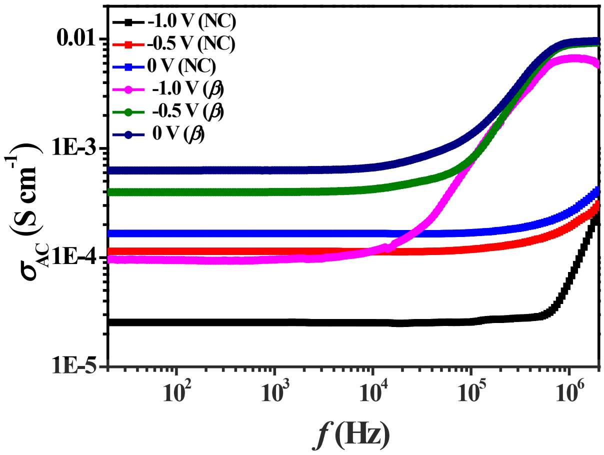

Figure 4.7 (a) The tan σ_{AC}-f plot at various voltage variances for the formed (a) p-Si/n-NC-FeSi$_2$ and (b) p-Si/n-β-FeSi$_2$ heterojunctions.

The frequency dependence of σ_{AC} is explained by combining the Maxwell-Wagner effect and Jonscher's universal power law [70,73]. At low frequencies, σ_{AC} is a constant value that shows little change with frequency. At this time, the applied electric field is weak enough to drive the polarization, and the charge carriers cannot hop to neighboring sites and tend to remain at the grain boundaries [70,73]. In this state, the AC conductivity is considered to be essentially dominated by the σ_{DC} [70,73]. On the other hand, as the frequency increases, the polarization response cannot keep up with the change in the electric field, and the carriers start hopping between localized states [70,73]. As a result, σ_{AC} increases with frequency, reflecting the improvement of the charge mobility [102]. To better understand this frequency response, a jump relaxation model is also used [102]. In this model, carriers move within a "cage effect" that results from the superposition of a potential formed by Coulomb interactions with a periodic potential of the crystal lattice [102]. The idea is that this potential structure affects the carrier jumps and contributes to the frequency dependence of AC conduction [102].

The σ_{DC} value at each applied voltage was calculated by extrapolating a straight line from the low f plateau of the σ_{AC} vs. f plot to the y-axis. At a reverse bias of -1 V, σ_{DC} was 2.666×10^{-5} S·m^{-1}, but when the bias was returned to 0 V, it increased to 1.656×10^{-4} S·m^{-1}. The decrease in σ_{DC} with increasing reverse bias is attributed to the expansion of the depletion layer, which reduces the majority carriers, and the higher potential barrier hinders carrier movement [109]. As shown in Figure 4.8(b), the frequency index *S* was 2.791 at -1 V and 1.390 at 0 V, decreasing with decreasing bias. All *S* values are greater than 1, indicating that carriers hop locally within adjacent sites, and that short-range transport is dominant, rather than long-range [70,73]. *S* of *p*-Si/*n*-β-FeSi$_2$ heterojunctions is greater than 1 for all conditions, being 1.607 at –1 V and 1.350 at 0 V. This suggests that the charge carriers move mainly by local hopping confined within adjacent sites. Meanwhile, the calculated σ_{DC} reflects the conduction component due to long-range hopping of carriers to unoccupied states. At –1 V, σ_{DC} is estimated to be 9.491 × 10^{-3} S·cm^{-1}, and when the reverse bias voltage is decreased to 0 V, the carriers accumulate and σ_{DC} also increases to 6.290 × 10^{-2} S·cm^{-1}. The higher conductivities of *p*-Si/*n*-β-FeSi$_2$ heterojunctions might be due to narrower depletion region and higher carrier mobility [109].

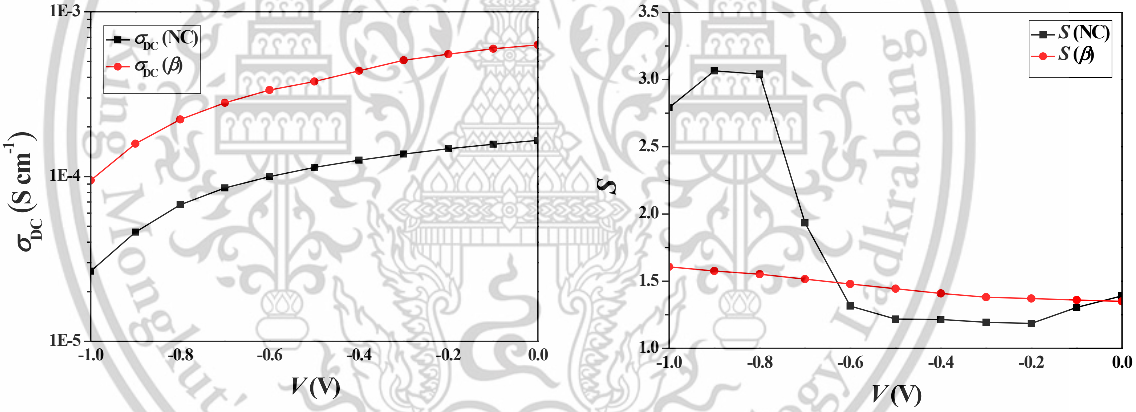

(a) (b)

Figure 4.8 (a) The σ_{DC}-*f* plot and (b) the *S* plot under varying voltage ranges for n-NC-FeSi$_2$/p-Si devices along side n-β-FeSi$_2$/p-Si devices.

4.2 Effect of temperature on n-FeSi$_2$/p-Si devices formed via FTDCS

Based on the reported parameters from former works, the band diagram of formed p-Si/n-NC-FeSi$_2$ and p-Si/n-β-FeSi$_2$ heterojunction devices can be represented as seen in Fig. 4.9 [93-95]. The Fermi level of the n-FeSi$_2$ is placed near the conduction band's level due to its shallow donor level as well as excess carrier density [93-95]. At around room temperature (300 K), the FeSi$_2$ possess the respectable V_{bi} value of is roughly 1.02 eV. However, the ΔE_v of the $FeSi_2$ forces the transmission of holes to rely on the imperfect interface states instead since the photogeneration process was disrupted leading to formation of spike on the valence band [93-95]. Early appearance of band offset on conduction band with conduction band potential (ΔE_C) is spotted due to a more pronouncing band bending effect from numerous nanocrystallites that present [55]. The Si side dominated the depletion layer of the p-Si/n-$FeSi_2$ heterostructures [93-95]. The source of the device's performance degradation that is N_{ss} value of the p-Si/n-$FeSi_2$ heterostructures acts as a trapping mechanism for the photo-generated carriers. Similar to what mentioned on the diagram in the voltage segment, higher N_{ss} value of NC-$FeSi_2$ also increase trap center inside the devices hence space charge region of Si-*p*/NC-$FeSi_2$-*n* heterostructures should be slightly wider [96]. At the same time higher carrier density of NC-$FeSi_2$ also raise conduction band energy level hence slightly higher base energy gap of 0.87 eV [95,97]. At lower temperatures, the both of the bands (valence and conduction) place slightly slower while valence and conduction band potential may raise [98]. At the same time, the band bending effect become more pronounce due to slower vibration of particle and less free electron, leading to band offset at conduction band appear for both devices [98]. The space charge region also widens at lower temperature from afore mentioned slower particle vibration. On the opposite end, the band bending should be subdued alongside narrower depletion region at higher temperatures [97]. Regardless, the energy band on n-$FeSi_2$ side should be rarely exhibit temperature dependence as the extra electron that being trapped should made the n-$FeSi_2$ thermal stable [110].

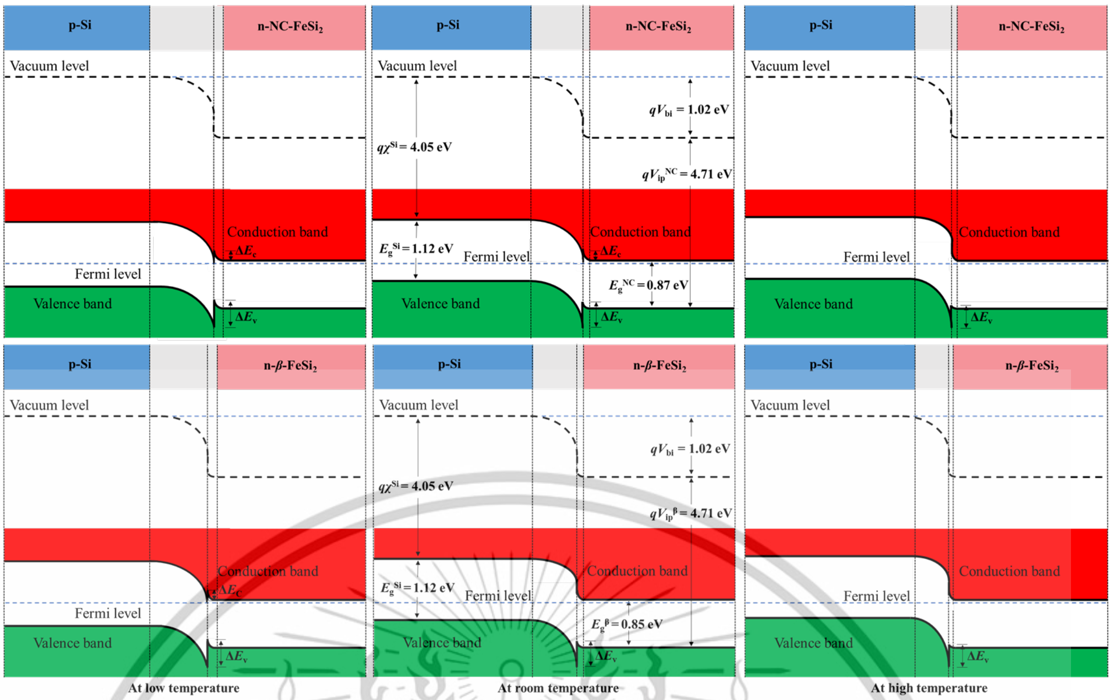

Figure 4.9 Band diagram behavior of 400 to 160 K of *p*-Si/*n*-NC-FeSi$_2$ heterojunctions and *p*-Si/*n*-*β*-FeSi$_2$ heterojunctions.

4.2.1 Impedance spectroscopy of n-FeSi$_2$/p-Si devices under temperature

The Figure 4.10 impedance responses for n-NC-FeSi$_2$/p-Si devices are similar to those reported for ferrites by K. Chandra et al., which show that increasing temperature reduces the bound charge density and increases mobility, thereby decreasing the impedance [110]. Figure 4.10(a), (c), and (e) shows the relationship between *Z'* and frequency measured under temperatures from 160 K to 400 K. With increasing *T*, the *Z'* value in the low *f* region decreases, but rarely change at high *f* above 10 kHz. This is interpreted as a result of a decrease in resistance due to thermally excited carriers and reduction of space charge's influence [112]. Figure 4.10(b) shows the relationship between *Z"* and *f* in the same temperature range. With increasing *T*, the *Z"* peak becomes smaller and shifts to higher *f* range. Namely, the peak value at 160 K is 21.8 kΩ (317 Hz) and decreases to 8.8 Ω (106 kHz) at 400 K. At all temperature ranges, the peak shape is asymmetric, indicating a non-Debye characteristic due to the distribution of relaxation times in the *p*-Si/*n*-FeSi$_2$ heterostructures [113]. 400 K, the impedance of the n-NC-FeSi$_2$/p-Si heterojunction is higher than that of the n-Beta-FeSi$_2$/p-Si junction due to the presence of abundant interface states and grain boundaries in NC-FeSi$_2$, which trap carriers and hinder transport despite its higher carrier density [98]. In contrast, the fully crystalline Beta-FeSi$_2$ formed at 600 °C allows more efficient band conduction at these temperatures [95]. However, at 160 K, the impedance trend reverses: Beta-FeSi$_2$ exhibits higher impedance than NC-FeSi$_2$. This is attributed to carrier delay in the crystalline phase, where the lack of mid-gap states or alternative conduction paths suppresses charge transport [114,115]. Meanwhile, NC-FeSi$_2$ retains lower impedance due to tunneling and hopping conduction across its disordered grain boundaries and defect-rich interfaces hence mechanisms that remain active at low temperatures and frequency [sees inset of Figure 4.10 (b)) without requiring thermal activation [114,115]. This behavior aligns with earlier reports suggesting tunnel-assisted transport in FeSi$_2$ nanostructures from N. Promros who computed ideality factor of the junction to be higher than 2 at low temperature suggesting presence of tunnel effect [11].

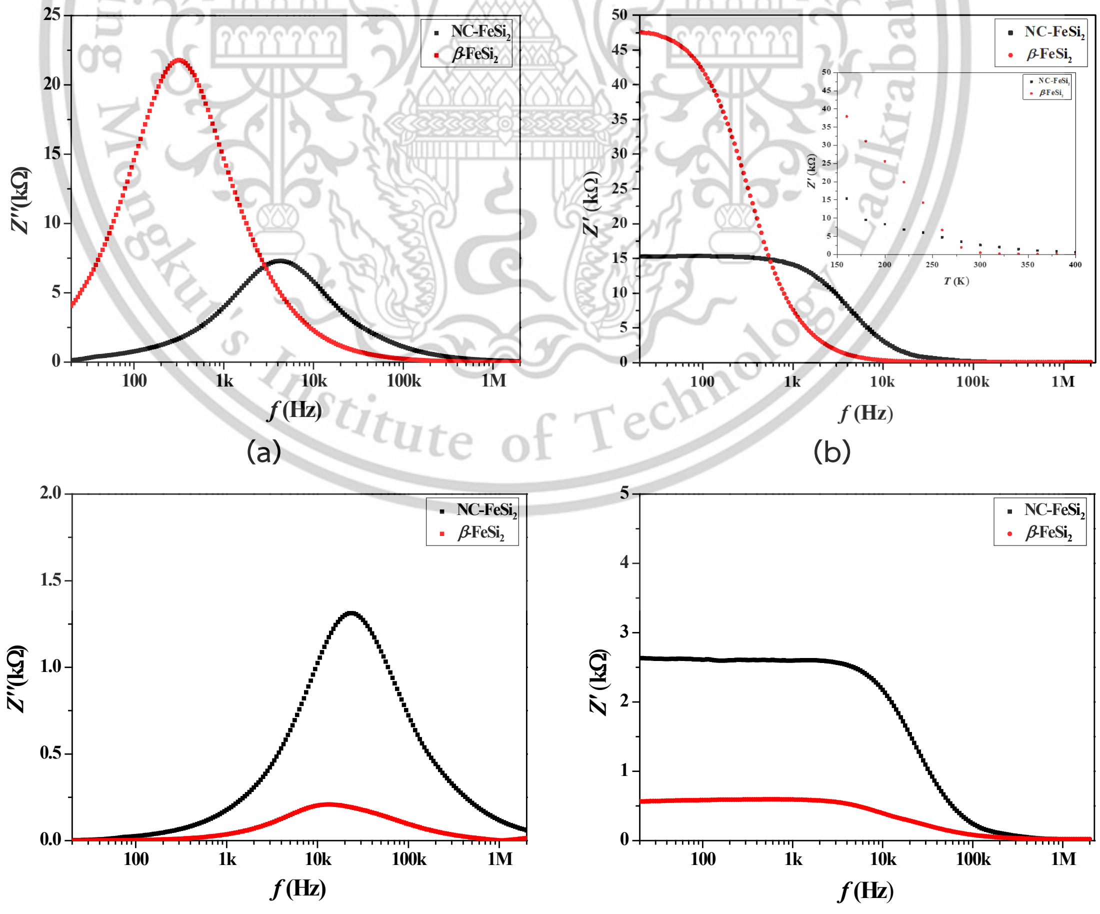

(a) (b)

(c) (d)

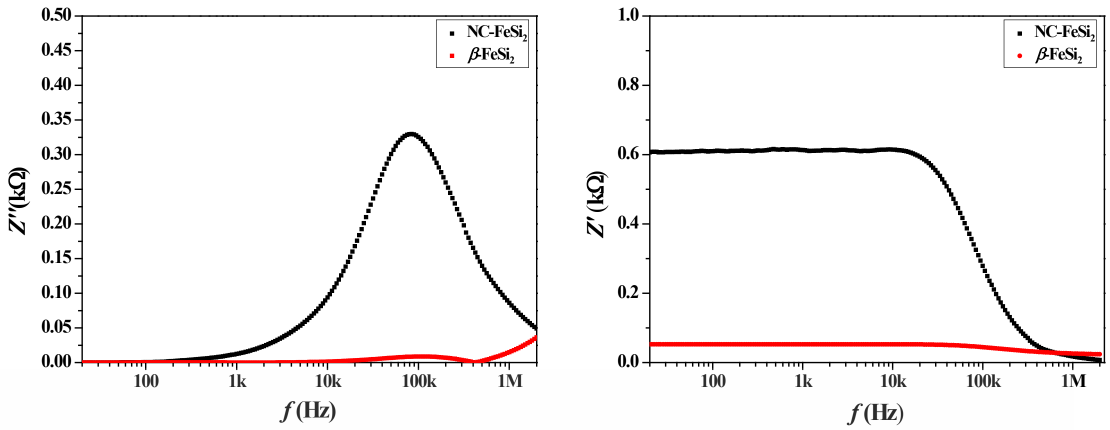

(e) (f)

Figure 4.10 (a) the Z' characteristics and (b) Z'' vs f in the low temperature range of 160 K and (c) Z' and (d) Z'' plot under room temperature of 300 K then (e) Z' and (f) Z'' plot under high temperature of 400 K of p-Si/n-NC-FeSi$_2$ heterojunctions.

Regarding the temperature dependence, the peak value of Z'' appeared at different frequencies, namely, 7.3 kΩ at around 2.2 kHz at 160 K and 330 Ω at 106 kHz at 400 K. These changes suggest that $\boldsymbol{\tau}$ is highly dependent on temperature. As shown in Figure 4.11(a), $\boldsymbol{\tau}$ increases from 1.89×10^{-6} s at 400 K to 3.77×10^{-5} s at 160 K. This shows that the lower the temperature, the fewer the number of excited carriers due to the decrease in thermal energy, and as a result, the longer it takes to relax [10]. Figure 4.11(b) shows the temperature dependency of the $\boldsymbol{\tau}$. At 160 K, $\boldsymbol{\tau}$ is approximately 5.02×10^{-4} s. With increasing T, $\boldsymbol{\tau}$ rapidly decreased to 1.5×10^{-6} s at 400 K. This result indicates that at high temperatures, many charge carriers are activated by thermal energy, shortening the carrier relaxation time [10]. Still, $\boldsymbol{\tau}$ values of the p-Si/n-NC-FeSi$_2$ are shorter than $\boldsymbol{\tau}$ values of p-Si/n-β-FeSi$_2$ heterojunctions. As trap interface energized this led to shallower band gap and reduce band bending seen in band diagram which improve conductivity [10].

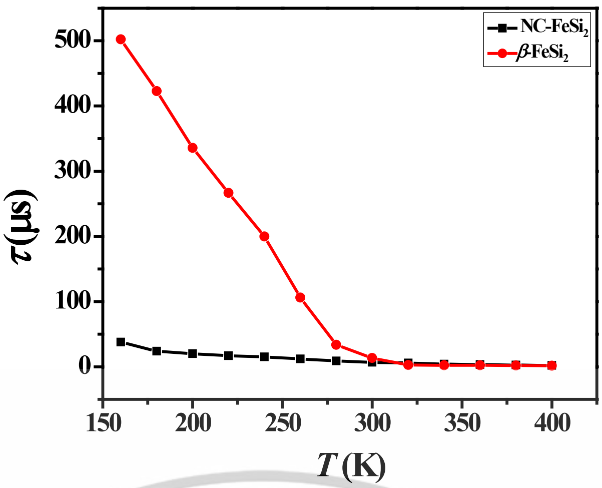

Figure 4.11 Relationship between τ vs temperature for the formed p-Si/n-NC-FeSi$_2$ and p-Si/n-β-FeSi$_2$ heterojunctions.

Figures 4.12 (a-c) show Nyquist plots of p-Si/n-NC-FeSi$_2$ heterojunctions measured under different temperatures, from 160-400 K, at a fixed bias of 0.01 V. All plots display a single semicircle, which increases in size as temperature decreases, indicating that resistance rises with decreasing thermal energy. Frequency shifts from right to left, reaffirming the presence of a single relaxation mechanism across all temperatures. Such behavior can be adequately described by the same equivalent circuit model shown in the voltage experiment section. Meanwhile, Z''–Z' characteristics of p-Si/n-β-FeSi$_2$ heterojunctions presents distinct a single semicircular arc but with slightly curled at the tail end. This curly end indicates inductive element likely from lack of mid-gap states or alternative conduction paths to response to signal of p-Si/n-β-FeSi$_2$ heterojunctions [116,117]. The size of these arcs diminishes as temperature rises, indicating a reduction in resistance likely caused by thermally activated charge carriers [114,115]. This temperature-dependent behavior is effectively described by an equivalent circuit consisting of a parallel configuration of R_p, a CPE, and an inductive branch (L + R_L), all connected in series with R_s. The corresponding circuit diagram is illustrated in the inset of Figure 4.12(d).

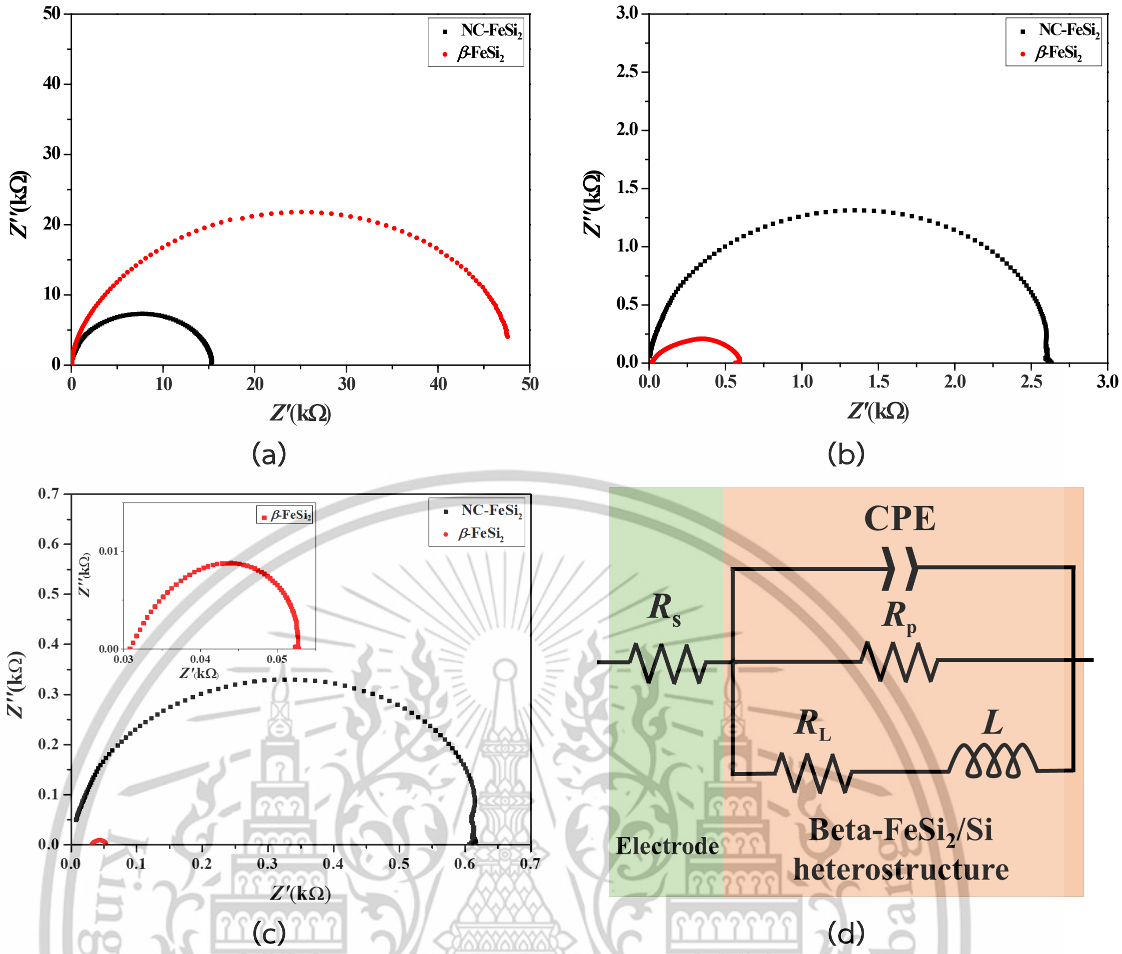

(a) (b)

(c) (d)

Figure 4.12 *Z”-Z’* characteristic curves of the manufactured *p*-Si/*n*-NC-FeSi$_2$ heterojunctions monitored by changing the temperature of (a) 160, (b) 300, and (c) 400 K. (d) equivalent circuit with inductive elements for *p*-Si/*n*-*β*-FeSi$_2$ heterojunctions.

The temperature dependence of data extracted the equivalent circuit parameters from the Nyquist plot shown in Figure 4.13(a) show that the R_s values of *p*-Si/*n*-NC-FeSi$_2$ heterojunctions remain low at 145 Ω at 160 K and 44.9 Ω at 400 K, indicating the formation of thermally stable ohmic contacts. At the same time, R_s *p*-Si/*n*-*β*-FeSi$_2$ heterojunctions is low at 21.0 Ω at 160 K and 49.6 Ω at 400 K, confirming the thermal stability of the ohmic contact in the *p*-Si/*n*-*β*-FeSi$_2$ heterojunctions. As the temperature increases, the carrier activation increases, promoting the transition and recombination processes, which leads to a tendency for the resistance values R_g, R_{gb}, and R_j to decrease [90]. In addition, the CPE values (CPE$_g$, CPE$_{gb}$, CPE$_j$) also increase due to the increased conduction activity caused by the increase in temperature, suggesting that the decrease in resistance due to heat increases the electrical conductivity of the entire *p*-Si/*n*-NC-$FeSi_2$ heterojunctions [90]. The *n* values corresponding to each CPE are all close to 1, indicating that these elements function as nearly ideal capacitors [90]. These fitting results are consistent with the typical characteristics seen in nanocrystalline materials [90]. It is generally known that in nanocrystalline materials, the capacitance of crystal grains and junction interfaces is on the order of pF, and the capacitance of grain boundaries is on the order of nF, confirming the presence of a nanocrystalline phase in the heterostructure [90]. For the *p*-Si/*n*-β-$FeSi_2$ heterojunctions, with increasing T, carrier excitation increases, promoting charge transfer and recombination, resulting in a decreasing trend in R_p and R_L. The CPE value also increases with increasing T, but the *n* value still remains near unity, supporting the capacitive interpretation [116]. Furthermore, the inductance (L) value at room temperature is consistent with that of the n-Si/polyaniline heterojunction reported by S. Ebrahim [118]. The increasing trend in L is attributed to the enhanced inductive effect due to the increased local fluctuations in electron density with increasing temperature, which in turn promotes the generation of dipoles in the bulk [118].

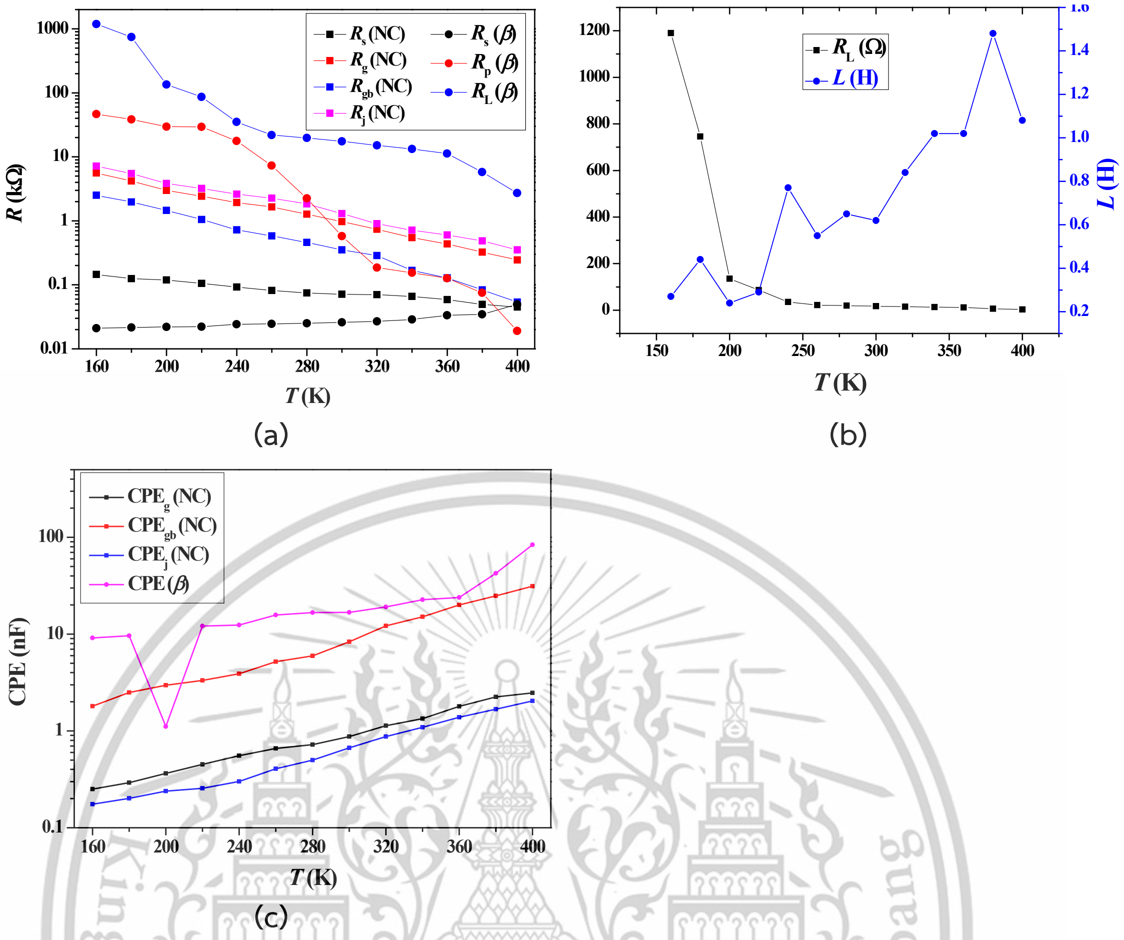

Figure 4.13 (a) comparison of each type of fitted *R* characteristic of the manufactured *p*-Si/*n*-NC-FeSi$_2$ and *p*-Si/*n*-β-FeSi$_2$ heterojunctions monitored by changing the temperature. (b) Trend of R_L and *L* while (c) are trend of CPE at different temperature values for *p*-Si/*n*-β-FeSi$_2$ heterojunctions.

4.2.2 Dielectric properties of n-FeSi$_2$/p-Si devices under temperature

The dielectric properties of the p-Si/n-NC-FeSi$_2$ and p-Si/n-β-FeSi$_2$ heterojunctions show different responses to frequency and temperature, reflecting the differences in their interfacial structures and band alignments. In the NC-FeSi$_2$ junction, the dielectric constant ε' at 100 Hz increases from 30.5 at 160 K to 191 at 400 K, due to the enhanced interfacial polarization caused by thermally excited carriers [119,120]. On the other hand, at high frequencies, ε' drops significantly, and ε'' dominates in the low-frequency region, indicating that Maxwell-Wagner relaxation at the grain boundaries is dominant. The dielectric loss tanδ increases slowly with temperature, rising from 13.5 to 58.9 at 100 Hz, but stabilizes at a low value of about 0.11 at 1 MHz, suggesting that NC-$FeSi_2$ is suitable for applications in high-frequency dielectric layers, filters, resonators, etc [121-123]. In contrast, the β-$FeSi_2$ junction exhibits a much higher dielectric response. At 100 Hz, ε' is 512 at 160 K and reaches 4,464 at 400 K. This is due to the sharp band offset and a strong built-in potential that effectively induces space charge polarization [119,120]. Tanδ also increases rapidly with temperature, reaching 891 at 400 K. However, at high frequencies, it shows stable values and stable performance can be expected for dielectric filters and sensing applications. For example, the ε' of NC-$FeSi_2$ at 300 K and 1 MHz is about 24.5, which is equivalent to lead oxide (PbO, $\varepsilon' \approx 25.9$), which is of concern for toxicity, and can be a more environmentally friendly alternative [123]. On the other hand, the high ε' of β-$FeSi_2$ is about half that of advanced supercapacitor materials such as carbon black and graphene oxide, indicating its potential as an energy storage material in harsh environments [124,125]. These differences are due to their respective band structures. NC-$FeSi_2$ has a high interface state density and a gentle band alignment that expands the space charge layer as seen in band diagram section, resulting in significant polarization due to trapping states. On the other hand, β-$FeSi_2$ has a steep band structure, which shows efficient carrier separation and high polarization effect. Therefore, β-$FeSi_2$ is promising for use in high-capacity capacitors and sensing devices, and NC-$FeSi_2$ is expected to be used in high-frequency electronics due to its stability and low-loss properties.

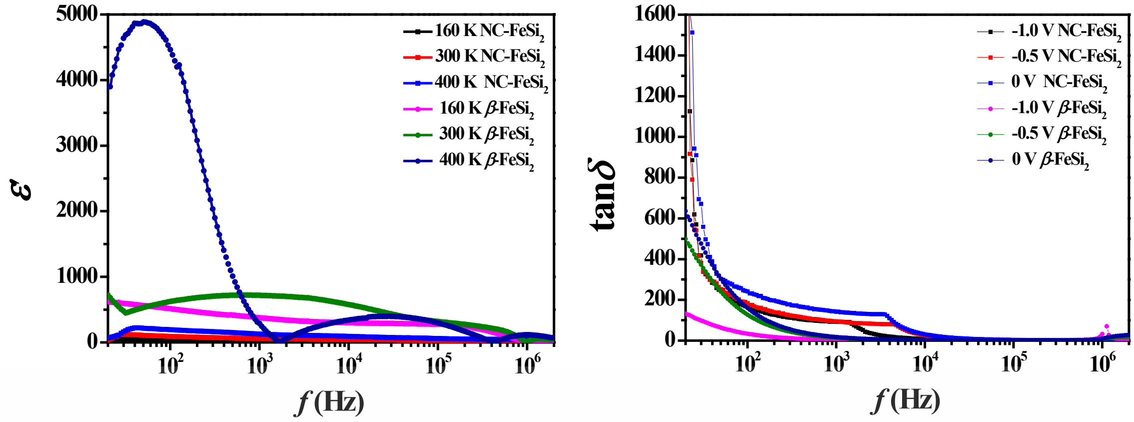

(a) (b)

Figure 4.14 The plot of (a) ε'-f and (b) tan δ-f at varying temperatures for the created *p*-Si/*n*-NC-FeSi$_2$ heterojunctions and *p*-Si/*n*-β-FeSi$_2$ heterojunctions.

4.2.3 Conductivities of n-FeSi$_2$/p-Si devices under temperature

Figure 4.15 shows the frequency dependence of σ_{AC} in the temperature from 160 K to 400 K, indicating that the conduction property is dominated by the localized charge movement, such as hopping mechanism [102]. The trend is supported by the consistent increase in σ_{AC} with frequency in the whole temperature region [102]. In the low f region, σ_{AC} is almost constant, which is consistent with σ_{DC} extrapolated from zero frequency in the σ_{AC}–f plot. This indicates that the electric field is not sufficient to cause hopping conduction [102]. Meanwhile, in the high f region, σ_{AC} shifts to the dispersion region, which can be attributed to the increased frequency that increases the possibility of charge carriers overcoming the local potential barrier [102].

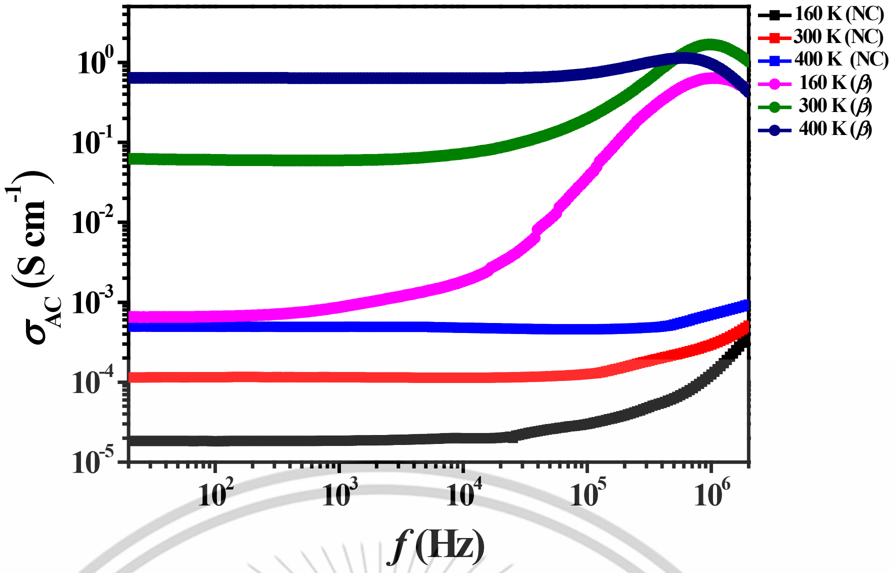

Figure 4.15 The σ_{AC}-f plot under varying temperature ranges for n-NC-FeSi$_2$/p-Si devices along side n-β-FeSi$_2$/p-Si devices.

The data in Figure 4.16(a) show that σ_{DC} of *p*-Si/*n*-NC-FeSi$_2$ heterojunctions increases sharply from 160 K to 180 K, and then gradually increases afterward. This behavior is consistent with the general characteristics of bulk-type heterojunctions, and supports the validity of the equivalent circuit model used in this study [90]. At temperatures between 160 and 180 K, the parameter *S* is less than 1, suggesting that the carriers undergo translational long-range hopping. On the other hand, in the range of 200 to 400 K, *S* exceeds 1, and localized short-range hopping becomes dominant. The increase in σ_{AC} with frequency also reflects the improved electric field response and the associated increased energy dissipation. At low temperatures, the lack of thermal energy and high resistivity limit carrier mobility, and mechanisms such as tunneling and capacitive conduction dominate. Below 180 K, these conduction processes also become less efficient leading to more difficult carrier transport [126]. From fitting parameters of *p*-Si/*n*-β-FeSi$_2$ heterojunctions at different temperatures in Figure 4.16(b) the *S* value is 1.01 at 200 K and 1.65 at 400 K. If *S* is less than or equal to 1, it means that the carriers made a long-distance jump, and if *S* is greater than 1, the transition is considered to be that of the local jump between adjacent stations is dominant. The increase of electrical conductivity observed with the increase of frequency is due to the decrease of R_s of materials due to the increase of eddy current loss and energy dissipation, making the bound charge move easier [127]. In addition, when the temperature is below 180 K, the transportation behavior changes to tunnel effect which is different from mechanic on higher T, which means that the tunnel effect at low temperature will be suppressed when temperature increase [126].

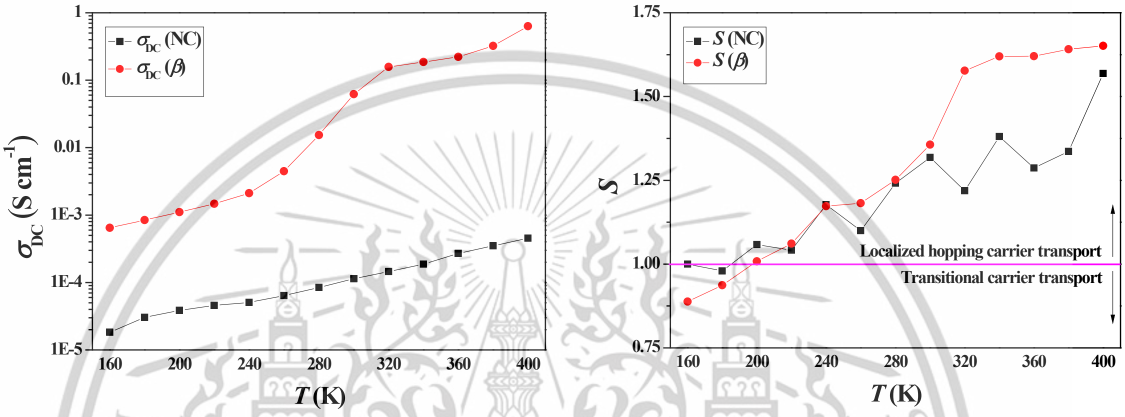

(a)

(b)

Figure 4.16 (a) The σ_{DC}-f plot and (b) the S plot under varying temperature ranges for n-NC-$FeSi_2$/p-Si devices along side n-β-$FeSi_2$/p-Si devices.

4.3 RTA treatment of Fe-Si based films

4.3.1 Physical properties of the β-$FeSi_2$ vs Fe_3Si films under different RTA temperatures

Figure 4.17(a) shows the XRD spectrum of the β-$FeSi_2$ thin film immediately after deposition on the Si(111) substrate, which confirms the peaks of Si(111) at about 28.4°, β(202/220) at about 29°, and β(404/440) at about 60°, which are consistent with the JCPDS card (No. 04-007-1080). After RTA treatment, the Si(111) peak disappears, which is believed to be due to overlap with the grown β(202/220) peak [128]. Annealing at 200-400°C improves the crystallinity of β-$FeSi_2$ and increases the peak intensity. Meanwhile, the peak intensity decreases at 600-800°C, which is believed to be the result of Fe and Si atoms being rearranged by thermal energy, promoting recrystallization [129-132]. Such structural changes are due to the higher mobility of Fe atoms compared to Si, which promotes diffusion within the film. EDS measurements showed that the Fe:Si ratio remained nearly 1:2 for all samples, and no significant interdiffusion between the film and the substrate was observed. Although β-$FeSi_2$ has an ordered compositional structure, significant interdiffusion is unlikely to occur, localized self-diffusion may have caused structural changes inside the film. Trace signals of C and Al were also detected, but these are likely due to organic contamination on the surface and trace impurities in the Si target. The XRD pattern of the as-deposited Fe_3Si film, shown in Figure 4.17(b), shows a prominent Fe_3Si(222) peak at 56.34° and a Si(111) peak at 28.46°. This is consistent with previous reports that Fe_3Si deposited by FTS at low temperatures forms a superposition state of the B2 structure [6]. When RTA is performed in the range of 200°C to 400°C, the peak intensities of Fe_3Si(222) and Si(111) increase, and new peaks such as β-$FeSi_2$ (021) at 25.70° and Fe_3Si(422) at 82.00° appear at 400°C [26,132]. Further heating to 600°C increases the intensity of the Si(111) and β(021) peaks, while Fe_3Si(222) and Fe_3Si(422) disappear, and instead, the Fe_3Si(220) peak appears at 45.34° [133,134]. In addition, peaks corresponding to FeSi(111) and FeSi(211) appear at 34.76° and 49.99°, indicating the progression of a phase transition [133,134]. At 800°C, the XRD pattern becomes dominated by the β-$FeSi_2$ phase, and in addition to Si(111), characteristic peaks of β(202)/(220) and β(404)/(440) also appear at 29.22° and 61.70°. These phase changes are considered to be thermal phase transitions caused by the large difference in the diffusion coefficients of Fe and Si (e.g., Fe⟶Si: approx. 3.5×10^{-6} cm^2/s, Si⟶Fe: approx. 1.5×10^{-8} cm^2/s at temperatures above 1000°C) [129-132]. High-temperature annealing promotes diffusion of Fe atoms and crystal reconstruction, and the structure and composition of the film transitions from Fe_3Si (200-400 °C) through FeSi (600 °C) and finally to β-$FeSi_2$ (800 °C) [129-132]. EDX analysis (Table 4.1) confirms this change, confirming that the Fe:Si ratio changes from Fe-rich to Si-rich. The phase transition adheres to phase diagram of Fe-Si based material as seen in Figure 4.18.

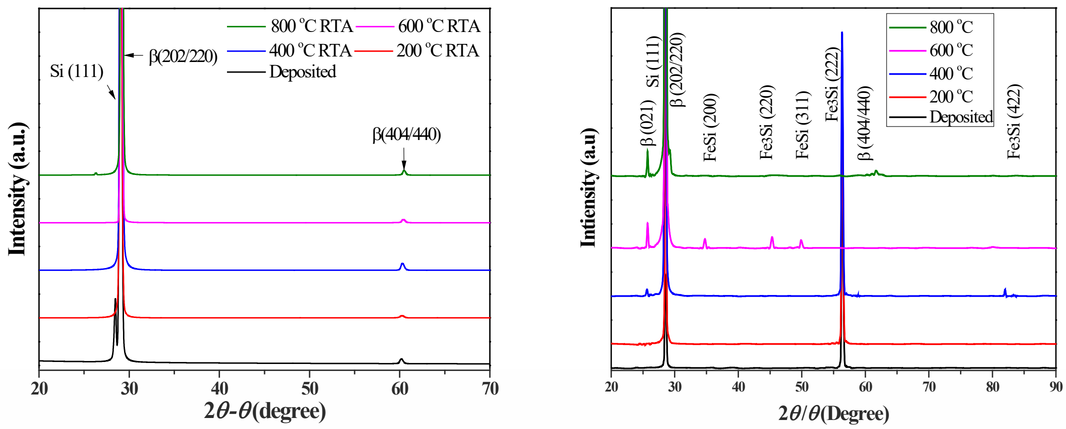

(a) (b)

Figure 4.17 XRD spectrum under 20-70° range of the (a) β-FeSi$_2$ and (b) Fe$_3$Si layers and rapidly annealed films by changing the T_{RTA} from 200 °C to 800 °C.

Table 4.1 Atomic compositions of β-FeSi$_2$ and Fe$_3$Si films at different T_{RTA} ranges

Condition	Composition of films (%)				Ratio of Fe:Si
	C	Al	Si	Fe	
β-FeSi$_2$	3.99	0.29	64.21	29.40	0.44
200 °C	5.63	0.41	66.83	27.13	0.41
400 °C	4.07	0.31	65.22	30.39	0.46
600 °C	5.59	0.39	65.53	28.49	0.43
800 °C	4.84	0.34	60.29	34.53	0.57
Fe$_3$Si	4.34	0.69	23.92	76.08	3.18
200	4.21	0.70	23.52	76.48	3.25
400	4.14	0.82	23.98	76.02	3.17
600	4.46	0.48	49.17	50.83	1.03
800	8.82	0.38	66.23	33.77	0.51

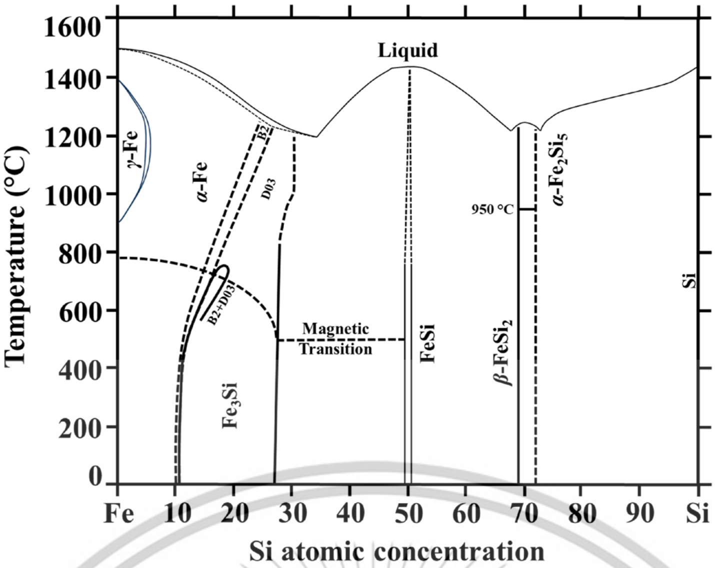

Figure 4.18 Phase diagram of Fe-Si based material at different Si atomic concentrations and temperatures.

Figure 4.19(a–e) shows the surface morphology of β-FeSi$_2$ films deposited on Si(111) substrates after as-deposited and RTA at 200–800 °C. The as-deposited films (Figure 4.19(a–e)) had a uniform grain distribution with an average grain size of about 29.16 nm estimated by XRD and Scherrer's equation function of Jade software. At 200 °C and 400 °C, the grain size grew to about 32.55 nm and 33.93 nm, respectively (Figure 4.19(b), (c)), confirming grain growth. Meanwhile, at 600 °C and 800 °C, the grain size decreased to about 30.17 nm and 28.01 nm, with simultaneous grain coarsening (Figure 4.19(d), (e)), suggesting the occurrence of recrystallization and/or structural dislocations. These changes reflect the change in atomic mobility with temperature, which leads to gradual grain growth at low temperatures, whereas at temperatures above 600 °C, the grains aggregate due to the sudden thermal stress, rearrange the structure, and relieve the internal stress. The AFM image ($2.5 \times 2.5\ \mu m^2$) shown in Figure 4.19(f) shows that the R_{rms} increased with increasing T_{RTA} from 3.83 nm as-deposited to 6.08 nm at 800 °C. The increase in roughness was gradual up to 400 °C, but progressed rapidly above 600 °C due to particle clustering, strain redistribution, deepening of grain boundaries, and crystallographic heterogeneity. Even though the grain size temporarily decreased, the surface roughness shows an overall tendency to increase due to the effects of particle aggregation and atomic diffusion at high temperatures. The surface morphology of Fe$_3$Si films, both as-deposited and post-RTA, was analyzed using FESEM and AFM. Figures 4.20(a)–(c) show that the as-deposited and 200–400 °C RTA films exhibit uniform nanocrystallites. The as-deposited film had an exceptionally smooth surface with an R_{rms} of ~1.339 nm, as shown in Figure 4.20(f), due to the benefits of FTDCS, which minimizes plasma bombardment via magnetic confinement [53]. At 200 °C and 400 °C, limited atomic diffusion led to only slight increases in R_{rms} values of 2.137 nm and 4.379 nm, respectively. At 600 °C, nanocrystallites merged into larger grains, roughening the surface significantly (R_{rms} = 21.190 nm, as seen in Figures 4.20(d). This trend intensified at 800 °C, with crystallites forming clustered colonies and R_{rms} reaching 51.320 nm. The trend is summarized in Figure 4.20(f).

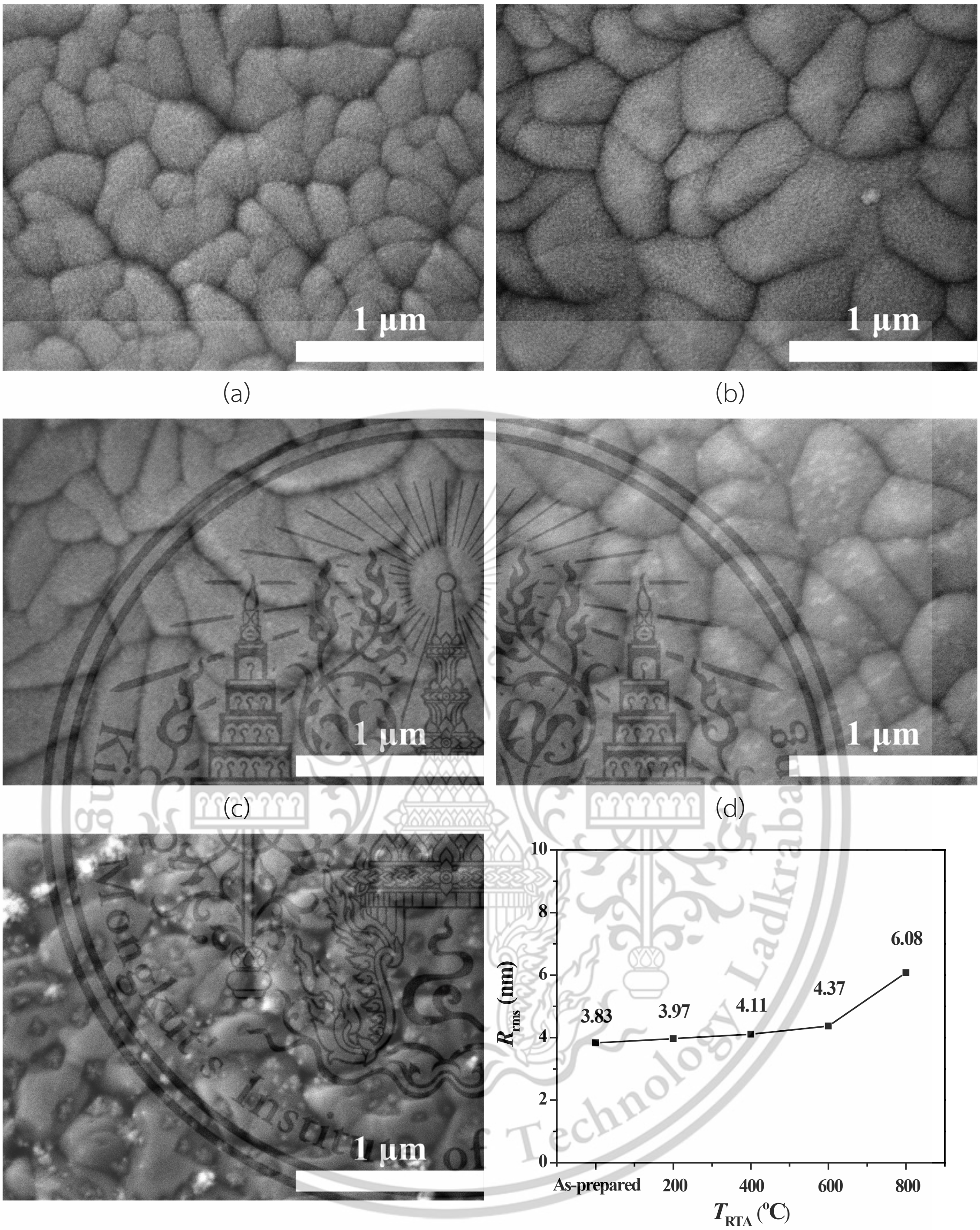

(a) (b)

(c) (d)

(e) (f)

Figure 4.19 The images from FESEM on (a-e) top view for β-$FeSi_2$ films as-prepared then after rapid annealing under a T_{RTA} ranging from 200 °C to 800 °C and (f) plot of AFM results.

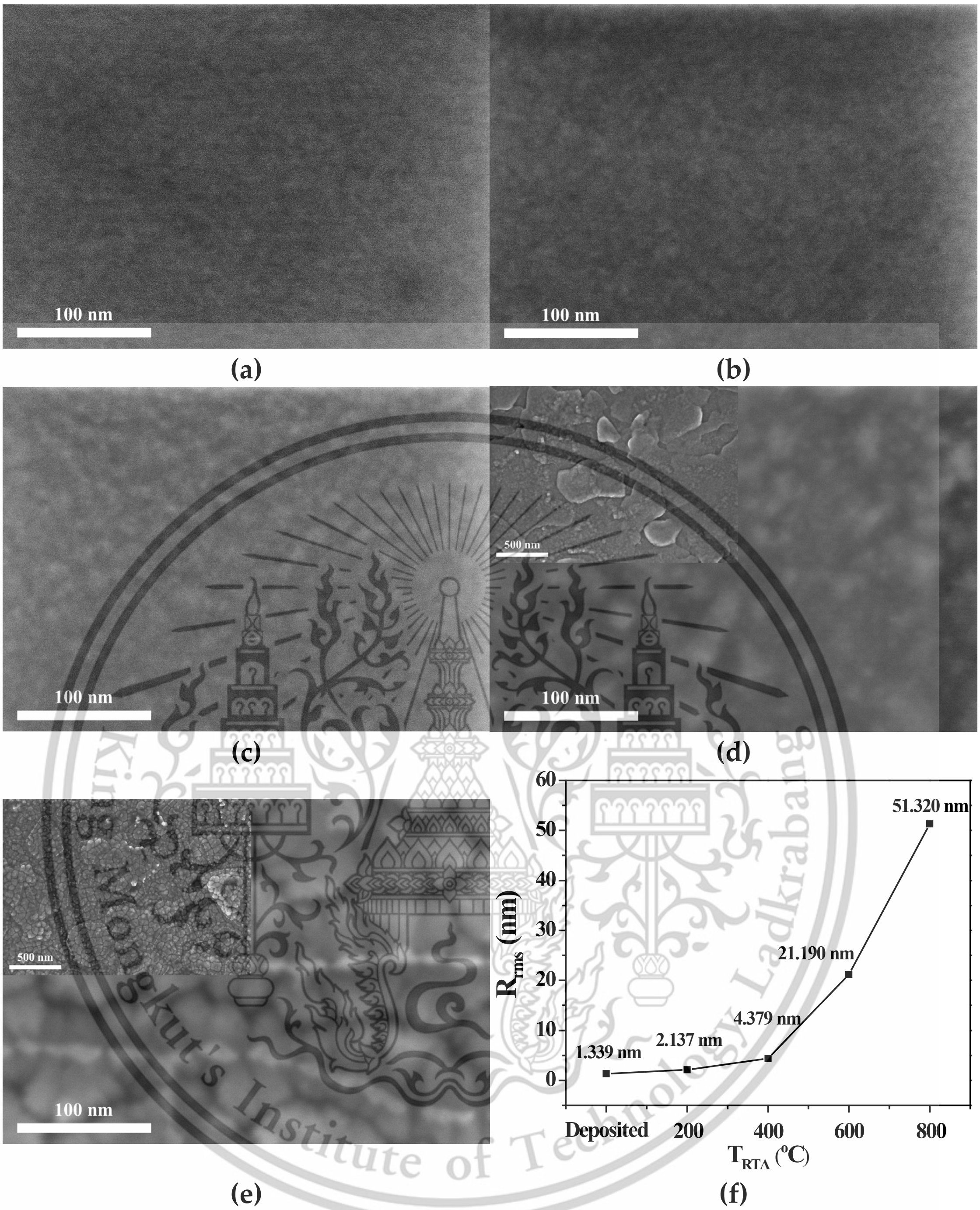

Figure 4.20 (a) Morphological image of the films on surface view before rapid annealing taken at 300 kx magnification taken from FESEM. Figure (b), (c), (d), and (e) are the images of the films after rapid annealing at 200 °C T_{RTA}, 400 °C T_{RTA}, 600 °C T_{RTA}, and 800 °C T_{RTA}, respectively. The insets in Figures (d) and (e) depict 50 kx FESEM images of Fe_3Si film's surfaces at 600 and 800 °C T_{RTA}, respectively. Figure (f) is plot of R_{rms} versus T_{RTA}.

In the cross-sectional images (Figure 4.21(i–j)), the film thickness increases slightly from about 512 nm as deposited to a maximum of about 548 nm after RTA at 200 °C–800 °C. This is likely due to the slight diffusion of Fe into the Si substrate, as it has a higher diffusion coefficient than Si. The film after low-temperature treatment maintained a smooth surface and a clear interface, whereas at 800 °C, the grains coarsened and the deep diffusion of Fe caused the surface to become rough and the interface to become unclear [129-132]. Cross-sectional FESEM images of Fe_3Si (Figures 4.21(a)–(e)) show that up to 400 °C, the films retained a smooth surface and clear interface. At 600 °C, structural uniformity degraded and a sub-layer emerged likely due to Fe diffusing into the Si substrate and triggering recrystallization. By 800 °C, this fusion layer dominated the film structure. This similar phenomenon was reported by M N Volochaev et al. [135] who annealed Fe_3SI and received similar trend of result as annealing temperature increased. They refer the cause to diffusion of films to substrate as TEM result revealed that diffusion layer firstly composed of FeSi then the result at higher temperature revealed mix phase including β-$FeSi_2$. Thicknesses measured via FESEM and surface profiler showed differing absolute values of 717.3 to 1704.2 nm (Figures 4.22(a)–(e)) but with similar trends. After subtracting the fused layers at 600 °C and 800 °C (818.6 nm and 553.5 nm, from ImageJ), the surface profile values better aligned with cross-sectional data. These comparisons are shown in Figure 4.22(f).

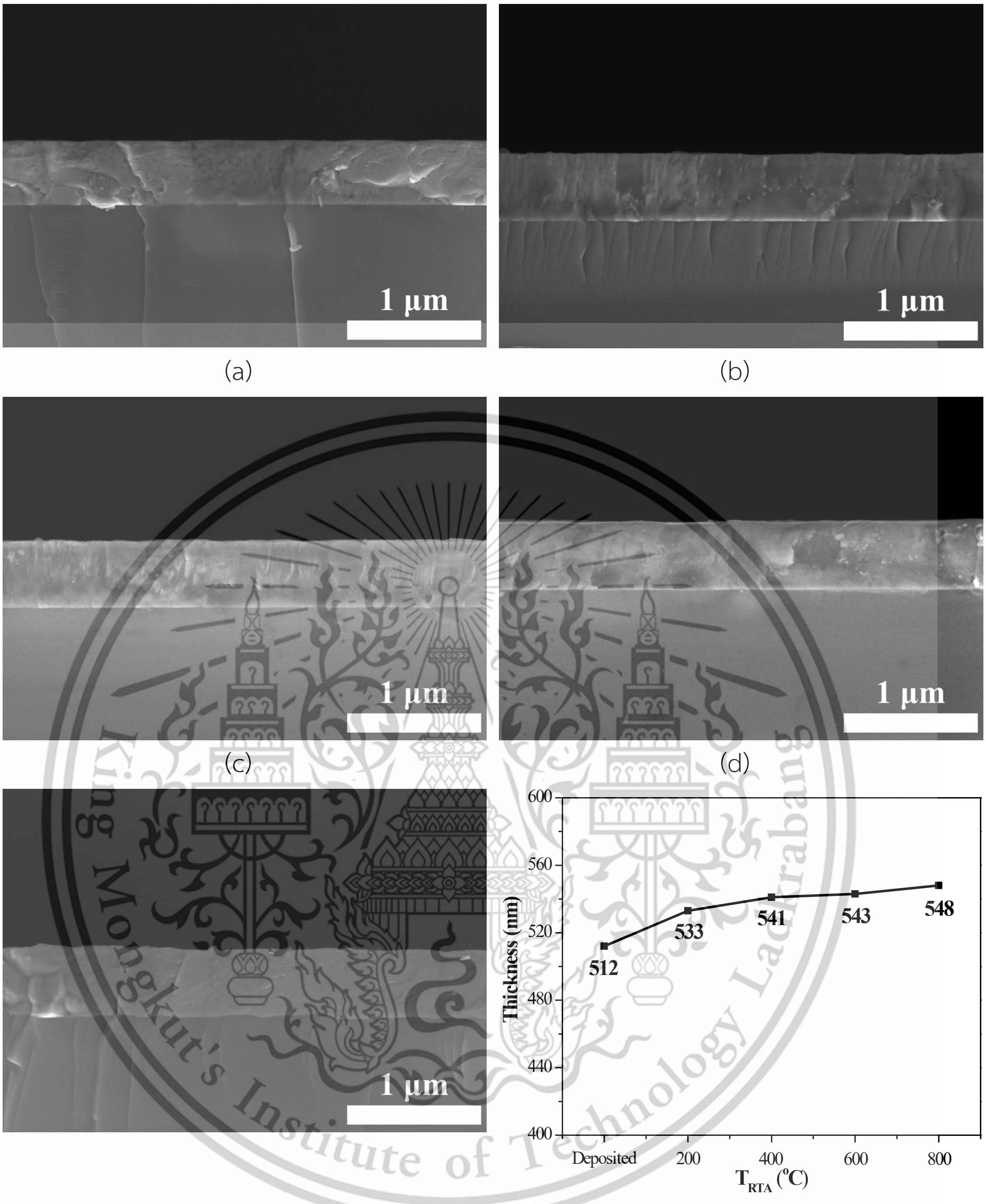

(a) (b)

(c) (d)

(e) (f)

Figure 4.21 The images from FESEM on (a-e) side view for β-$FeSi_2$ films as-prepared then after rapid annealing under a T_{RTA} ranging from 200 °C to 800 °C and (f) plot of thickness results.

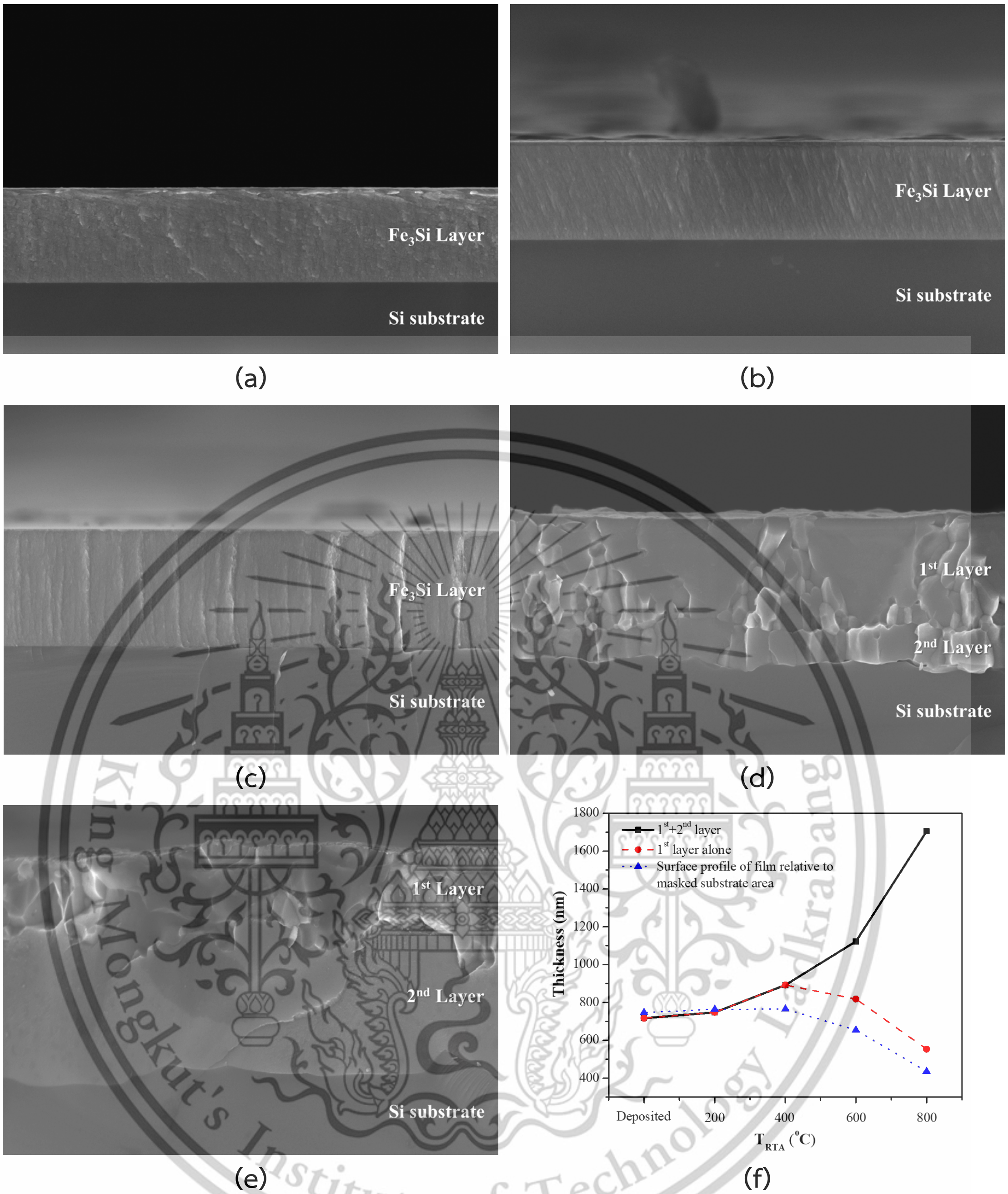

(a) (b)

(c) (d)

(e) (f)

Figure 4.22 (a-e) The side-viewed images of Fe$_3$Si films before rapid annealing and after rapid annealing at T_{RTA} of 200 °C, 400 °C, 600 °C, and 800 °C at 30kx. Figure (f) presents a comparison of film thicknesses of each film at different T_{RTA} ranges.

A comparison of the contact angle behavior of β-FeSi$_2$ and Fe$_3$Si thin films highlights the influence of the differences in surface structure and morphology on wettability. Both films exhibit hydrophobicity as deposited, with contact angles of

96.75° for β-$FeSi_2$ and 103.6° for Fe_3Si. Annealing at 200–400 °C gradually reduces the contact angles to 91.20° and 94.4°, respectively, due to grain growth and the reduction of microporosity on the surface. These pores trap air beneath the water droplet, which plays a role in maintaining hydrophobicity based on the Cassie-Baxter model [31,31]. Although the surface roughness increases, the hydrophobicity remains relatively stable under moderate temperature conditions. However, when the annealing temperature reaches 600–800 °C, both films turn hydrophilic. The contact angle of β-$FeSi_2$ drops significantly to 63.00°, and that of Fe_3Si also drops to 69.0°. This change is thought to result from a larger change in the surface structure. In β-$FeSi_2$, the particles gather to form clusters, and the fine voids that held the air disappear, changing the surface into one that is easier for water droplets to spread. [136] AFM measurements have also confirmed that above 600°C, the surface roughness increases while the water repellency of the surface tends to decrease. Similarly, in Fe_3Si, the nanocrystals fuse to form an uneven structure, and the air layer disappears. At this stage, the droplet comes into direct contact with the surface, and the wettability improves with the increase in surface roughness and actual contact area, which is consistent with the Wenzel model. Comparing the two, β-$FeSi_2$ shows more significant changes in the contact angle and surface behavior. In particular, the film treated at 800°C is located in the area classified as an "immersion film" in the Kao diagram, and it can be seen that it has higher wettability [137]. These properties make β-$FeSi_2$ highly promising for applications requiring this range of contact angle to interaction with fluids, such as microfluidic devices [138]. On the other hand, Fe_3Si transitions more gently to hydrophilicity and maintains a smooth surface even at low temperatures, making it suitable for applications requiring moderate surface adhesion and surface stability, such as interfaces for magnetic and electronic devices [6]. Overall, the change in contact angle strongly reflects the structural and morphological changes caused by heat treatment, and these findings provide an important guide for the design of surface functional materials with tailored wettability.

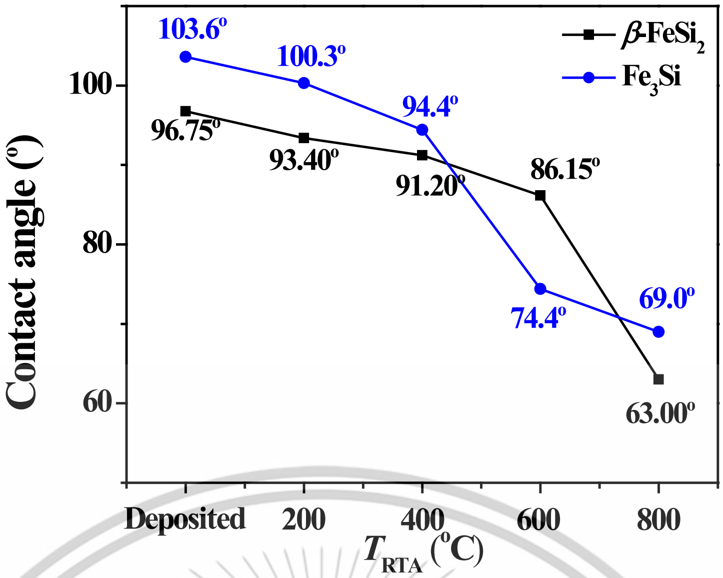

Figure 4.23 The θ_{CA} results using a deionized water testing solution for β-$FeSi_2$ and Fe_3Si layers as-created and after being rapidly annealed under different T_{RTA} ranges from 200 °C to 800 °C.

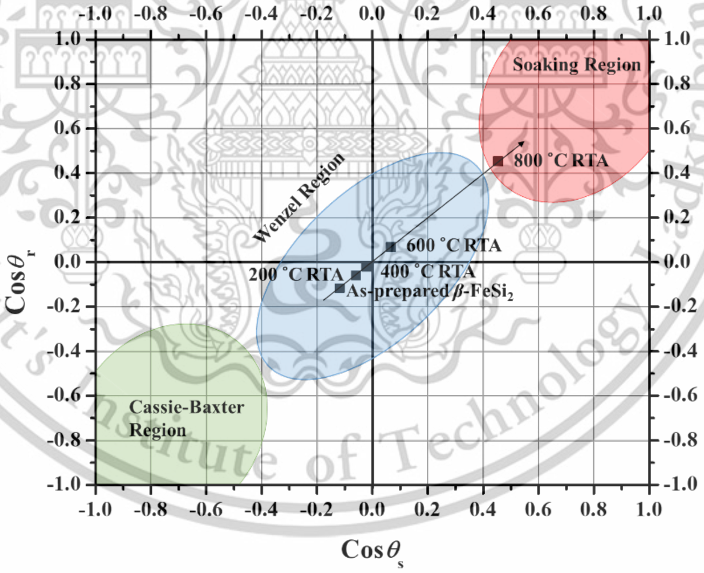

Figure 4.24 A Kao diagram of θ_{CA} values for β-$FeSi_2$ layers as-created and after being rapid thermal annealed under different T_{RTA} ranges from 200 °C to 800 °C in vacuum.

Comparing the mechanical properties of β-$FeSi_2$ and Fe_3Si thin films, it is clear that the structural and morphological changes significantly affect the hardness and elastic modulus of the respective films. For β-$FeSi_2$, the as-deposited hardness is 13.9 ± 0.64 GPa and the elastic modulus (Er) is 192.3 ± 9.45 GPa, and both values increase with increasing annealing temperature, reaching 15.2 ± 0.93 GPa and 225.8 ± 1.99 GPa after annealing at 800 °C. These values indicate mechanical strength comparable to or even superior to that of diamond-like carbon (DLC) films (hardness 12–30 GPa) [90], suggesting excellent wear resistance. Annealing at 200–400 °C is dominated by the inverse Hall-Petch effect, which promotes crystallinity and grain growth and reduces grain boundaries, resulting in increased deformation resistance [139]. On the other hand, at temperatures above 600 °C, dislocation activation by fine particles occurs, and further strengthening is promoted by the usual Hall-Petch effect [139]. Thus, the change in the dominant strengthening mechanism depending on the heat treatment is a major characteristic of the properties of β-$FeSi_2$. On the other hand, Fe_3Si has a slightly low hardness of 8.466 ± 0.016 GPa and Er of 189.3 ± 2.9 GPa immediately after deposition, but shows a rapid improvement above 600 °C, reaching a hardness of 19.129 ± 0.305 GPa and Er of 218.2 ± 9.7 GPa at 800 °C. In particular, the hardness at 800 °C exceeds that of β-$FeSi_2$, indicating that Fe_3Si also undergoes significant structural strengthening by high-temperature treatment [139]. This strengthening is thought to be mainly due to work hardening caused by structural phase transition and internal strain and is supported by the fact that larger stress is required during nanoindentation [139]. At intermediate temperatures (200–400 °C), the mechanical properties of Fe_3Si do not change significantly, but the surface remains relatively smooth and stable, and the deformation energy absorption is well balanced. Comparing the two in terms of applications, both have high hardness, elastic modulus, and good crystallinity with slightly to β-$FeSi_2$, making them resistant to wear and promising as a tool coating, highly durable protective film, and hard film material by epitaxial growth on steel substrates [26].

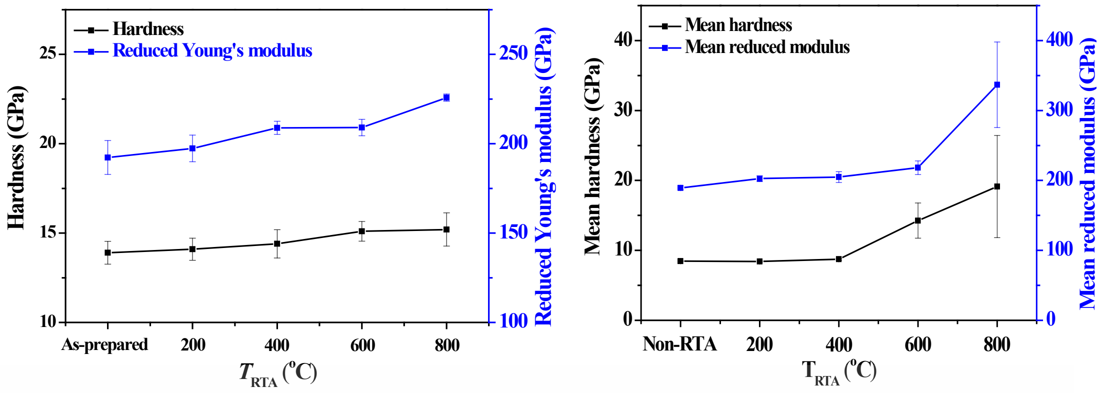

(e) (f)

Figure 4.25 (a-e) Mechanical properties presented in the form of an indentation load and penetrating depth plot of β-FeSi$_2$ and Fe$_3$Si layers as-prepared and after being rapidly annealed at different T_{RTA} of 200 °C to 800 °C. (f) Trend of hardness and reduced Young's modulus observed through different T_{RTA} values.

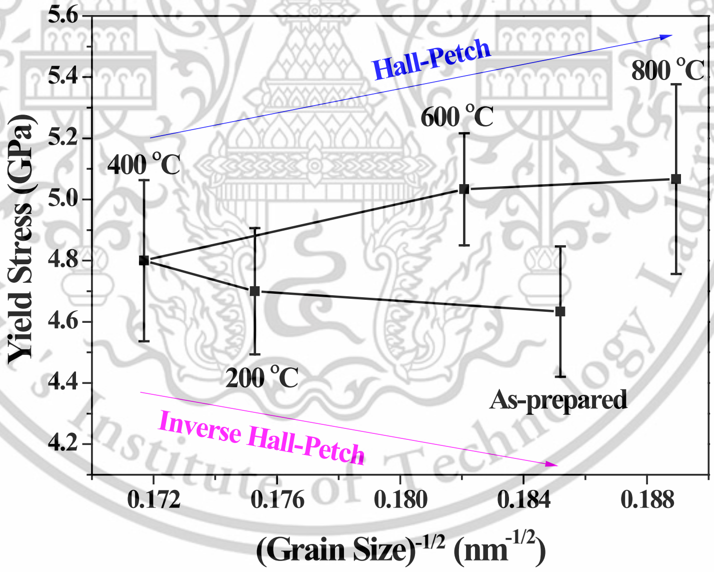

Figure 4.26 Yield stress vs grain size$^{-1/2}$ plot of β-FeSi$_2$ layers as-created and after being rapid thermal annealed under different T_{RTA} ranges from 200 °C to 800 °C in vacuum.

4.4 Plasma treatment of Fe-Si based films

4.4.1 Plasma's Analytical Discussion

A study on the optical emission spectrum of Ar gas plasma generated from the microwave frequency used in surface etching with a plasma power of 300 W at different etching times of 5, 10, and 15 minutes revealed spectral lines, These included excited Ar atoms at wavelengths 693.76, 704.61, 725.26, 736.28, 747.95, 761.15, 770.13, 792.44, 799.23, 809.35, 824.49, 849.49 and 909.62 nm, which also had oxygen atoms excited at wavelengths 775.00, 839.78, and 919.87 nm as well as atoms of hydrogen at a wavelength of 653.76 nm mixed in [140]. Figure 4.27 shows the spectral intensity ratio of Ar peak wavelengths at 761.15 and 809.35 nm from the National Institute of Standards and Technology's databank [140], selected to calculate T_e from two-emission-spectra ratio method [141]. The calculation revealed that the etching using Ar gas plasma produced by a microwave frequency of 300 W for 5 minutes had a T_e value of 0.287 eV, decreasing to 0.286 and 0.283 eV at 10- and 15-minute etching times, respectively. The n_e value using stark broadening was then calculated, revealing that the Ar gas plasma etching for 5, 10, and 15 minutes resulted in n_e values of 3.973×10^{17}, 3.977×10^{17}, and 4.027×10^{17} cm^{-1} indicating properties consistent with cold plasma at low vacuum [141]. The change in T_e but n_e increase over time was insignificant. This relative stability is due to the extremely high frequency of microwave which made energy distribution of plasma almost time independent [78,79].

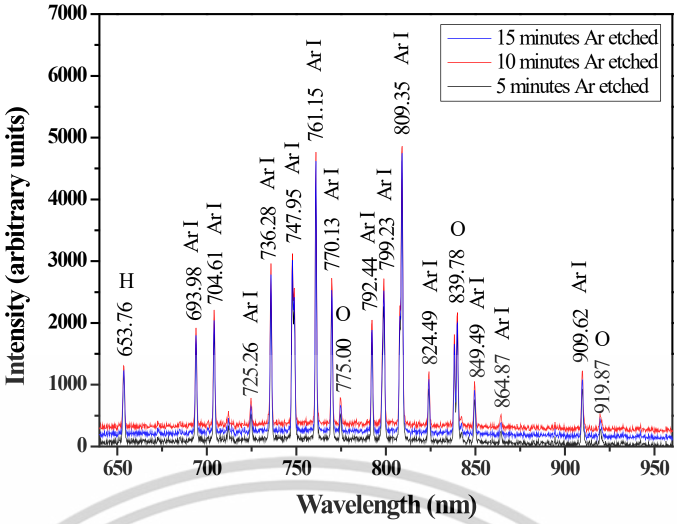

Figure 4.27 Optical emission spectra of microwave-based Ar plasma at 300 W under different durations of 5, 10, and 15 minutes.

4.4.2 Analytical Discussion of Chemical Composition

The spectra from the XPS measurement of unetched β-FeSi$_2$ thin films and films etched under different times are displayed in Figure 4.28. The XPS spectra identified peaks corresponding to Fe 2p and Si 2p as well as C 1s and O 1s, which were used to calculate the atomic concentrations in percentage terms using a proportion of the corrected peak area for a specific element for summation of the corrected peak area for all elements (corrected area = raw area/relative sensitivity factor) [142]. The calculated results of the β-FeSi$_2$ film surface can be observed in Table 4.2. The results indicate an inverse relationship between the percentage value of O 1s and C 1s in all β-FeSi$_2$ films. With an increase in the etching time, the percentage value of C 1s decreased while the percentage value of O 1s increased. The XPS analysis revealed that in addition to Fe and Si, the surface of all β-FeSi$_2$ thin films also contained a large amount of carbon and oxygen. These elements are common contaminants, especially in materials containing metals, as exposure to the environmental air promotes the formation of contamination [143,144]. The C 1s peak is caused by the spontaneous carbon layer which could also easily formed on materials exposed to the atmosphere [143]. These spontaneous carbon layers are often associated with hydrophobic properties. Under low-vacuum microwave plasma etching with high-energy Ar ions, these ions react with the sample surface, removing organic carbon contaminants by volatilizing them [141]. β-$FeSi_2$ is susceptible to oxidation, which facilitates the formation of the surface oxide layer [144]. The oxide groups, identified as the main factor in the hydrophilicity of the etched surface, also play an important role. Figure 4.32 shows the component peaks of the O 1s peak, representing the hydroxyl and oxide groups. The hydroxyl peak and oxide areas were relatively close when unetched [145]. The oxide peak reduced when first exposed to 5 minutes of etching, likely due to the selective etching of Si_xO_x [145], then slightly increased with a longer etching time. Meanwhile, the oxide and hydroxyl peak increased along with the etching duration but slightly decreased in the case of films etched for 15 minutes compared to those etched for 10 minutes due to cessation of oxide/hydroxyl formation from overexposure, causing the ion bombardment to also remove the dangling hydroxyl radical and oxide layer [145]. These additional hydrophilic oxide groups and hydroxyl radicals may originate from various source such as the trace amount of oxygen and air in the Ar gas and low-vacuum environment in the microwave plasma chamber, as well as the reactive groups remaining on the surface after plasma exposure [141]. The surface reacting with oxygen from the environment or impurities in the plasma led to the formation of an oxide group [141].

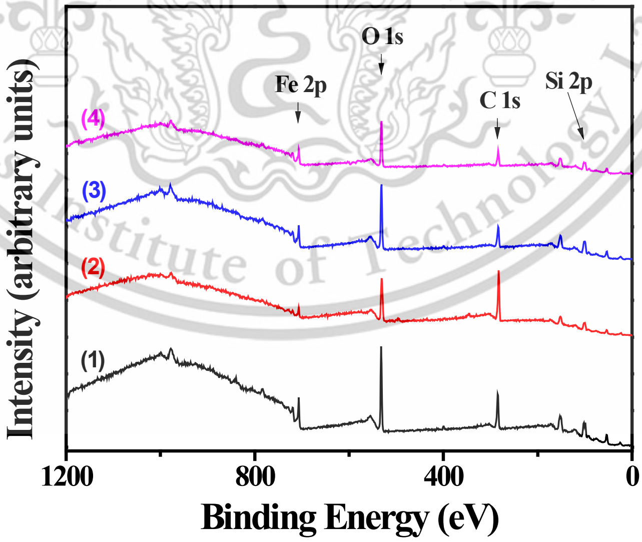

Figure 4.28 The XPS spectra of β-$FeSi_2$ films under various conditions: (1) as-coated β-$FeSi_2$ films, (2) after 5 minutes etching, (3) after 10 minutes etching, and (4) after 15 minutes etching.

Table 4.2 Results derived from the XPS spectra representing the surface chemical composition of β-FeSi$_2$ films under various conditions

Sample	at%			
	Fe	Si	C	O
Unetched	5.40	14.05	58.70	21.85
5 minutes	15.37	24.19	34.33	26.10
10 minutes	16.51	25.73	27.99	29.78
15 minutes	18.22	24.32	28.27	29.19

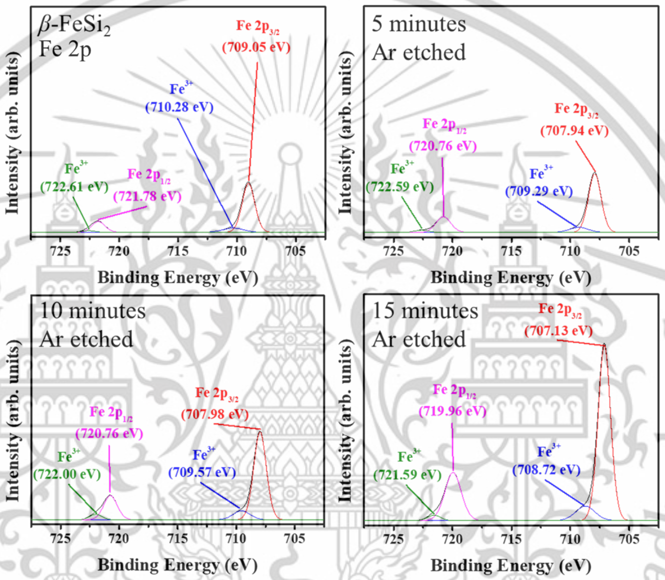

Figure 4.29 XPS spectra components of Fe 2p of the etched β-FeSi$_2$ thin films and the films after plasma etching at durations of 5, 10, and 15 minutes.

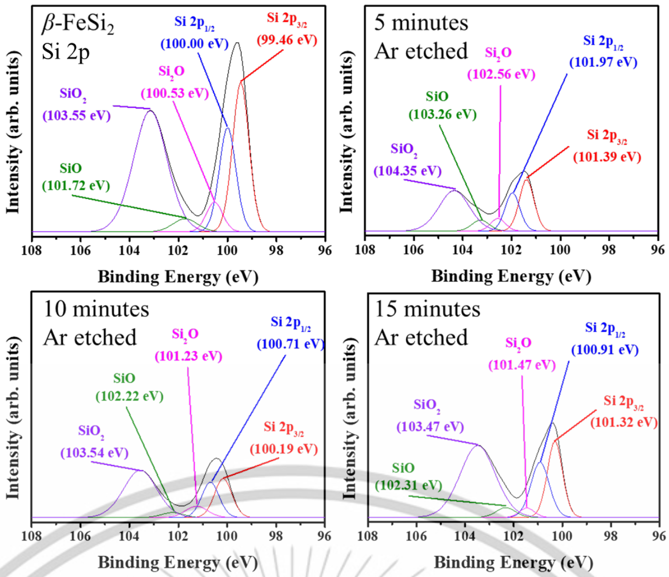

Figure 4.30 XPS spectra components of Si 2p of the etched β-FeSi$_2$ thin films and the films after plasma etching at durations of 5, 10, and 15 minutes.

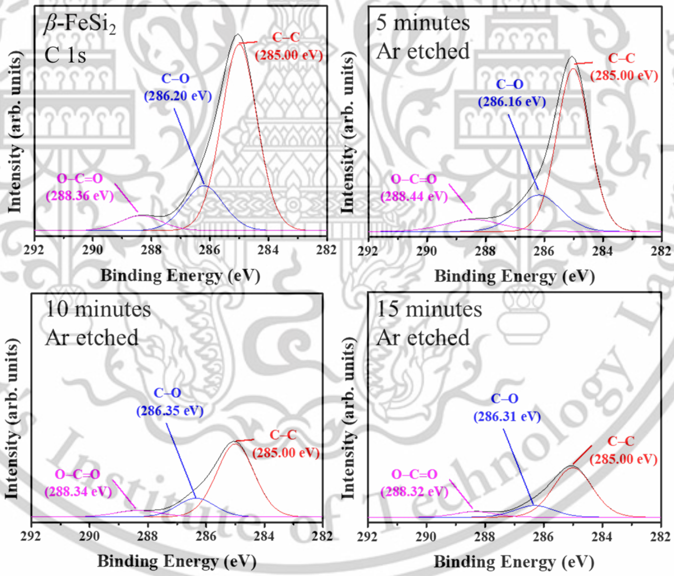

Figure 4.31 XPS spectra components of C 1s of the etched β-FeSi$_2$ thin films and the films after plasma etching at durations of 5, 10, and 15 minutes.

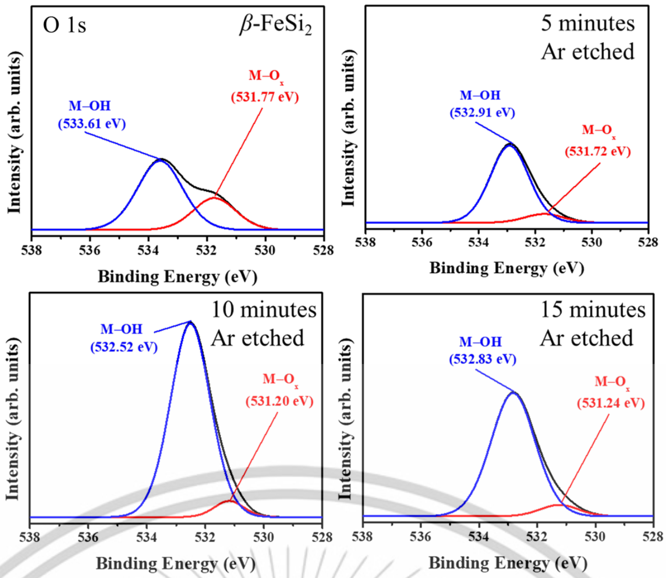

Figure 4.32 XPS spectra components of O 1s of the etched β-FeSi$_2$ thin films and the films after plasma etching at durations of 5, 10, and 15 minutes.

4.4.3 Analytical Discussion on the Structure

According to the XRD analysis of β-FeSi$_2$ thin films and those etched under the condition of the same power at 300 W, the etching time was different at 5, 10, and 15 minutes for deviations in the crystal structure when etching the surface with Ar gas plasma generated from the microwave measurement of a 2θ–θ scan from 20° to 70°. Figures 4.33(a) and 4.33(b) show that both XRD spectra demonstrate peaks of β(202/220) at about 29.1° and Si(111) at about 28.5°, including a small peak of β(404/440) at 60.3°, which are consistent with the characteristics of β-FeSi$_2$ reported in previous research [22]. The spectra after etching with Ar gas plasma at different durations do not exhibit any significant changes. Since the XRD measurement relies on detecting the diffraction of an X-ray beam from the sample, the presence of a defect layer could slightly deter the X-ray beam trajectory [146]. Therefore, the removal of the surface defect and contaminant through plasma etching grants the sample a slightly better alignment for the X-ray beam to propagate. In contrast, structure degradation caused by an overexposure of plasma may create more defects. Hence, the slight fluctuation may be due to the change of defect on the surface since the etching should rarely cause a shift in bulk structure, detected by the 2θ–θ mode [141].

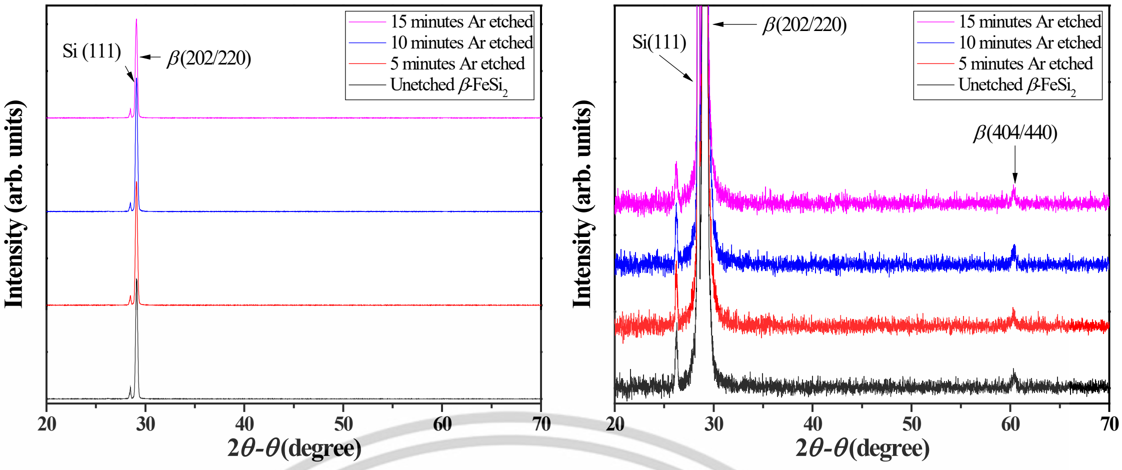

(a) (b)

Figure 4.33 XRD spectra in the as-coated β-FeSi$_2$ thin films and films after etching in durations of 5, 10, and 15 minutes: (a) full peak intensity and (b) a zoom-up view.

4.4.4 Analytical Discussion on Surface Morphology

The β-FeSi$_2$ thin films were examined before and after etching with Ar gas plasma generated by a microwave under the same power condition of 300 W and different etching durations of 5, 10, and 15 minutes, respectively, and the surface area and side-view cross-section of the thin film then analyzed. According to the surface area images of β-FeSi$_2$ thin film before and after etching, the morphology changed from the original cluster with a clear grain boundary, becoming almost amorphous. In addition, more holes appeared on the surface, and the hole size increased along with the etching duration. The cause is likely to be the plasma process in which Ar gas plasma particles or atoms are accelerated by the electric field into colliding with the particles on the surface of the samples, causing the bonds on the film surface to be broken and atoms volatilized [147]. The volatilized atoms come off, resulting in surface changes, as shown in Figure 4.34. Increased etching of the surface should originate from the increasing plasma saturation attributed to the OES, resulting in higher plasma temperature and broader energy distribution [148]. A longer etching duration also increases the likelihood of impact on the film area [149]. Hence, the morphology of the films becomes less defined with a longer duration despite the boundary becoming sharper five minutes after the selected etching of Ar plasma.

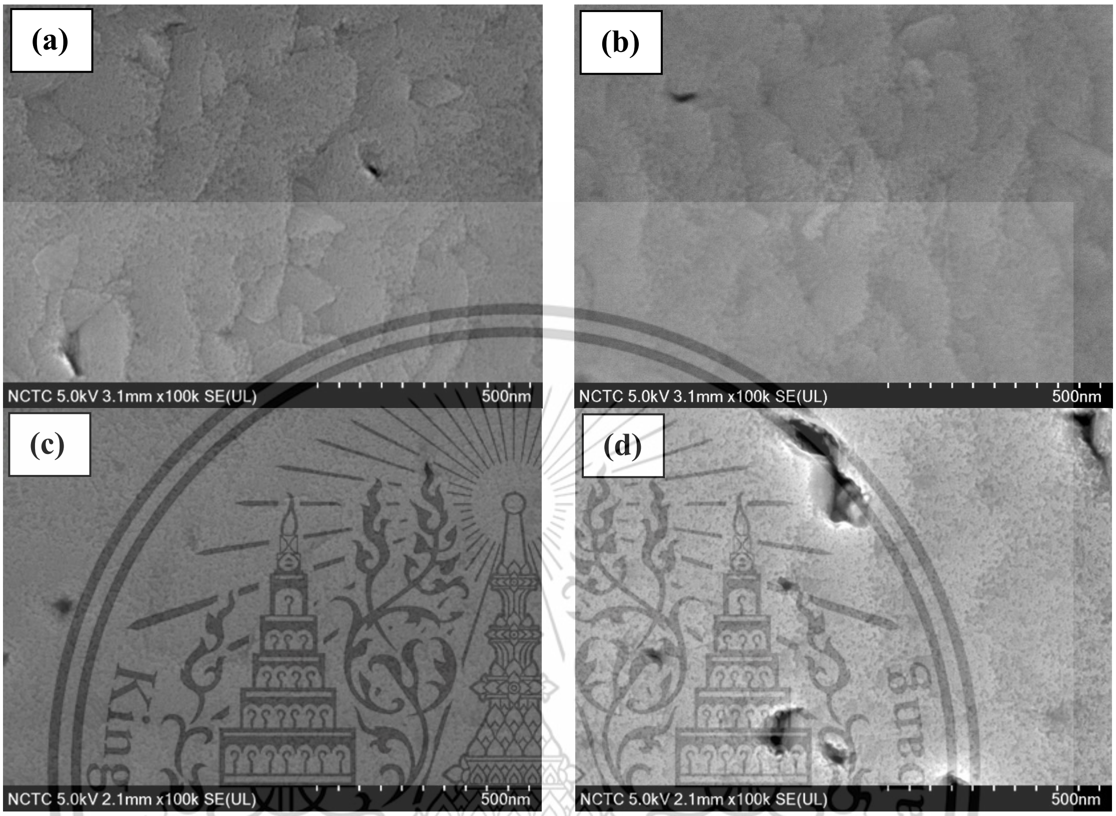

Figure 4.34 Surface-viewing FESEM micrographs for the surface of β-FeSi$_2$ films under various conditions: (a) as-coated β-FeSi$_2$ films, (b) after 5 minutes etching, (c) after 10 minutes etching, and (d) after 15 minutes etching.

When analyzing the cross-section of a sample unetched by plasma, the average thickness of the film was 563 nm. The β-FeSi$_2$ film's surface, etched at a power of 300 W for 5 minutes, caused the β-FeSi$_2$ films to become relatively thinner, with an average thickness of 553 nm. At the surface etching durations of 10 and 15 minutes, the average thickness of the β-FeSi$_2$ films decreased to 537 and 508 nm, respectively. The decrease in average film thickness, resulting from an increase in etching duration, is due to the interaction between the Ar plasma accelerated by the microwave electric field and the surface atoms of the film, causing atomic detachment on the surface of the film [141]. Therefore, as expected, the longer etching duration reduced the cross-section thickness of the etched β-FeSi$_2$ thin film, as shown in Figure 4.35 [149]. However, the thickness of β-FeSi$_2$ layers is less affected by plasma etching than the previously reported NC-FeSi$_2$ films [141] despite being etched in the plasma for a longer duration, likely due to stronger bond between film atoms.

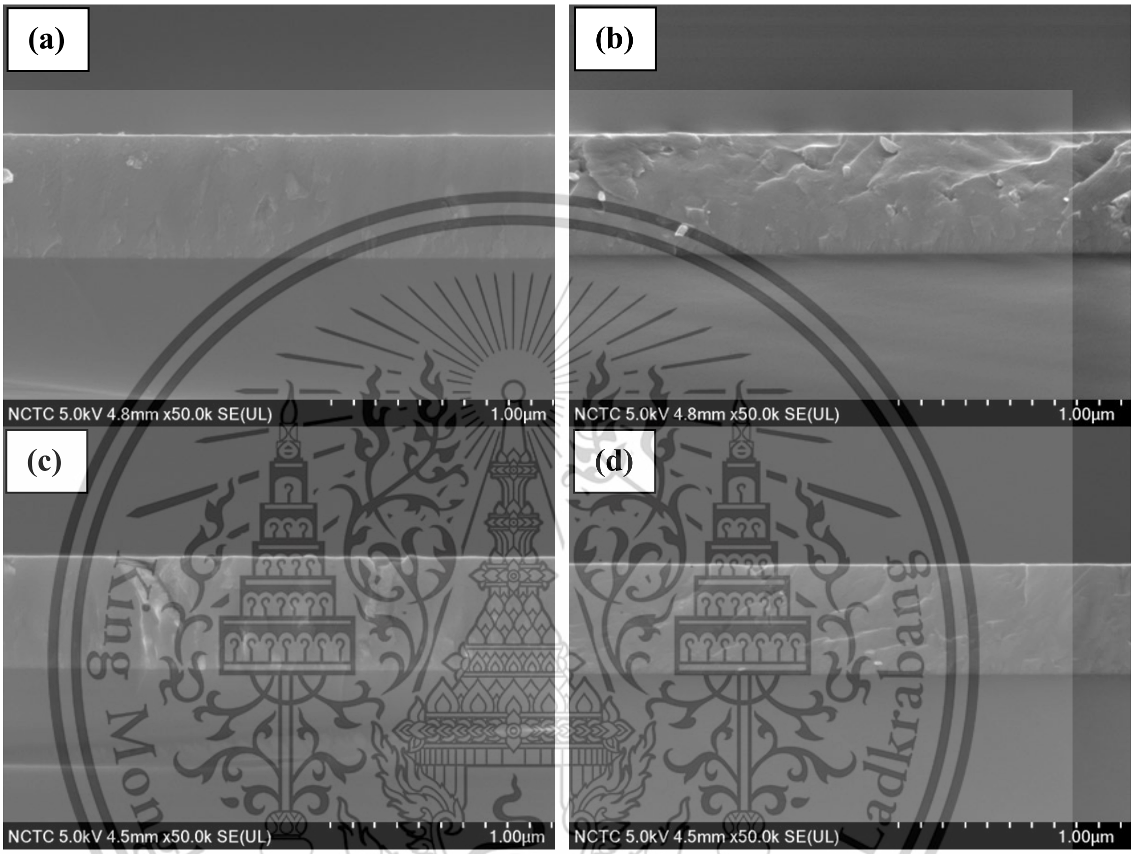

Figure 4.35 Cross-sectional FE-SEM photographs for the β-FeSi$_2$ thin films and Si substrate under various conditions: (a) as-coated β-FeSi$_2$ films, (b) after 5 minutes etching, (c) after 10 minutes etching, and (d) after 15 minutes etching.

The AFM analysis results for β-FeSi$_2$ thin films before and after microwave plasma etching with Ar gas plasma generated from a microwave at the same power and different etching durations were used to observe and compare the R_{RMS} values of the films changed in the form of $R_{RMS,}$ which could find the average deviation from the normal mean to be used as the accurate roughness value. The R_{RMS} surface image value of the β-FeSi$_2$ thin films before etching was 3.975 nm. When comparing the β-FeSi$_2$ thin films after etching with Ar gas plasma generated from a microwave at etching durations of 5, 10, and 15 minutes, under different durations were 4.117, 5.595, and 7.510 nm, respectively, indicating that the surface of the films slightly roughened with an increase in etching duration. This initially conflicted with the FE-SEM results but was expected due to the large holes appearing on the surface of the etched films. The interaction resulted from the volatilization of surface atoms, causing holes on the surface to become enlarged by longer exposure to plasma, as shown in Figure 4.36 [147]. These holes swayed to R_{RMS} values due to their drastic deviation, causing the overall value to increase.

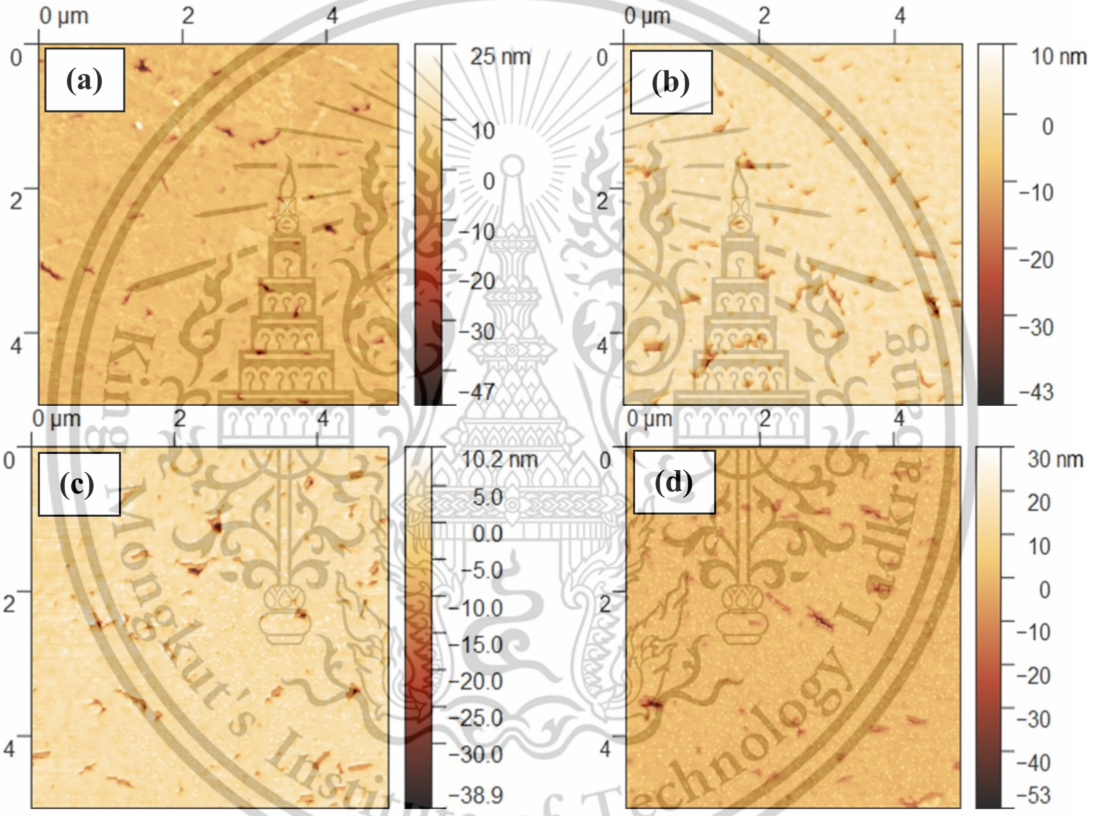

Figure 4.36 AFM images of the β-FeSi$_2$ thin films: (1) as-coated β-FeSi$_2$ films, (2) after 5 minutes etching, (3) after 10 minutes etching, and (4) after 15 minutes etching.

4.4.5 Analytical Discussion of Wettability

The results of the water contact angle measurement on β-FeSi$_2$ thin films before and after microwave plasma etching with Ar gas plasma generated from a microwave at the same power and different etching times showed that the sessile contact angle of DI water droplet on top of β-$FeSi_2$ thin film's surface prior to surface etching was 95.5°, indicating hydrophobicity. The water contact angle on the β-$FeSi_2$ surfaces after etching the surfaces at 300 W for 5, 10, and 15 minutes was measured. The contact angle was found to slightly decrease with longer etching duration, remaining at around 73.85°, 71.60°, and 70.75°, respectively, indicating hydrophilicity. As can be observed from Figure 4.37(b), the wetting properties of the surface changed after etching from hydrophobicity to hydrophilicity of the β-$FeSi_2$ thin film. The hydrophilicity properties remained the same as those shown in Figures 4.37(c) and 4.33(d). The wetting properties of the material can be explained physically by the Cassie-Baxter model, which uses the simple principle of air bubbles in gaps on the rough surface to support the water droplets in the explanation, alongside complex factor such as disjoining pressure and the liquid thin film at the interface that could support the shift in wetting state [150, 151]. Here, plasma etching results in the destruction of the air gap structure via surface changes, causing the surface to lose its hydrophobicity, and the contact angle decreases with a longer etching time resulting from the increased roughness [152]. The change in chemical composition on the XPS section might also shares responsibility for the change of the surface wetting state from hydrophobic to hydrophilic despite the shift in chemical composition is not as drastic as the previously reported NC-$FeSi_2$ study [141]. However, this range of contact angle is typical range for dental implant materials [153].

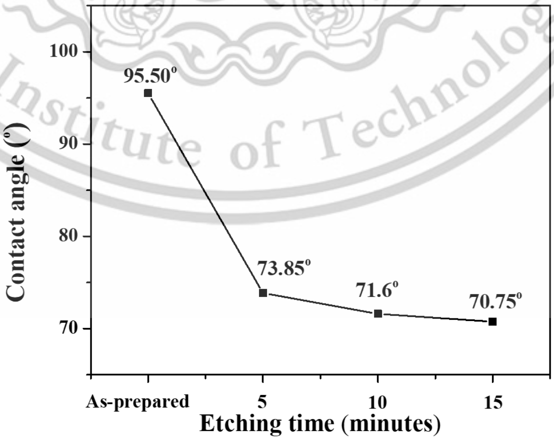

Figure 4.37 Contact angle values between DI water and β-$FeSi_2$ films as function of etching duration.

4.4.6 Solid Mechanic’s Analytical Discussion

Figure 4.38 presents the load-depth curve for each β-FeSi$_2$ thin film. The surface of the unetched β-FeSi$_2$ film exhibited H_{nano} of around 14.058 GPa, with an E_r of around 204.670 GPa. The results show that β-FeSi$_2$ samples possess noticeably higher H_{nano} and E_r than the Fe$_3$Si and NC-FeSi$_2$ from the previous work and are closer to those of commercial coating material such as DLC [90]. The etched β-FeSi$_2$ films at a duration of 5 minutes exhibited a H_{nano} value of 15.649 GPa and 220.110 GPa for the E_r value. With a longer etching duration of 10 minutes, the H_{nano} and E_r β-FeSi$_2$ films exhibited 15.851 GPa and 216.027 GPa, altering to 15.891 GPa and 219.062 GPa after 15 minutes of etching. The H_{nano} and E_r were almost the same, albeit slightly inclined, with a lower estimated standard deviation after Ar plasma etching. These results align with the inverse Hall-Petch principle which shows an inclining trend when the reduction of surface defects such as the oxide layer and grain boundary slide after the surface change (as can be observed in the morphology section) [139]. Following ion bombardment by Ar plasma, which increased saturation over time, the surface was damaged, resulting in less consistency on the surface structure and a rise in the standard deviation after increasing the etching duration [154].

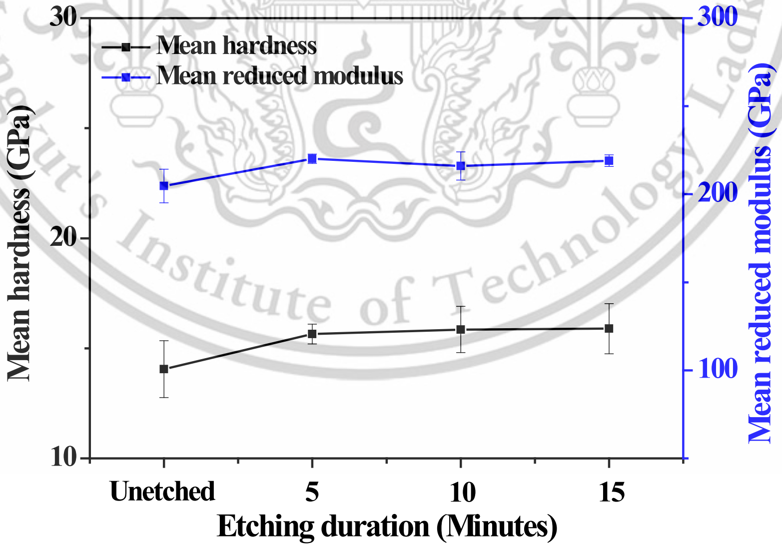

Figure 4.38 Hardness and reduced modulus for each β-FeSi$_2$ film in the case of (a) as-coated β-FeSi$_2$ films, (b) after 5 minutes of etching, (c) after 10 minutes of etching, and (d) after 15 minutes of etching.

Chapter 5

Conclusion and Suggestions

5.1 Conclusion

5.1.1 Effect of voltage on heterojunction devices of p-Si/n-FeSi$_2$

Al/n-NC-FeSi$_2$/p-Si/Pd heterostructures were fabricated by FTDCS at room temperature without post-annealing. *J*–*V* characteristics confirmed rectifying behavior with high leakage current due to accumulation of interface states. Impedance spectroscopy performed at frequencies ranging from 20 Hz to 2 MHz and varying reverse bias (–1 V to 0 V) revealed a single semicircular arc in the *Z”*–*Z’* plot, indicating that one relaxation process dominates. Weakening the reverse bias shortened τ and the radius of the arc, suggesting faster charge entry and exit. An equivalent circuit model reproduced this behavior, confirming that the CPE values of the components are in the range of nanocrystalline materials. Dielectric characterization also revealed a shoulder-like peak in tan δ around 10^3–10^4 Hz, with ε'' significantly larger than ε', revealing leakage dielectric behavior due to space charge polarization. The σ_{AC} increased with frequency, and the exponent *S* obtained by the Jonscher power law exceeded 1, suggesting that the local conduction mechanism in which carriers hop between neighboring sites is dominant. The σ_{DC} also increased significantly with decreasing reverse bias, suggesting improved carrier mobility. The electrical behavior of the n-β-FeSi$_2$/p-Si heterojunction was analyzed under varying bias voltage and temperature using AC impedance spectroscopy across a wide *f* range. Under different applied voltage (–1 V to 0 V), the impedance spectra exhibited single semicircular arcs, indicating a dominant relaxation process. With increasing *V*, reduced arc radius, lower R_s and R_p values, and higher CPE parameters pointed to enhanced carrier mobility and charge accumulation. The ε' and tan δ decreased with increasing frequency, with σ_{AC} displaying clear flat and dispersive regions. The extracted *S* values (1.23–1.61) confirmed a localized hopping mechanism. The σ_{DC} values rose with increasing bias, suggesting improved long-range charge transport and increased carrier injection, though some leakage remained under reverse bias. These result reveal mechanism of conduction as well as reveal dielectric properties of heterojunctions which would be basis for further studies to determine possible potential for storage application

5.1.2 Effect of temperature on heterojunction devices of p-Si/n-$FeSi_2$

Furthermore, temperature-dependent impedance measurements performed in the range of 160–400 K showed that the resistance components (R_s, R_g, R_{gb}, and R_j) increased with decreasing temperature, while the CPE components (CPE_g, CPE_{gb}, and CPE_j) decreased, indicating ideal capacitor-like behavior. The relaxation time τ increased from approximately 1.5×10^{-5} s at 400 K to approximately 7.1×10^{-5} s at 160 K, which is likely due to the decrease in thermally excited carriers. The dielectric constant ε' increased with temperature and showed stable values in the frequency range of 100 Hz–1 MHz. At 300 K and 1 MHz, the heterojunction shows $\varepsilon' = 24.5$ and low tan δ, comparable to PbO ($\varepsilon' \approx 25.9$) but without the associated toxicity. The S value is close to unity around 180 K and exceeds unity at higher temperatures, indicating that the carrier transport mechanism transitions from translational movement to local hopping. σ_{DC} decreases with decreasing temperature, confirming the thermally activated transport properties. These results confirm that the heterostructure exhibits sensitive and stable electrical response to bias and temperature. In particular, the high ε' value and tunable dielectric loss characteristics at high frequencies and temperature indicate the potential for applications in sensor components, dielectric filters, resonators, and even future energy storage devices. Temperature variation (160–400 K) also significantly affected electrical properties. As temperature increased, R_s and R_p decreased, while CPE and τ also shifted, indicating thermally activated conduction. Above 300 K, a pronounced change in ε' and tan δ behavior was observed, particularly with a growing donor-acceptor deionization peak in the low-frequency region. At 400 K, ε' reaches 4,464 at 100 Hz, which is roughly half the value of supercapacitor materials such as carbon black and graphene oxide. The S values transitioned from <1 at low temperatures, indicating of long-range transition, to >1 at higher temperatures, confirming a shift to localized carrier transport. The value of σ_{DC} increased with T due to enhancement of carrier excitation. In conclusion, both bias voltage and temperature significantly influence the conduction and dielectric behavior of the n-β-$FeSi_2$/p-Si heterostructure. These results highlight the potential for devices to be employed in high-temperature applications such as aerospace and downhole electronics. However, reduction of dielectric loss is necessary for practical usage.

5.1.3 RTA treatment of Fe-Si based films

Effect of RTA temperature on the structure, morphology, mechanical properties, and surface properties of Fe_3Si and β-$FeSi_2$ thin films prepared on Si(111) substrates by the FTDCS method were studied. In the Fe_3Si film, RTA at temperatures above 400 °C promotes a phase transition from Fe_3Si to FeSi and then to β-$FeSi_2$ at 800 °C. During this process, grain growth, surface roughening, and heterogeneity of the interface with the substrate progressed, and the hardness significantly increased from about 8.5 GPa to about 19.1 GPa. This indicates an improvement in mechanical strength due to grain boundary dislocations and recrystallization. The change in surface structure also changed the wettability of the film from hydrophobic to hydrophilic. On the other hand, in the β-$FeSi_2$ film, RTA at low temperatures (~400 °C) promoted grain growth, while high temperatures (above 600 °C) caused grain refinement and clustering. Concurrently, the crystallinity improved due to Fe diffusion, and the film thickness also increased slightly. The R_{rms} increased with increasing T, reflecting the change in the grain structure. Mechanically, both the hardness and elastic modulus improved, and the properties reached a level comparable to that of diamond-like carbon DLC films. Similarly, the wettability changed to hydrophilic above 600 °C due to the loss of the surface's air-retention function. These results suggest that RTA is an effective process for precisely controlling the properties of Fe-Si-based thin films, and indicates their potential for applications in protective hard coatings and even hydrophilic functional surface materials such as microfluidic for medical usage.

5.1.4 Plasma treatment of Fe-Si based films

In this study, the effects of microwave-generated Ar gas plasma etching on β-FeSi$_2$ thin films are examined through various aspects after being subjected to Ar plasma etching at different durations of 5, 10, and 15 minutes. The key findings include plasma diagnosis, chemical composition, structural analysis, surface morphology, wettability, and mechanical properties. The OES spectra of Ar plasma used for etching with 300 W power over 5–15 minutes showed excited Ar and oxygen atoms, where the T_e decreased from 0.287 eV to 0.283 eV with increased etching time, while n_e increased. These plasma parameters are consistent with cold plasma characteristics. The XPS analysis revealed changes in the surface composition of β-FeSi$_2$ films, with decreased C 1s and O 1s concentrations over a longer duration, implying the removal of surface contaminants and accumulation of hydrophilic oxide and hydroxyl by increasing the plasma etching duration. Meanwhile, the XRD patterns showed no significant changes for the β-FeSi$_2$ films etched in any duration. The FE-SEM and AFM analyses revealed a transition from defined grain boundaries to a less defined morphology with increasing R_{RMS} (from 3.975 nm as-created to 7.510 nm after 15 minutes of etching) due to larger holes and a reduction in film thickness (from 563 nm at as-created to 508 nm after 15 minutes of etching). Plasma etching reduced the contact angle from 95.5° (hydrophobic) to 70.8° (hydrophilic) after 15 minutes of etching due to a combination of the change in morphology leading to a collapse in the gap that supported the droplet and chemical composition changes on the surface. The values of H_{nano} and E_r remained relatively consistent, with slight deviations attributed to surface damage from prolonged etching, where H_{nano} increased from 14.058 GPa to 15.891 GPa while E_r increased from 204.670 GPa to 219.062 GPa. These results highlight the impact of plasma etching duration on the β-FeSi$_2$ film’s morphology, composition, and wettability of β-FeSi$_2$ films while preserving their mechanical integrity, allowing further development into coating materials for use in self-cleaning coating, friction-reducing coating for automotive parts, water vapor barrier coating for food packaging, and even dental implants.

5.2 Suggestions

1) The effect on RTA treatment on electrical properties on Fe-Si based heterojunction devices should be studied.

2) Effect of RTA duration should also be studied for modification of wetting properties and machinal properties of Fe-Si based materials

3) Effect of different gas flow rates and atmospheres during plasma etching should also be studied for wetting properties and machinal properties of Fe-Si based materials

4) Effect of aging should be included in study of wettability of Fe-Si based films.

Reference

[1] Izumi, S., Shaban, M., Promros, N., Nomoto, K., and Yoshitake, T. 2013. "Near-infrared photodetection of β-$FeSi_2$/Si heterojunction photodiodes at low temperature", Appl. Phys. Lett. 102 : 032107.

[2] Shaban, M., Izumi, S., Nomoto, K., and Yoshitake, T. 2009. "N-type β-$FeSi_2$/intrinsic-Si/p-type Si heterojunction photodiodes for near-infrared light detection at room temperature", Appl Phys Lett. 95 : 162102

[3] Yoshitake, T., Inokuchi, Y., Yuri, A., and Nagayama, K. 2006. "Direct epitaxial growth of semiconducting β-$FeSi_2$ thin films on Si (111) by facing targets direct-current sputtering", Appl. Phys. Lett. 88 : 182104.

[4] Sittisart, P., Promros, N., Chaleawpong, R., Charoenyuenyao, P., Borwornpornmetee, N., Tanaka, Y., and Yoshitake, T. 2020. "Light detection and carrier transportation mechanism in p-type Si/n-type nanocrystalline $FeSi_2$ heterojunctions produced via radio-frequency magnetron sputtering", J. Nanosci. Nanotechnol. 20 : 5082-5088.

[5] Funasaki, S., Promros, N., Iwasaki, R., Takahara, M., Shaban, M., and Yoshitake, T. 2013. "Fabrication of mesa structural n-type nanocrystalline-$FeSi_2$/p-type Si heterojunction photodiodes by liftoff technique combined with photolithography", Phys. Status Solidi C 10 : 1785-1788.

[6] Yoshitake, T., Nakagauchi, D., Ogawa, T., Itakura, M., Kuwano, N., Tomokiyo, Y., Kajiwara T., and Nagayama, K. 2004. "Room-Temperature Epitaxial Growth of Ferromagnetic Fe_3Si Films on Si(111) by Facing Target Direct-Current Sputtering.", Appl. Phys. Lett. 86 : 262505.

[7] Sadoh, T., Takeuchi, H., Ueda, K., Kenjo, A., and Miyao, M. 2006. "Epitaxial Growth of Ferromagnetic Silicide Fe_3Si on Si(111) Substrate.", Jpn. J. Appl. Phys. 45 : 3598.

[8] Schneeweiss, O., Pizurova, N., Jiraskova, Y., Žák, T., and Cornut, B. 2000. "Fe_3Si Surface Coating on SiFe Steel.", J. Magn. Magn. Mater. 215 : 115–117.

[9] Shaban, M., Nakashima, K., and Yoshitake, T. 2007. “Substrate Temperature Dependence of Photovoltaic Properties of β-$FeSi_2$/Si Heterojunctions Prepared by Facing-Target DC Sputtering”, Jpn. J. Appl. Phys. 46 : 7708.

[10] Chaleawpong, R., Promros, N., Charoenyuenyao, P., Nopparuchikun, A., Sittimart, P., Nogami, T., and Yoshitake, T. 2018. “Production of p-Type Si/n-Type β-$FeSi_2$ Heterojunctions Using Facing-Targets Direct-Current Sputtering and Evaluation of Their Resistance and Interface State Density”, Phys. Status Solidi A 215 : 1701022.

[11] Promros, N., Sittimart, P., and Kaenrai, W. 2016. “Investigation of electrical transport properties in heterojunctions comprised of silicon substrate and nanocrystalline iron disilicide films”, Int. J. Nanotechnol. 13 : 903-912.

[12] Ali, S., Chang, S., Imran, M., Shi, Q., Chen, Y. and Zhong, H. 2019. “Impedance spectroscopy: A versatile technique to understand solution-processed optoelectronic devices”, Phys. Status Solidi RRL 13 : 1800580.

[13] Xu, L., Lee, Y.-J., Hsua, J.W. P. 2014. “Charge collection in bulk heterojunction organic photovoltaic devices: An impedance spectroscopy study”, Appl. Phys. Lett. 105 : 123904.

[14] Panigrahi, J., Vandana, Singh, R., Batra, N., Gope, J., Sharma, M., Pathi, P., Srivastava, S.K., Rauthan, C.M.S., and Singh, P.K. 2016. “Impedance spectroscopy of crystalline silicon solar cell: Observation of negative capacitance”, Sol. Energy 136 : 412-420.

[15] Barreiro-Argüelles, D., Ramos-Ortiz, G., Maldonado, J.-L., Pérez-Gutiérrez, E., Romero-Borja, D., and Álvarez-Fernández, A. 2016. “PTB7:PC_{71}BM-based solar cells fabricated with the eutectic alloy field’s metal as an alternative cathode and the influence of an electron extraction layer”, IEEE J. Photovolt. 7 : 191-198.

[16] Qi, B., Zhang, Z.-G., and Wang, J., 2015. “Uncovering the role of cathode buffer layer in organic solar cells”, Sci. Rep. 5 : 7803.

[17] Wang, H., Wang, Y., He, B., Li, W., Sulaman, M., Xu, J., Yang, S., Tang, Y., and Zou, B. 2016. "Charge carrier conduction mechanism in PbS quantum dot solar cells: Electrochemical impedance spectroscopy study", ACS Appl. Mater. Interfaces 8 : 18526-18533.

[18] Demirezen, S. 2013. "Frequency-and voltage-dependent dielectric properties and electrical conductivity of Au/PVA (Bi-doped)/n-Si Schottky barrier diodes at room temperature", Appl. Phys. A 112 : 827-833.

[19] Yahia, I.S., Fadel, M., Sakr, G.B., Shenouda, S.S., Yakuphanoglu, F., and Farooq, W.A. 2011. "Impedance Spectroscopy of Nanostructure p-$ZnGa_2Se_4$/n-Si Heterojunction Diode", Acta Phys. Pol. A. 120 : 563–366.

[20] Kumar, M., Shankar, S., Brijmohan, Kumar, S., Thakur, O.P., and Ghosh, A.K. 2017. "Impedance spectroscopy and conductivity analysis of multiferroic BFO–BT solid solutions", Phys Lett A. 381 : 379–386.

[21] Thakur, S., Rai, R., Bdikin, I., and Valente, M.A. 2016. "Impedance and modulus spectroscopy characterization of Tb modified $Bi_{0.8}A_{0.1}Pb_{0.1}Fe_{0.9}Ti_{0.1}O_3$ ceramics", Materials Research. 19 : 1–8.

[22] Charoenyuenyao, P., Chaleawpong, R., Borwornpornmetee, N., Paosawatyanyong, B., Sittimart, P., Yoshitake, T., and Promros, N. 2022. "Investigation of morphological surface features, wetting behavior and mechanical traits under various substrate temperatures for beta iron disilicide prepared via facing-targets sputtering", Mater. Sci. Semicond. Process. 146 : 106604.

[23] Borwornpornmetee, N., Charoenyuenyao, P., Chaleawpong, R., Paosawatyanyong, B., Phatthanakun, R., Sittimart, P., Aramaki, K., Hamasaki, T., Yoshitake, T., and Promros, N. 2021. "Physical properties of Fe_3Si films coated through facing targets sputtering after microwave plasma treatment", Coatings 11 : 923.

[24] Borwornpornmetee, N., Sittimart, P., Phatthanakun, R., Nakajima, H., Paosawatyanyong, B., Yoshitake, T., and Promros, N. 2023. “Physical feature exploration of nanocrystalline $FeSi_2$ surface with argon plasma etching under varying power”, Vacuum 218 : 112588.

[25] Murakami, T., Hibi, Y., Mano, H., Matsuzaki, K., Inui, H. 2012. “Friction and wear properties of Fe–Si intermetallic compounds in ethyl alcohol”, Intermetallics 20 : 68-75.

[26] Chang-bin, T., Hong-xia, C., Fu-rong, W., Ni-jun, X., Wei, H., Juan-qin, X. 2020. “Facile preparation and tribological property of alloyed Fe_3Si coatings on stainless steels surface by molten-salt infiltration method”, Surf. Coat. Technol. 397 : 126049.

[27] Nakamura, S., Aoki, T., Kittaka, T., Hakamata, R., Tabuchi, H., Kunitsugu, S., and Takarabe, K.I. 2007. “Facing target sputtered iron-silicide thin film.”, Thin Solid Films 515 : 8205-8209.

[28] Chen, Y.T. and Zou, Y.J. 2017. “Effect of (102) Diffracted Peak on Magnetic, Photoelectric, and Adhesive Characteristics of Fe_2Si Films”, J. Nanosci. Nanotechnol. 17 : 1198-1203.

[29] Nunes, B., Magalhães, S., Franco, N., Alves, E., Serro, A.P. and Colaço, R., 2013. “Wettability and nanotribological response of silicon surfaces functionalized by ion implantation”, In Materials Science Forum 730 : 257-262.

[30] Charoenyuenyao, P., Promros, N., Chaleawpong, R., Saekow, B., Porntheeraphat, S., and Yoshitake, T. “Influence of annealing temperature on mechanical and wetting properties of β-$FeSi_2$ films built using facing-targets direct-current sputtering”, J. Nanosci. Nanotechnol. 20 : 621-628.

[31] Schrader, M.E. and Loeb, G.I. 2013. Modern approaches to wettability: theory and applications. Maryland, Springer Science & Business Media.

[32] Mohamed, A.M., Abdullah, A.M., and Younan, N.A. 2015. “Corrosion behavior of superhydrophobic surfaces: A review.” Arab. J. Chem. 8: 749-765.

[33] Charoenyuenyao, P., Promros, N., Chaleawpong, R., Saekow, B., Porntheeraphat, S., and Yoshitake, T. 2019. “Effect of annealing on surface morphology and wettability of NC-$FeSi_2$ films produced via facing-target direct-current sputtering”, J. Nanosci. Nanotechnol. 19 : 6834-6840.

[34] Bazhan, Z., Ghodsi, F.E., and Mazloom, J. 2018. “Effect of phase transition induced by annealing temperature on wettability, optical and photocatalytic properties of nanostructured iron oxide thin film”, J Mater Sci: Mater Electron. 29 : 11489–11497.

[35] Du, P., Wang, X., Lin, I.K., and Zhang, X. 2012. “Effects of composition and thermal annealing on the mechanical properties of silicon oxycarbide films”, Sens. Actuators A Phys. 176 : 90–98.

[36] Ghosh, S.P., Das, K.C., Tripathy, N., Bose, G., Kim, D.H., Lee, T.I., Myoung, J.M., and Kar, J.P. “Microstructural evolution of sputtered ZnO thin films with rapid thermal annealing”, J Mater Sci: Mater Electron. 26 : 7860–7866.

[37] Lin, X.W., Behar, M., Desimoni, J., Bernas, H., Swider, W., Liliental-Weber, Z., Washburn, J. 1992. “Epitaxial Phase Formation of $FeSi_2$ in an Fe-Implanted Si by Ion Irradiation and Rapid Thermal Annealing”, Mater Res Soc Symp Proc. 279 : 535–540.

[38] Wu, P-H., Lin, I-K., Yan, H-Y., Ou, K-S., Chen, K-S., Zhang, X. 2011. “Mechanical property characterization of sputtered and plasma enhanced chemical deposition (PECVD) silicon nitride films after rapid thermal annealing”, Sens. Actuators A: Phys. 168 : 117-126.

[39] Chiu, Y.J., Shen, C.Y., Chang, H.W. and Jian, S.R., 2018. “Characteristics of Iron-Palladium alloy thin films deposited by magnetron sputtering”, Results in Physics 9 : 17-22.

[40] Ting, J.A. S., Rosario, L.M. D., Lee Jr, H. V., Ramos, H. J., Tumlos, R. B., and Fischer, R. V. 2014. “Studies on the use of the coaxial plasma bulb for enhanced wettability of aluminum and polymethylmethacrylate surfaces”, Vacuum 103 : 9-13.

[41] Ru, L. and Jie-Rong, C. 2006. "Studies on wettability of medical poly (vinyl chloride) by remote argon plasma", Appl. Surf. Sci. 252 : 5076-5082.

[42] Zajíčková, L., Subedi, D. P., Buršíková, V., Veltruská, K. 2003. "Study of argon plasma treatment of polycarbonate substrate and its effect on film deposition", Acta Phys. Slov. 53 : 489-504.

[43] Borisenko, V.E. 2013. Semiconducting Silicides: Basics, Formation, Properties. Berlin : Springer Science & Business Media.

[44] Chen, L.J. 2004. Silicide Technology for Intregrated Circuits, The institution of London : Engineering and Technology.

[45] Christensen, N.E. 1990. "Electronic structure of β-FeSi$_2$.", Phys. Rev. B. 42 : 7148-7153.

[46] Bost, M.C. and Mahan, J.E. 1985. "Optical properties of semiconducting iron disilicide thin films.", J. Appl. Phys. 58 : 2696-2703.

[47] Suzuno, M. Murase, S. Koizumi, T. and Suemasu, T. 2008. "Improved Room-Temperature 1.6 μm Electroluminescence from p-Si/β-FeSi$_2$/n-Si Double Heterostructures Light-Emitting Diodes.", Appl. Phys. Express. 1 : 021403.

[48] Suzuno, M. Koizumi, T. and Suemasu, T. 2009. "p-Si/ β-FeSi$_2$/n-Si double-heterostructure light-emitting diodes achieving 1.6 μm electroluminescence of 0.4 mW at room temperature.", Appl. Phys. Lett. 94 : 213509.

[49] Gay, J.M. Stocker, P. and Rethore, F. 1993. "X-ray scattering studies of FeSi$_2$ films epitaxially grown on Si (111).", J. Appl. Phys. 73 : 8169-8178.

[50] Mahan, J.E. Thanh, V.L. Chevrier, J. Berbezier, I. Derrien, J. and Long, R.G. 1993. "Surface electron-diffraction patterns of β-FeSi$_2$ films epitaxially grown on silicon.", J. Appl. Phys. 74 : 1747-1761.

[51] Yoshitake, T., Yatabe, M., Itakura, M., Kuwano, N., Tomokiyo, Y., and Nagayama, K. 2003. "Semiconducting nanocrystalline iron disilicide thin films prepared by pulsed-laser ablation.", Appl. Phys. Lett. 83 : 3057-3059.

[52] Milosavljević, M., Wong, L., Lourenço, M., Valizadeh, R., Colligon, J. Sha, G., and Homewood, K.P. 2010. "Correlation of structural and optical properties of sputtered FeSi2 thin films.", Jpn. J Appl. Phys. 49 : 081401.

[53] Shaban, M., Kondo, H., Nakashima, K., and Yoshitake, T. 2008. “Electrical and photovoltaic properties of n-type nanocrystalline-$FeSi_2$/p-type Si heterojunctions prepared by facing-targets direct-current sputtering at room temperature.”, Jpn. J. Appl. Phys. 47 : 5420-5422.

[54] Takarabe, K., Doi, H., Mori, Y., Fukui, K., Shim, Y., Yamamoto, N., Yoshitake, T., and Nagayama, K. 2006. “Optical properties of nanocrystalline $FeSi_2$ and the effects of hydrogenation.”, Appl. Phys. Lett. 88 : 061911.

[55] Shaban, M., Kawai, K., Promros, N., and Yoshitake, T., 2010. “n-Type nanocrystalline-$FeSi_2$/p-Type Si heterojunction photodiodes prepared at room temperature.”, IEEE Electron Device Lett. 31 : 1428-1430.

[56] Starke, U., Schardt, J., Weiss, W., Meier, W., Polop, C., De Andres, P. L., and Heinz, K. 2001. “Structural and compositional reversible phase transitions on low-index Fe3Si surfaces.”, EPL 56 : 822.

[57] Zhang, Y., and Ivey, D. G. 1998. “Fe_3Si formation in Fe–Si diffusion couples.”, J. Mater. Sci. 33 : 3131-3135.

[58] Hamaya, K., Ueda, K., Kishi, Y., Ando, Y., Sadoh, T., and Miyao, M. 2008. “Epitaxial ferromagnetic Fe_3Si/Si (111) structures with high-quality heterointerfaces”, Appl. Phys. Lett. 93 : 132117.

[59] Herfort, J., Schönherr, H. P., and Ploog, K. H. 2003. “Epitaxial growth of Fe_3Si/GaAs (001) hybrid structures.”, Appl. Phys. Lett. 83 : 3912-3914.

[60] Yakovlev, I. A., Varnakov, S. N., Belyaev, B. A. E., Zharkov, S. M., Molokeev, M. S., Tarasov, I. A. E., and Ovchinnikov, S. G. E. 2014. “Study of the structural and magnetic characteristics of epitaxial Fe_3Si/Si (111) films”, JETP letters. 99 : 527-530.

[61] Wasa, K., and Hayakawa, S. 1992. Handbook of Sputter Deposition Technology: Principles, Technology, and Applications. New Jersey : Noyes Publication.

[62] Kadokura, S. Facing-targets-type sputtering apparatus and method. U.S. patent no. 6911123B2. June 2005.

[63] Kadokura, S. Facing Target Type Sputtering Apparatus. U.S. patent no. 6156172. December 2000.

[64] Yoshikawa, T. Facing Targets Sputtering Device. U.S. patent no. 5000834. March 1991.

[65] Rana, F. 2016. Semiconductor optoelectronics. [Online] Available : https://courses.cit.cornell.edu/ece533/Lectures/handout2.pdf.

[66] S.M. Sze, K.N. Kwok, Semiconductor Devices Physics and Technology. 3nd ed. United States of America: John Wiley & Sons (2007).

[67] Photodiode Technical Information (Hamamatsu). Available : https://www.hamamatsu.com/content/dam/hamamatsuphotonics/sites/documents/99_SALES_LIBRARY/ssd/si_pd_kspd9001e.pdf

[68] Buyukbas-Ulusan, A., Taşçıoğlu, İ., Tataroğlu, A., Yakuphanoğlu, F., and Altındal, S. 2019. “A comparative study on the electrical and dielectric properties of Al/Cd-doped ZnO/p-Si structures”, J. Mater. Sci.: Mater. Electron. 30 : 12122-12129.

[69] Friesen, G., Ozsar, M.E., and Dunlop, E.D. 2000. “Impedance model for CdTe solar cells exhibiting constant phase element behaviour”, Thin Solid Films 361-362 : 303-308.

[70] Sil, S., Datta, J., Das, M., Jana, R., Halder, S., Biswas, A., Sanyal, D., Ray, P. P. 2018. “Bias dependent conduction and relaxation mechanism study of Cu_5FeS_4 film and its significance in signal transport network”, J. Mater. Sci.: Mater. Electron. 29 : 5014-5024.

[71] Prakash, T., Ramasamy, S., and Murty, B. S. 2013. “Effect of DC bias on dielectric properties of nanocrystalline $CuAlO_2$”, Electron. Mater. Lett. 9 : 207-211.

[72] Melagiriyappa, E., Jayanna, H. S., and Chougule, B. K. 2008. “Dielectric behavior and ac electrical conductivity study of Sm^{3+} substituted Mg–Zn ferrites”, Mater. Chem. Phys. 112 : 68-73.

[73] Radoń, A., Łukowiec, D., Kremzer, M., Mikuła, J., and Włodarczyk, P. 2018. “Electrical conduction mechanism and dielectric properties of spherical shaped Fe_3O_4 nanoparticles synthesized by co-precipitation method”, Materials 11 : 735.

[74] Dey, A., Dhar, J., Sil, S., Jana, R., and Ray, P.P. 2018. “Bias voltage-dependent impedance spectroscopy analysis of hydrothermally synthesized ZnS nanoparticles”, J. Mater. Eng. Perform. 27 : 2727-2733.

[75] Ahmad, M., Rafiq, M. A., Imran, Z., Rasool, K., Shahid, R. N., Javed, Y., and Hasan, M. M. 2013. “Charge conduction and relaxation in MoS2 nanoflakes synthesized by simple solid state reaction”. J. Appl. Phys. 114 : 043710.

[76] Mattox, D.M. 2010. “Handbook of physical vapor deposition (PVD) processing.", Burlington : William Andrew (Imprint of Elsevier).

[77] Hill, C., Jones S., and Boys. D. 1988. "Rapid Thermal Annealing-Theory and Practice"(ed by Ronald A. Levy). Plenum Press, New York.

[78] Flamma, D. L., and Herb G. K. 1989. Plasma Etching || Plasma Etching Technology—An Overview. Amsterdam : Elsevier.

[79] Harry, J. E. 2013. Introduction to plasma technology: science, engineering, and applications. New Jersey : John Wiley & Sons.

[80] Yuan, Y. and Lee, T.R. 2013. Surface Science Techniques. Berlin : Springer-Verlag Berlin Heidelberg.

[81] Bormashenko, E. 2015. “Progress in understanding wetting transitions on rough surfaces.” Adv. Colloid Interface Sci. 222 : 92-103.

[82] Wenzel, R.N. 1936. “Resistance of solid surfaces to wetting by water.” Industrial & Engineering Chemistry. 28(8) : 988-994.

[83] Cassie, A.B.D. and Baxter, S. 1944. “Wettability of porous surfaces.” Transactions of the Faraday society. 40 : 546-551.

[84] Bunaciu, A.A., Udriştioiu, E.G., and Aboul-Enein, H.Y. 2015. “X-ray diffraction: instrumentation and applications.”, Crit. Rev. Anal. Chem. 45 : 289-299.

[85] Prysiazhnyi, V. 2012. Atmospheric pressure plasma treatment of metal surfaces by DCSBD plasma source: effects of plasma treatment and aging effect of plasma treated surfaces. Brno : Masaryk University.

[86] Joy, D.C., Bradbury, S. and Ford, B.J. 2019. Scanning electron microscope. [Online]. Available : https://www.britannica.com/technology/scanning electron-microscope.

[87] Zeng, C., Vitale-Sullivan, C. and Ma, X. 2017. “In situ atomic force microscopy studies on nucleation and self-assembly of biogenic and bio-inspired materials.”, Minerals 7 : 158.

[88] Mendes, B. 2020. Functionalization of Silicon Carbide (SiC) for Abrasive Filament Production. Lisbon : Instituto Superior Técnico.

[89] Sun, X., Li, L., Guo, Y., Zhao, H., Zhang, S., Yu, Y., Wu, D., Liu, H., Yu, M., Shi, D., Liu, Z., Zhou, M., Ren, L. and Fu, L. 2018. “Influences of organic component on mechanical property of cortical bone with different water content by nanoindentation.”, AIP Advances 8 : 035003.

[90] Shaban, M., Zkria, A., Yoshitake, T. 2020. “Temperature-dependent impedance spectra of nitrogen-doped ultrananocrystalline diamond films grown on Si substrates”, IEEE Access 9 : 896-904.

[91] Savvides, N. and Bell, T.J. 1993. “Hardness and elastic modulus of diamond and diamond-like carbon films”, Thin Solid Films 228 : 289–292.

[92] Özgen, Ö., 2011. “Plasma surface modification and characterization of PMMA films” Master of Science in Polymer Science and Technology Department, Middle East Technical University (Turkey).

[93] Shaban, M., Yoshitake, T. 2012. “Interface Properties of Nanocrystalline-$FeSi_2$/Crystalline-Si Near-Infrared Heterojunction Photodiodes,” IEEE J. Quantum Electron. 48 : 1432-1438.

[94] Shaban, M., Bayoumi, A. M., Farouk, D., Saleh, M. B., Yoshitake, T. 2016. “Evaluation of photovoltaic properties of nanocrystalline-$FeSi_2$/Si heterojunctions”, Solid State Electron. 123 : 111-118.

[95] Shaban, M., Nakashima, K., Yokoyama, W., Yoshitake, T. 2007. “Photovoltaic Properties of n-type β-$FeSi_2$/p-type Si Heterojunctions”, Jpn J Appl Phys. 46 : L667.

[96] Yang, X., Duan, B., Yang, Y., 2023. “Analysis of SiC/Si Heterojunction Band Energy and Interface State Characteristics for SiC/Si VDMOS”, Micromachines 14 : 1890.

[97] Sze, S.M., Li, Y., Ng, K.K. 2021. “Physics of semiconductor devices”, John wiley & sons.

[98] Sittimart, P., Duangrawa, A., Onsee, P., Teakchaicum, S., Nopparuchikun, A., Promros, N. “Interface state density and series resistance of n-type nanocrystalline $FeSi_2$/p-type Si heterojunctions formed by utilizing facing-target direct-current sputtering”, J. Nanosci. Nanotechnol. 18 : 1841-1846.

[99] Zhang, Y., Li, L., Yuan, S., Li, G., Zhang, W. 2013. “Electrical properties of the interfaces in bulk heterojunction organic solar cells investigated by electrochemical impedance spectroscopy”, Electrochim. Acta 109 : 221-225.

[100] Zkria, A., Abubakr, E., Sittimart, P., Yoshitake, T. 2020. “Analysis of electrical characteristics of Pd/n-nanocarbon/p-Si heterojunction diodes: By *C-V-f* and *G/ω-V-f*”, J. Nanomater. 2020 : 4917946.

[101] Singh, L., Kim, I. W., Woo, W. S., Sin, B. C., Lee, H., Lee, Y. 2015. “A novel low cost non-aqueous chemical route for giant dielectric constant $CaCu_3Ti_4O_{12}$ ceramic”, Solid State Sci. 43 : 35-45.

[102] Sil, S., Das, M., Datta, J., Halder, S., Ray, P. P. 2018. “Impedance spectroscopy study of hydrothermally synthesized nano-semiconducting bornite (Cu_5FeS_4)”, Mater. Today. 5 : 9948-9957.

[103] Cao, W., Gerhardt, R. 1990. “Calculation of various relaxation times and conductivity for a single dielectric relaxation process”, Solid State Ion. 42 : 213-221.

[104] Nivetha, R., Grace, A. N. 2019. “Manganese and zinc ferrite based graphene nanocomposites for electrochemical hydrogen evolution reaction”, J. Alloys Compd. 796 : 185-195.

[105] Chen, W., Zhu, W., Ke, C., Yang, Z., Wang, L., Chen, X. F., Tan, O. K. “Impedance spectroscopy and conductivity mechanism of $CoFe_2O_4$–$Pb(Zr_{0.53}Ti_{0.47})O_3$ composite thick films”, J. Alloys Compd. 508 : 141-146.

[106] Büyükbaş-Uluşan, A., Tataroğlu, A. 2020. “Impedance spectroscopy of Au/TiO_2/n-Si metal-insulator-semiconductor (MIS) capacitor”, Physica B: Condensed Matter 580 : 411945.

[107] Jiang, Y., Juarez-Perez, E. J., Ge, Q., Wang, S., Leyden, M. R., Ono, L. K., Raga, S. R., Hu, J., Qi, Y. 2016. "Post-annealing of MAPbI3 perovskite films with methylamine for efficient perovskite solar cells", Mater. Horiz. 3 : 548-555.

[108] Bhowmik, R. N., Panneer Muthuselvam, I. 2014. "Dielectric properties and signature of multi-ferroelectricity in Co_2FeO_4: A structurally single phased and bi-phased spinel oxide", J. Alloys Compd. 589 : 247-257.

[109] Ben Messaoud, N., Braik, M., Dridi, C., Ben Ali, M., Ali, A., Abbas, M. N., Errachid, A. 2016. "Optical, electrical and perchlorate sensing properties of a new CoPc derivative", Sensor Lett.14 : 928-937.

[110] Ožvold, M., Gašparík, V., & Dubnička, M. 1997. "The temperature dependence of the direct gap of β-$FeSi_2$ films", Thin Solid Films 295 : 147–150.

[111] Chandra Babu Naidu, K., Suresh Kumar, N., Ranjith Kumar, G., Naresh Kumar, S., 2019. "Temperature and frequency dependence of complex impedance parameters of microwave sintered NiMg ferrites", J. Aust. Ceram. 55 : 541-548.

[112] Jaiswal, S.K., Kumar, J. 2011. "On the sol–gel synthesis and structure, optical, magnetic and impedance behaviour of strontium cobaltite powder", J. Alloys. Compd. 509 : 3859–3865.

[113] Shehata, M.M. Abdelhady, K. 2018. "Temperature and frequency dependence of dielectric relaxation and AC electrical conductivity in p-Si/CuPc hybrid photodiode", Applied Physics A. 124 : 591.

[114] Yang, X., Duan, B. and Yang, Y., 2023. "Analysis of SiC/Si Heterojunction Band Energy and Interface State Characteristics for SiC/Si VDMOS", Micromachines, 14 : 1890.

[115] Hanefeld, M., Gruszka, P. and Huth, M., 2021. "AC conductivity and correlation effects in nano-granular Pt/C", Scientific reports 11 : 15163.

[116] Gonzales, C., Guerrero, A., Bisquert, J. 2022. "Transition from Capacitive to Inductive Hysteresis: A Neuron-Style Model to Correlate I-V Curves to Impedances of Metal Halide Perovskites", Journal of Physical Chemistry C 126 : 13560–13578.

[117] Bisquert, J., Guerrero, A. 2022. “Chemical Inductor”, J. Am. Chem. Soc. 144 : 5996–6009.

[118] Ebrahim, S. 2011. “Impedance spectroscopy and equivalent circuits of heterojunction solar cell based on n-Si/polyaniline base”, Polymer Science - Series A 53 : 1217–1226.

[119] Turcan, I., Lukacs, V.A., Curecheriu, L., Padurariu, L., Ciomaga, C.E., Airimioaei, M., Stoian, G., Lupu, N., Mitoseriu, L. 2018. “Microstructure and dielectric properties of Ag-BaTiO_3 composite ceramics”, J Eur Ceram Soc 38 : 5420–5429. https://doi.org/10.1016/j.jeurceramsoc.2018.08.002.

[120] Thurzo, I., Méndez, H., Zahn, D.R.T. 2005. “Dielectric relaxation in a hybrid Ag/DiMe-PTCDI/GaAs device”, J Non Cryst Solids 351 : 2003–2008.

[121] Wang, C., Krawthar, Z. 2007. “Dielectric resonators and filters”, IEEE Microwave Magazine 8 : 115–127.

[122] Kursumovic, A., Li, W.W., Cho, S., Curran, P.J., Tjhe, D.H.L., MacManus-Driscoll, J.L. 2020. “Lead-free relaxor thin films with huge energy density and low loss for high temperature applications”, Nano Energy. 71 : 104536.

[123] Darwish, A. A. A., El-Zaidia, E. F. M., El-Nahass, M. M., Hanafy, T. A., Al-Zubaidi, A. A. 2014. “Dielectric and electrical conductivity studies of bulk lead (II) oxide (PbO)”, J. Alloys Compd. 589 : 393-398.

[124] Santhosh, N. M., Upadhyay, K.K., Filipič, G., Zavašnik, J., de Fátima Montemor, M., Cvelbar, U. 2023. “Widening the limit of capacitance at high frequency for AC line-filtering applications using aqueous carbon-based supercapacitors”, Carbon N Y. 203 : 686–694.

[125] Liu, J., Galpaya, D., Notarianni, M., Yan, C., Motta, N. 2013. “Graphene-based thin film supercapacitor with graphene oxide as dielectric spacer”, Appl Phys Lett. 103 : 063108.

[126] Bakkali, H., Dominguez, M., Batlle, X., Labarta, A. 2016. “Universality of the electrical transport in granular metals”, Sci Rep. 6 : 29676.

[127] Barkhordari, A., Mashayekhi, H., Amiri, P., Altındal, Ş., Azizian-Kalandaragh, Y. 2023. “On the investigation of frequency-dependent dielectric features in Schottky barrier diodes (SBDs) with polymer interfacial layer doped by graphene and $ZnTiO_3$ nanostructures”, Applied Physics A. 129 : 249.

[128] Richman, E. K., Brezesinski, T., Tolbert, S. H. 2008. “Vertically oriented hexagonal mesoporous films formed through nanometre-scale epitaxy”, Nat. Mater. 79 : 712-717.

[129] Lakshantha, W.J., Dhoubhadel, M.S., Reinert, T., McDaniel, F.D., Rout, B. 2015. “Investigation of various phases of Fe-Si structures formed in Si by low energy Fe ion implantation”, Nucl. Instrum. Methods Phys Res B. 365 : 114–119.

[130] Baldwin, N.R., Ivey, D.G. 1995. “Iron Silicide Formation in Bulk Iron-Silicon Diffusion Couples”, Journal of phase equilibria. 16 : 300-307.

[131] Li, M., Chen, X., Guan, J., Wang, J., Liang, C. 2013. “Thermally induced phase transition and magnetic properties of Fe-$FeSi_2$ with core-shell structure”, Phys Status Solidi A. 210 : 2710–2715.

[132] Dusausoy, P.Y., Protas, J., Wandj, R., Roques, B. 1971. “Structure Cristalline du Disiliciure de Fer, $FeSi_2\beta$”, Acta Crystallogr B Struct. 27 : 1209-1218.

[133] Shen, B., He, Y., Wang, Z., Yu, L., Jiang, Y., Gao, H. 2020. “Reactive synthesis of porous FeSi intermetallic compound”, J Alloys Compd. 826 : 154227.

[134] Volochaev, M.N., Tarasov, I.A., Loginov, Y.Y., Cherkov, A.G., Kovalev, I. V., 2017. “The regularities of phase formation in $Fe_3Si(111)/Si(111)$ structure at vacuum annealing”, in: J Phys Conf Ser, Institute of Physics Publishing, 2017.

[135] Cassie, A.B.D., Baxter, S. 1944. “Wettability of porous surfaces”, Trans. Faraday Soc. 40 : 546–551.

[136] Samadi, A., Ni, T., Fontananova, E., Tang, G., Shon, H., Zhao, S. 2023 “Engineering antiwetting hydrophobic surfaces for membrane distillation: A review”, Desalination 563 : 116722.

[137] Li, Y., He, L., Zhang, X., Zhang, N., Tian, D. 2017 “External-field-induced gradient wetting for controllable liquid transport: from movement on the surface to penetration into the surface”, Adv. Mater. 29 : 1703802.

[138] Quek, S. S., Chooi, Z. H., Wu, Z., Zhang, Y. W., Srolovitz, D. J. 2016. “The inverse hall–petch relation in nanocrystalline metals: A discrete dislocation dynamics analysis”, J. Mech. Phys. Solids 88 : 252-266.

[139] Schiøtz, J., Vegge, T., Di Tolla, F.D., Jacobsen, K.W. 1999. “Atomic-scale simulations of the mechanical deformation of nanocrystalline metals”, Phys. Rev. B 60 : 11971–11983.

[140] Kramida, A., Yu. Ralchenko, J. Reader, NIST ASD Team, NIST Atomic Spectra Database (ver. 5.12). National Institute of Standards and Technology (2024), Gaithersburg, MD. Accessed January 31, 2025.

[141] Borwornpornmetee, N., Sittimart, P., Phatthanakun, R., Nakajima, H., Paosawatyanyong, B., Yoshitake, T., Promros, N. 2023. “Physical feature exploration of nanocrystalline $FeSi_2$ surface with argon plasma etching under varying power”, Vacuum 218 : 112588.

[142] Hofmann, S. 2013. “Auger-and X-Ray photoelectron spectroscopy in materials science: A user-oriented guide”, Springer Science & Business Media.

[143] Lynch, B., Neupane, S., Wiame, F., Seyeux, A., Maurice, V., Marcus, P. 2021 “An XPS and ToF-SIMS study of the passive film formed on a model FeCrNiMo stainless steel surface in aqueous media after thermal pre-oxidation at ultra-low oxygen pressure”, Appl. Surf. Sci. 554 : 149435.

[144] Saito, T., Yamamoto, H., Sasase, M., Nakanoya, T., Yamaguchi, K., Haraguchi, M., Hojou, K. 2002. “Surface chemical states and oxidation resistivity of ‘ecologically friendly’semiconductor (β-$FeSi_2$) thin films”, Thin Solid Films 415 : 138-142.

[145] Grundmeier, G., Stratmann, M. 1999. “Influence of oxygen and argon plasma treatments on the chemical structure and redox state of oxide covered iron”, Appl. Surf. Sci. 141 : 43-56.

[146] Fewster, P.F. 2023. “The Limits of X-ray Diffraction Theory, Crystals 13 : 521.

[147] Yin, Y., Sawin, H.H. 2008. “Surface roughening of silicon, thermal silicon dioxide, and low-k dielectric coral films in argon plasma”, J. Vac. Sci. Technol. A 26 : 151-160.

[148] Hoek, W., Mackus, A.J.M., Chittock, N.J., Knoops, H.C.M., de Jong, A.M. 2022. "Anisotropic plasma atomic layer etching of Al_2O_3 and HfO_2 using SF_6 and Ar plasma", Eindhoven University of Technology.

[149] Dias, N.F.L., Meijer, A.L., Jäckel, C.P., Frisch, A., Biermann, D., Tillmann, W. 2024. "Arc-enhanced glow discharge ion etching of WC-Co cemented carbide for improved PVD thin film adhesion and asymmetric cutting edge preparation of micro milling tools", Surf. Coat. Technol. 491 : 131166.

[150] Seo, K. Kim, M. 2015. "Re-derivation of Young's equation, Wenzel equation, and Cassie-Baxter equation based on energy minimization", In Surface energy. InTechOpen (2015).

[151] Hejazi, V., Moghadam, A.D., Rohatgi, P., Nosonovsky, M. 2014. "Beyond Wenzel and Cassie–Baxter: second-order effects on the wetting of rough surfaces", Langmuir 30 : 9423-9429.

[152] Terpilowski, K., Rymuszka, D. 2016. "Surface properties of glass plates activated by air, oxygen, nitrogen and argon plasma", Glass Phys. Chem. 42 : 535-541.

[153] Strnad, G., Chirila, N., Petrovan, C. and Russu, O. 2016. "Contact angle measurement on medical implant titanium based biomaterials.",Procedia Technology, 22 :.946-953.

[154] Kawakami, R., Niibe, M., Takeuchi, H., Konishi, M., Mori, Y., Shirahama, T., Yamada, T., Tominaga, K. 2013 "Surface damage of 6H–SiC originating from argon plasma irradiation, Nucl. Instrum", Methods Phys. Res., B 315 : 213-217.

Biography

Personal Information	
Full Name	Mr. Nattakorn Borworpornmetee
Date of Birth/ Age	January 12, 1997 / 27 years
Gender	Male
Nationality	Thai
Affiliation	Department of Physics, School of Science, King Mongkut's Institute of Technology Ladkrabang
Mobile Phone	+66 96-962-2673
E-mail	65056032@kmitl.ac.th
Home Address	1700/3 Mu 6, U-thong, U-thong, Suphan Buri 72160, Thailand
Keywords	Physics, Thin Solid Films, Solid State Physics, Laser and Plasma, Material and Device Characterizations

Academic Qualifications

B.Sc.	Applied Physics	King Mongkut's Institute of Technology Ladkrabang	2019
M.Sc.	Applied Physics	King Mongkut's Institute of Technology Ladkrabang	2022
Ph.D.	Applied Physics	King Mongkut's Institute of Technology Ladkrabang	

English Proficiencies

Format	Score	Date
TO-EFL (ITP)	603 (Listening B2, Structure B2, Reading C1)	15/09/2020
TO-EFL (ITP)	597 (Listening B2, Structure B2, Reading C1)	04/07/2024

Experiences and Achievements

- International research internship at Kyushu University: Nov, 2024-Feb, 2025
- International research internship at Kyushu University: Nov, 2022-Feb, 2023
- Research on dielectric barrier discharge plasma 2021-present
- KMITL Doctoral Scholarship: 2022
- Teaching assistant on MiniTab and DOE lab of Atomic Structure and Solid-State Physics Laboratory, academic year 2020
- Research Assistant and Teaching Assistant Scholarship: 2019
- International research internship at Kyushu University: Jan-Feb, 2019

Awards

Years	Awards	Organizations
2024	Gold Medal “Improvement of the Dielectric Barrier Discharge for the Elimination of Pathogenic Microorganisms and Airborne Dust”	Thailand New Gen Inventors Award 2024, Thailand, Feb 2-6, 2024
2022	Silver Medal “Design and Fabrication of Dielectric Barrier Discharge Plasma for Air Conditioning System Disinfection”	Thailand Research Expo 2022 Bangkok, Thailand, Aug 1-5, 2022
2022	Best presentation “Design and Characterization of Surface Dielectric Barrier Discharge Plasma System”	The 5th CRU-National Conference in Science and Technology Bangkok, Thailand, 16 June, 2022.
2022	First Place (Social Science, Humanity, and Management Group) “Warehouse Management”	KMITL Cooperative Education Exhibition 2021 Bangkok, Thailand, Jan 25, 2022
2022	First Place (Science and Technology Group) “Study and Improvement Epoxy Resin Bleed at Die Attach Operation for IC Copper Clip Package”	KMITL Cooperative Education Exhibition 2021 Bangkok, Thailand, Jan 25, 2022
2021	Silver Medal “Design and Construct of Air Purifier for Hospital Use”	Thailand Research Expo 2021 Bangkok, Thailand, June 27- July 1, 2021

2020	Best Poster Award “Nitrogen Plasma Etching of Indium Tin Oxide Nanorod Film Surface at Different Radio-Frequency Powers”	The 6th International Conference on Electronic Materials and Nanotechnology for Green Environment: **ENGE 2020** Ramada Plaza Jeju Hotel, Jeju, Korea, November 1-4, 2020
2019	Best Poster Award “Wetting, Structural and Surface Morphological Properties of C-doped β-$FeSi_2$ Thin Films Prepared via Radio-Frequency Magnetron Sputtering”	The 5th International Conference on Advanced Electromaterials: **ICAE 2019** Ramada Plaza Jeju Hotel, Jeju, Korea, November 5-8, 2019

Research publications

1. **Nattakorn Borwornpornmetee**, Thawichai Traiprom, Takafumi Kusaba, Phongsaphak Sittimart, Hiroshi Naragino, Boonchoat Paosawatyanyong, Tsuyoshi Yoshitake, and Nathaporn Promros. Modification of wetting and mechanical traits via rapid annealing under varying temperatures for β-$FeSi_2$, Journal of Materials Science (2025) 1-17. (Impact factor 3.500, Q1 Indexed in SCOPUS). https://doi.org/10.1007/s10853-024-10539-1
2. **N. Borwornpornmetee**, T. Traiprom, B. Paosawatyanyong, P. Sittimart, T. Yoshitake, and N. Promros. " Investigation into the impedance, dielectric behavior, and conductivity within *p*-silicon/*n*-nanocrystalline iron disilicide heterojunctions and equivalent circuit model in relation to temperature, Materials Science in Semiconductor Processing 188 (2025) 109184. (Impact factor 4.200, Q1 Indexed in WoS). https://doi.org/10.1016/j.mssp.2024.109184
3. **N. Borwornpornmetee**, T. Traiprom, B. Paosawatyanyong, P. Sittimart, T. Yoshitake, and N. Promros. Temperature Dependency of Impedance, Dielectric, and Conductivity Properties for Si-*p*/Beta-$FeSi_2$-*n* Heterostructures Created through Facing Target Sputtering, Materials Science in Semiconductor Processing 179 (2024) 108499. (Impact factor 4.100, Q1 Indexed in WoS). https://doi.org/10.1016/j.mssp.2024.108499

4. **Nattakorn Borwornpornmetee**, Thawichai Traiprom, Takafumi Kusaba, Phongsaphak Sittimart, Hiroshi Naragino, Boonchoat Paosawatyanyong, Tsuyoshi Yoshitake, and Nathaporn Promros. Wetting state and mechanical property alteration for the Fe_3Si films using rapid thermal annealing under various temperatures, Heliyon, Vol. 9 (2023) Article No. 12. (Impact factor 4.000, Q1) Indexed in SCOPUS.
5. **Nattakorn Borwornpornmetee**, Phongsaphak Sittimart, Rungrueang Phatthanakun, Hideki Nakajima, Boonchoat Paosawatyanyong, Tsuyoshi Yoshitake, and Nathaporn Promros. Physical feature exploration of nanocrystalline FeSi2 surface with argon plasma etching under varying power, Vacuum, Vol. 218 (2023) Article No. 112588. (Impact factor 4.000, Q1) Indexed in SCOPUS.
6. **Nattakorn Borwornpornmetee**, Chawapon Achirawongwat, Thawichai Traiprom, Bunpot Saekow, Supanit Porntheeraphat, Boonchoat Paosawatyanyong, Tsuyoshi Yoshitake, and Nathaporn Promros, Determining the Annealing Temperature Dependency of Wetting and Mechanical Features on Fe_3Si Films, Coatings, Vol. 13 (2023) Article No. 1328. (Impact factor 3.400, Q2) Indexed in Web of science.
7. **Nattakorn Borwornpornmetee**, Rawiwan Chaleawpong, Peerasil Charoenyuenyao, Adison Nopparuchikun, Boonchoat Paosawatyanyong, Phongsaphak Sittimart, Tsuyoshi Yoshitake, Nathaporn Promros, Impedance Characteristics under Different Voltages of n-β-$FeSi_2$/p-Si Heterojunctions Constructed via Facing Target Sputtering, Materials Science in Semiconductor Processing Vol. 165 (2023) Article No. 107671. (Impact factor 4.100, Q1) Indexed in Web of science.
8. **Nattakorn Borwornpornmetee**, Rawiwan Chaleawpong, Peerasil Charoenyuenyao, Adison Nopparuchikun, Boonchoat Paosawatyanyong, Phongsaphak Sittimart, Tsuyoshi Yoshitake, Nathaporn Promros, Reverse Bias Dependent Impedance and Dielectric Properties of Al/n-NC $FeSi_2$/p-Si/Pd Heterostructures Formed by Facing-Targets Sputtering, Materials Science in Semiconductor Processing Vol. 146 (2022) Article No. 106641. (Impact factor 3.927, Q1) Indexed in Web of science.

9. Peerasil Charoenyuenyao, Rawiwan Chaleawpong, **Nattakorn Borwornpornmetee**, Boonchoat Paosawatyanyong, Phongsaphak Sittimart, Tsuyoshi Yoshitake, Nathaporn Promros, Investigation of Morphological Surface Features, Wetting Behavior and Mechanical Traits under Various Substrate Temperatures for Beta Iron Disilicide Prepared via Facing-Targets Sputtering, Materials Science in Semiconductor Processing Vol. 146 (2022) Article No. 106604 (Impact factor 3.927, Q1) Indexed in Web of science.
10. **Nattakorn Borwornpornmetee**, Peerasil Charoenyuenyao, Rawiwan Chaleawpong, Boonchoat Paosawatyanyong, Rungrueang Phatthanakun, Phongsaphak Sittimart, Kazuki Aramaki, Takeru Hamasaki, Tsuyoshi Yoshitake, Nathaporn Promros, Physical Properties of Fe3Si Films Coated through Facing Targets Sputtering after Microwave Plasma Treatment, Coatings Vol. 11 (2021) Article No. 923. (Impact factor 2.881, Q2) Indexed in Web of science.
11. Rawiwan Chaleawpong, Nathaporn Promros, Peerasil Charoenyuenyao, Phongsaphak Sittimart, Pattarapol Sittisart, **Nattakorn Borwornpornmetee**, Yuki Tanaka, Tsuyoshi Yoshitake, Photovoltaic, Capacitance-Voltage, Conductance-Voltage, and Electrical Impedance Characteristics of p-Type Silicon/Intrinsic-Silicon/n-Type Semiconducting Iron Disilicide Heterostructures Built via Facing Target Direct-Current Sputtering, Thin Solid Films, Vol. 709 (2020) Article No. 138229. (Impact factor 2.183, Q3) Indexed in Web of science.
12. Peerasil Charoenyuenyao, Nathaporn Promros, Rawiwan Chaleawpong, **Nattakorn Borwornpornmetee**, Pattarapol Sittisart, Yuki Tanaka, Tsuyoshi Yoshitake, Wettability, Morphological and Wetting Properties of Semiconducting Beta and Nanocrystalline Iron Disilicide Formed via Radio Frequency Magnetron Sputtering, Thin Solid Films, Vol. 709 (2020) Article No. 138248. (Impact factor 2.183, Q3) Indexed in Web of science.

13. Peerasil Charoenyuenyao, Nathaporn Promros, Rawiwan Chaleawpong, Pitoon Noymaliwan, **Nattakorn Borwornpornmetee**, Surachart Kamoldilok, Supanit Porntheeraphat, Bunpot Saekow, Tanapoj Chaikeeree, Benjarong Samransuksamer, Peerapong Nuchuay, Chanunthorn Chananonnawathorn, Saksorn Limwichean, Mati Horprathum, Pitak Eiamchai, Viyapol Patthanasettakul, Influence of an Annealing Temperature in a Vacuum Atmosphere on the Physical Properties of Indium Tin Oxide Nanorod Films, Journal of Nanoscience and Nanotechnology, Vol. 20 (2020) 5006-5013. (Impact factor 1.134, Q4) Indexed in Web of science.
14. Peerasil Charoenyuenyao, Nathaporn Promros, Rawiwan Chaleawpong, **Nattakorn Borwornpornmetee**, Pattarapol Sittisart, Yuki Tanaka, Tsuyoshi Yoshitake, Wettability, Surface Morphology and Structural Properties of β-$FeSi_2$ Films Manufactured through Usage of Radio-Frequency Magnetron Sputtering, Journal of Nanoscience and Nanotechnology, Vol. 20 (2020) 5075-5081. (Impact factor 1.134, Q4) Indexed in Web of science.
15. Pattarapol Sittisart, Nathaporn Promros, Rawiwan Chaleawpong, Peerasil Charoenyuenyao, **Nattakorn Borwornpornmetee**, Yuki Tanaka, Tsuyoshi Yoshitake, Light Detection and Carrier Transportation Mechanism in p-Type Si/n-Type Nanocrystalline $FeSi_2$ Heterojunctions produced via Radio-Frequency Magnetron Sputtering, Journal of Nanoscience and Nanotechnology, Vol. 20 (2020) 5082-5088. (Impact factor 1.134, Q4) Indexed in Web of science.

Supplementary

S.1 *I-V* inspection

Figure S.1 displays the source measure unit (Keithley, model: 2400 Series), which was used to perform the *I-V* inspections. The rectifying behaviour and near-infrared (NIR) photoresponse of the n-β-FeSi$_2$/p-Si and n-NC-FeSi$_2$/p-Si heterojunction devices were evaluated under both dark and illuminated conditions. *I-V* data for both device types were collected in the dark environment within a bias voltage span of -1 V to 0 V at room temperature to confirm their rectifying characteristics. These dark measurements also served as the basis for extracting diode parameters using thermionic emission (TE), Cheung’s method, and Norde’s technique. Additionally, at lower temperatures, the dark *J-V* curves were analysed using the TE and Norde models to further examine the temperature dependence of the diode parameters.

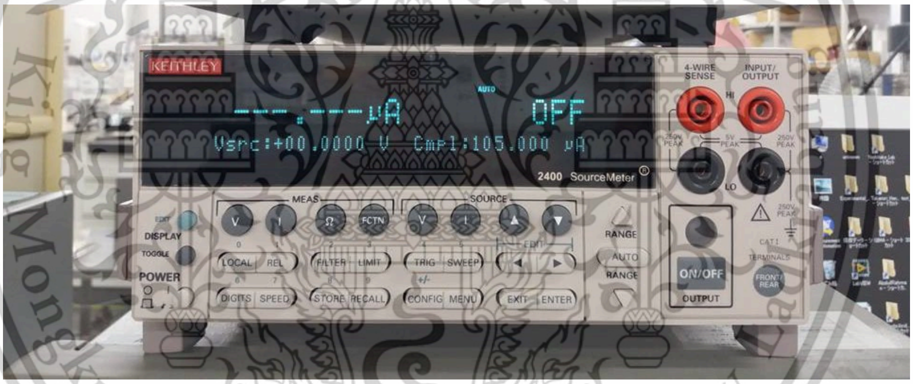

Figure S.1 Keithley 2400 Series Source Measure Unit Instrument.

S.2 Dark and illuminated *J-V* profiles at room temperature of the NC-FeSi$_2$/Si

Figure S.2 shows the *J–V* characteristics of the fabricated heterostructure (device area 1 mm^2) measured at room temperature in the dark under forward and reverse bias (–1 V to 1 V). It can be seen that the heterojunction exhibits a clear rectifying behavior. At 0 V, a leakage current density of 3.0×10^{-4} A cm^{-2} was observed, and this value increased to 1.8×10^{-2} A cm^{-2} when the reverse bias was applied up to –1 V. Such an increase in leakage current under reverse bias may be due to the accumulation of interface states at the NC-FeSi$_2$/Si interface, which promotes the recombination and tunneling of charge carriers. In addition, the high carrier concentration from the nanocrystalline $FeSi_2$ layer may also contribute to the increase in leakage current.

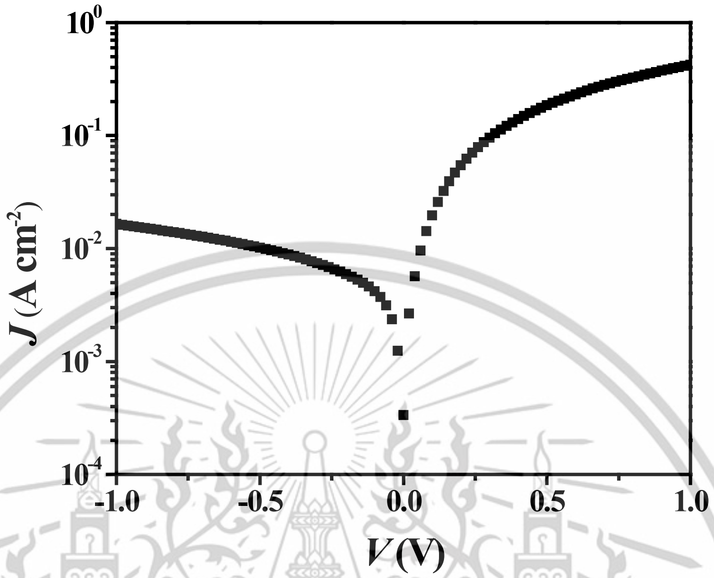

Figure S.2 A plot of *J* against bias *V* from 1 to -1 V for the formed heterostructures.

Figure S.3 displays the dark measured *J-V* curve in the positive region of the voltage for the formed heterostructures. Based on the thermionic emission theory, the linearity of *J* values when voltage ≤ 0.20 V could be explained through the diode equation as follows:

$$J_0 = \frac{J}{\left[\exp\left(\frac{Vq}{Tkn}\right) - 1\right]} \tag{S.1}$$

where J_0 and *J* refer to the density of saturation current and density of the current, while *V*, *q*, *T*, and *k* are the biased voltage, electron charge, temperature, and Boltzmann constant, respectively. Per Eq. (S.1) in the circumstance of voltage value beyond $3kT/q$, the ideality factor (*n*) could be computed using the linear slope of the linear part of the ln*J*-*V* plot through the following equation:

$$n = \frac{dV}{d(\ln(J))} \times \frac{q}{Tk} = \frac{1}{\text{slope}} \times \frac{q}{Tk} \qquad \text{(S.2)}$$

In the bias voltage range of 0.04 to 0.16 V, the ideality factor n calculated using equation (S.2) was approximately 2.45. This relatively high *n* value indicates that recombination occurs not only at the junction interface but also inside the film, and that tunneling effects may also be involved. This phenomenon is thought to be caused by grain boundaries in the nanocrystalline film, which form deep trap levels in the energy band.

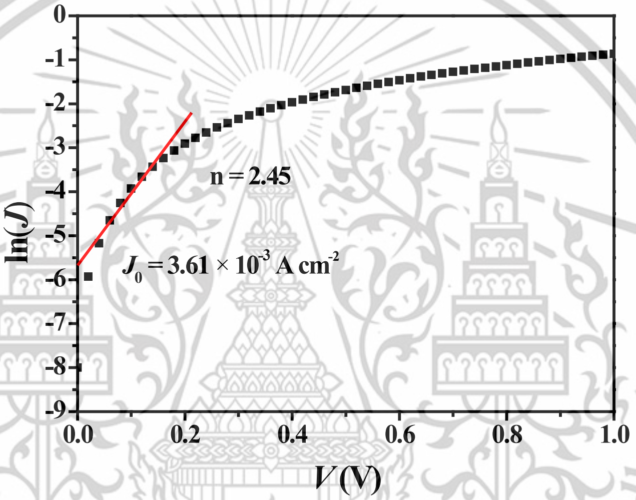

Figure S.3 Dark measured ln*J* –*V* curve on the positive voltage region of the created heterostructures.

The y-axis interception of the linear part on the *J* –*V* plot can be utilized for J_0 estimation, where it indicates that the heterostructures possess J_0 of 3.61 x 10^{-3} Acm^{-2}. When the value of J_0 is calculated, the barrier height (ϕ_b) can be estimated by Eq. (S.3), where the ϕ_b of the created heterostructures was estimated to be 0.55 eV.

$$\phi_b = -\frac{kT}{q} \ln\left(\frac{J_0}{A^* T^2}\right) \qquad \text{(S.3)}$$

where *A** is the effective Richardson's constant.

Further, the values of R_s and ϕ_b can be calculated through Norde's method. This method can be expressed as the relationship below:

$$F(V) = \frac{V}{\gamma} - \frac{kT}{q}\ln\left(\frac{J}{A^{*}T^{2}}\right) \tag{S.4}$$

where *F(V)* is the function of the biased voltage, and γ is the first integer with a value greater than that of the *n* value.

When the lowest point of *F(V)* is acquired, the ϕ_b and R_s values can be determined through the following equations:

$$\phi_b = F(V_0) + \frac{V_0}{\gamma} - \frac{kT}{q} \tag{S.5}$$

where $F(V_0)$ denotes the lowest point of *F(V)*, and V_0 denotes the biased voltage corresponding to the $F(V_0)$. *Rs* can be extracted as:

$$R_s = (\gamma - n)\frac{kT}{qJ_{\min}A} \tag{S.6}$$

where J_{min} is the current density corresponding to $F(V_0)$, and *A* is the junction area.

Figure S.4 shows the plot between *F*(*V*) and voltage for the heterostructures formed at room temperature. From this plot, the $F(V_0)$ value was 0.54 at the V_0 of 0.12 V. From the $F(V_0)$ value, the ϕ_b value was calculated through Eq. (4.5) and was found to be 0.57 eV. This acquired ϕ_b is concordant with that appraised by Eq. (S.3). In addition, the evaluation of R_s using Eq. (S.6) revealed a value of approximately 42.42 Ω. This R_s value might originate in the R_s of the heterostructures occurring at the neutral regimes together with ohmic contact.

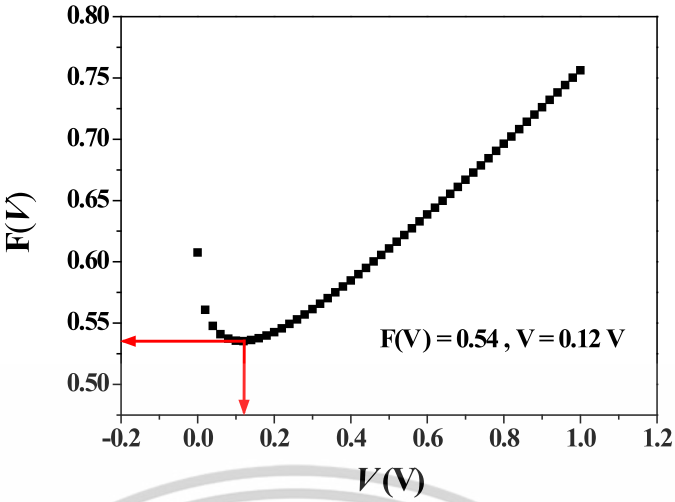

Figure S.4 A plot of *F*(*V*) versus voltage for the heterostructures formed at room temperature.

S.3 Dark and illuminated *I-V* profiles at room temperature of the β-FeSi$_2$/Si

In this study, both sides made Ohmic contact, ideally to allow the current to pass from both sides of the β-FeSi$_2$/Si heterojunction devices. Pd was applied on the Si side due to its ϕ_M of 5.12 which is higher than χ of 4.05 eV of *p*-type Si. Meanwhile, Al with ϕ_M of 4.10 eV is the closest possible value to χ of 4.16 eV for *n*-type β-FeSi$_2$ among other conventional metal electrodes. The quality of Al and Pd electrodes was demonstrated using *I-V* characteristics, separately measured at each side of the Ohmic contact. Fig. 4.10 reveals the *I-V* curve of the Al/ β-FeSi$_2$ and Pd/*p*-Si Ohmic contact. The results for both Ohmic contacts show a straight line with very low current values, proving that the Pd and Al electrodes were properly created.

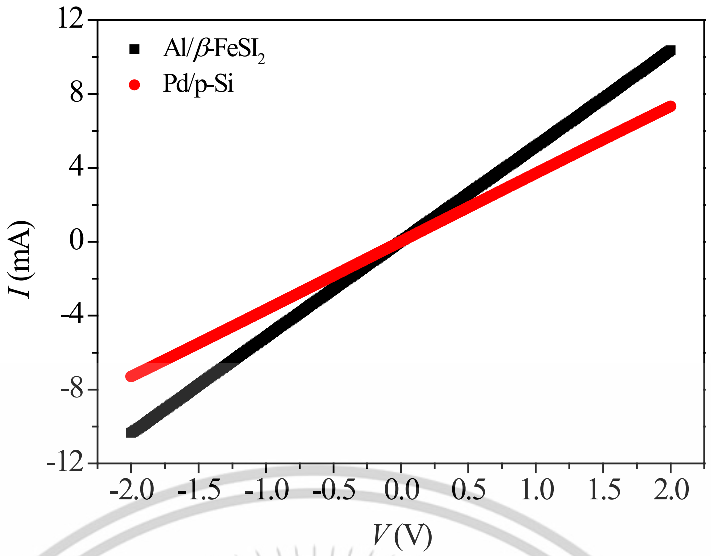

Fig. S.5 The *I-V* measurements of the Al/ β-$FeSi_2$ and Pd/*p*-Si Ohmic contact.

S.4 Table of fitted values

Table S.1 Software-fitted circuit parameters of *p*-Si/*n*-NC-$FeSi_2$ heterojunctions

V (V)	R_s (Ω)	R_g (Ω)	R_{gb} (Ω)	R_j (Ω)	CPE_g (pF)	CPE_{gb} (nF)	CPE_j (pF)
-1	196.200	6485.000	3588.000	8732.000	277.000	1.056	205.700
-0.9	173.800	3762.000	2133.000	5198.000	320.500	2.124	235.800
-0.8	157.100	2512.000	1445.000	3610.000	417.000	3.230	329.000
-0.7	139.600	1993.000	1098.000	2769.000	451.000	4.080	384.900
-0.6	126.700	1701.000	912.000	2298.000	547.400	4.877	456.100
-0.5	115.500	1490.000	773.840	2032.000	665.700	5.839	541.100
-0.4	108.400	1303.000	703.000	1892.000	802.600	7.094	660.300
-0.3	96.600	1202.000	663.000	1730.000	957.700	8.773	812.700
-0.2	90.290	1112.000	620.500	1591.000	1048.500	10.040	993.000
-0.1	84.580	1045.000	576.000	1497.000	1178.000	11.250	1042.000
0	78.800	988.000	557.000	1429.000	1379.000	12.230	1133.000

Table S.2 Software-fitted circuit parameters of p-Si/n-β-FeSi$_2$ heterojunctions simulated via EC-Lab Software

V (V)	R_s (Ω)	R_g (Ω)	R_{gb} (Ω)	R_j (Ω)	CPE$_g$ (nF)	CPE$_{gb}$ (nF)	CPE$_j$ (nF)
-1.0	84.160	1467.000	428.000	2101.000	11.840	43.600	4.843
-0.9	75.990	798.000	247.500	1279.000	12.200	43.700	4.944
-0.8	65.200	486.312	141.036	871.056	12.630	43.780	5.000
-0.7	58.600	344.088	102.060	641.520	13.000	44.440	5.042
-0.6	55.500	271.635	81.445	522.795	13.890	45.280	5.104
-0.5	53.270	242.312	72.694	437.027	15.870	47.620	5.260
-0.4	51.830	230.065	68.183	380.653	18.600	51.670	5.556
-0.3	50.580	219.132	64.928	340.872	22.300	57.610	6.348
-0.2	49.520	209.456	62.442	316.160	26.950	65.800	7.440
-0.1	48.600	200.720	60.602	301.080	32.350	76.900	8.920
0	47.720	192.372	58.843	290.444	38.630	82.310	9.544
0.1	46.970	184.850	57.304	280.972	42.350	84.700	10.783
0.2	46.340	178.066	55.964	272.550	44.600	90.920	11.487
0.3	45.990	172.752	55.065	266.326	47.980	95.960	11.993
0.4	45.500	166.850	53.960	259.150	53.950	107.900	12.983
0.5	45.200	161.920	53.152	253.440	58.430	116.860	14.477
0.6	45.100	157.950	52.650	249.210	60.230	124.460	15.743
0.7	45.000	139.000	42.150	225.000	61.190	132.380	17.063
0.8	44.900	130.100	41.650	220.800	63.430	149.100	19.480
0.9	44.900	126.580	41.303	217.320	72.450	176.300	23.030
1.0	44.870	122.967	40.910	213.629	80.160	198.500	25.330

Table S.3 Fitted parameters based on Jonscher's power law under different applied voltage for *p*-Si/*n*-NC-FeSi$_2$

V (V)	σ_{DC} (S m^{-1})	S	A
-1.0	2.67×10^{-5}	2.79	6.60×10^{-22}
-0.9	4.60×10^{-5}	3.06	3.06×10^{-22}
-0.8	6.75×10^{-5}	3.04	3.04×10^{-23}
-0.7	8.54×10^{-5}	1.93	1.17×10^{-16}
-0.6	9.99×10^{-5}	1.31	8.95×10^{-13}
-0.5	1.14×10^{-4}	1.22	3.88×10^{-12}
-0.4	1.26×10^{-4}	1.22	4.23×10^{-12}
-0.3	1.37×10^{-4}	1.19	5.73×10^{-12}
-0.2	1.47×10^{-4}	1.18	6.58×10^{-12}
-0.1	1.57×10^{-4}	1.30	1.35×10^{-12}
0	1.66×10^{-4}	1.39	4.32×10^{-13}

Table S.4 The fitted σ_{DC} and S parameters based on the Jonscher's power law under various applied voltage for p-Si/n-β-FeSi$_2$

V (V)	σ_{DC} (S cm^{-1})	A	S
-1.0	9.49×10^{-3}	3.15×10^{-13}	1.61
-0.9	1.58×10^{-2}	3.56×10^{-13}	1.58
-0.8	2.22×10^{-2}	4.79×10^{-13}	1.55
-0.7	2.80×10^{-2}	7.91×10^{-13}	1.52
-0.6	3.35×10^{-2}	1.35×10^{-12}	1.48
-0.5	3.77×10^{-2}	2.29×10^{-12}	1.44
-0.4	4.39×10^{-2}	3.83×10^{-12}	1.41
-0.3	5.08×10^{-2}	4.84×10^{-12}	1.38
-0.2	5.53×10^{-2}	6.90×10^{-12}	1.37
-0.1	5.96×10^{-2}	8.77×10^{-12}	1.36
0	6.29×10^{-2}	1.53×10^{-11}	1.35
0.1	6.64×10^{-2}	2.01×10^{-11}	1.33
0.2	7.00×10^{-2}	2.29×10^{-11}	1.32
0.3	7.35×10^{-2}	2.9×10^{-11}	1.31
0.4	7.67×10^{-2}	3.27×10^{-11}	1.30
0.5	7.98×10^{-2}	3.91×10^{-11}	1.29
0.6	8.28×10^{-2}	3.94×10^{-11}	1.29
0.7	8.52×10^{-2}	4.23×10^{-11}	1.28
0.8	8.68×10^{-2}	5.71×10^{-11}	1.26
0.9	8.82×10^{-2}	7.22×10^{-11}	1.25
1.0	8.87×10^{-2}	8.75×10^{-11}	1.23

Table S.5 Fitted circuit parameters for the *p*-Si/*n*-NC-FeSi$_2$ heterojunctions under various temperatures

T (K)	R_s (Ω)	R_g (Ω)	R_{gb} (Ω)	R_j (Ω)	CPE$_g$ (pF)	CPE$_{gb}$ (nF)	CPE$_j$ (pF)
160	145.100	5571.000	2512.500	7150.200	250.900	1.800	175.200
180	125.120	4201.600	1964.800	5490.800	291.600	2.500	201.000
200	118.640	2986.400	1453.600	3844.100	365.000	2.968	238.600
220	105.450	2413.400	1051.000	3215.400	452.100	3.330	255.700
240	92.580	1923.400	723.100	2611.100	555.000	3.900	300.200
260	81.500	1648.500	578.900	2261.700	658.400	5.200	406.600
280	74.600	1272.400	460.500	1833.300	721.000	5.970	499.900
300	71.300	971.200	352.100	1292.500	875.000	8.330	670.000
320	70.320	740.500	286.600	901.200	1134.500	12.200	875.000
340	65.800	544.800	168.200	712.200	1340.800	15.100	1090.000
360	58.640	435.000	128.400	599.800	1791.200	20.020	1382.000
380	49.420	325.200	83.600	487.400	2241.600	24.840	1674.000
400	44.850	244.800	53.600	351.100	2475.000	31.200	2045.000

Table S.6 Fitted circuit parameters for the p-Si/n-β-$FeSi_2$ heterostructures under various temperatures

T (K)	R_s (Ω)	CPE (nF)	n	R_p (Ω)	R_L (Ω)	L (H)
160	21.000	9.140	0.970	46417.000	1190000.000	0.270
180	21.600	9.640	0.940	38336.000	745567.000	0.440
200	22.000	1.110	0.960	29558.000	135105.000	0.240
220	22.200	12.100	0.990	29349.000	86082.000	0.290
240	24.200	12.400	0.990	17714.000	35105.000	0.770
260	24.500	15.800	0.980	7329.000	21866.000	0.550
280	25.100	16.700	0.970	2249.000	19696.000	0.650
300	25.900	16.800	0.930	578.100	17514.000	0.620
320	26.900	19.100	0.990	186.400	15071.000	0.840
340	28.700	22.700	0.990	153.800	13266.000	1.020
360	33.500	23.900	0.980	126.600	11270.000	1.020
380	34.600	42.400	1.000	75.430	5779.000	1.480
400	49.600	83.700	1.000	19.040	2724.000	1.080

Table S.7 The values of σ_{DC}, *S,* and *A* from Jonscher's fitting on σ_{AC}-*f* plots under varying temperatures

T (K)	σ_{DC} (× 10^{-5} S cm^{-1})	*A* (× 10^{-14})	*S*
160	1.82	13600	1
180	3.04	20100	0.98
200	3.87	6680	1.06
220	4.56	8090	1.04
240	5.06	1190	1.18
260	6.4	3910	1.1
280	8.43	546	1.24
300	11.4	209	1.32
320	14.5	924	1.22
340	18.7	98.4	1.38
360	27.0	327	1.29
380	35.1	200	1.34
400	45.4	7.34	1.57

Table S.8 The σ_{DC}, S, and A parameters of p-Si/n-β-FeSi$_2$ heterojunctions under different temperatures fiitted from Jonscher's law

T (K)	σ_{DC} ($\times 10^{-4}$ S cm^{-1})	S	A ($\times 10^{-13}$)
160	6.47	0.89	15600
180	8.42	0.94	9410
200	11	1.01	4180
220	14.7	1.06	1700
240	21.1	1.17	402
260	44.6	1.19	851
280	153	1.23	551
300	621	1.36	188
320	1570	1.58	6.60
340	1860	1.62	4.33
360	2210	1.62	4.57
380	3230	1.64	3.75
400	6340	1.65	4.44

S.5 Contact angle image

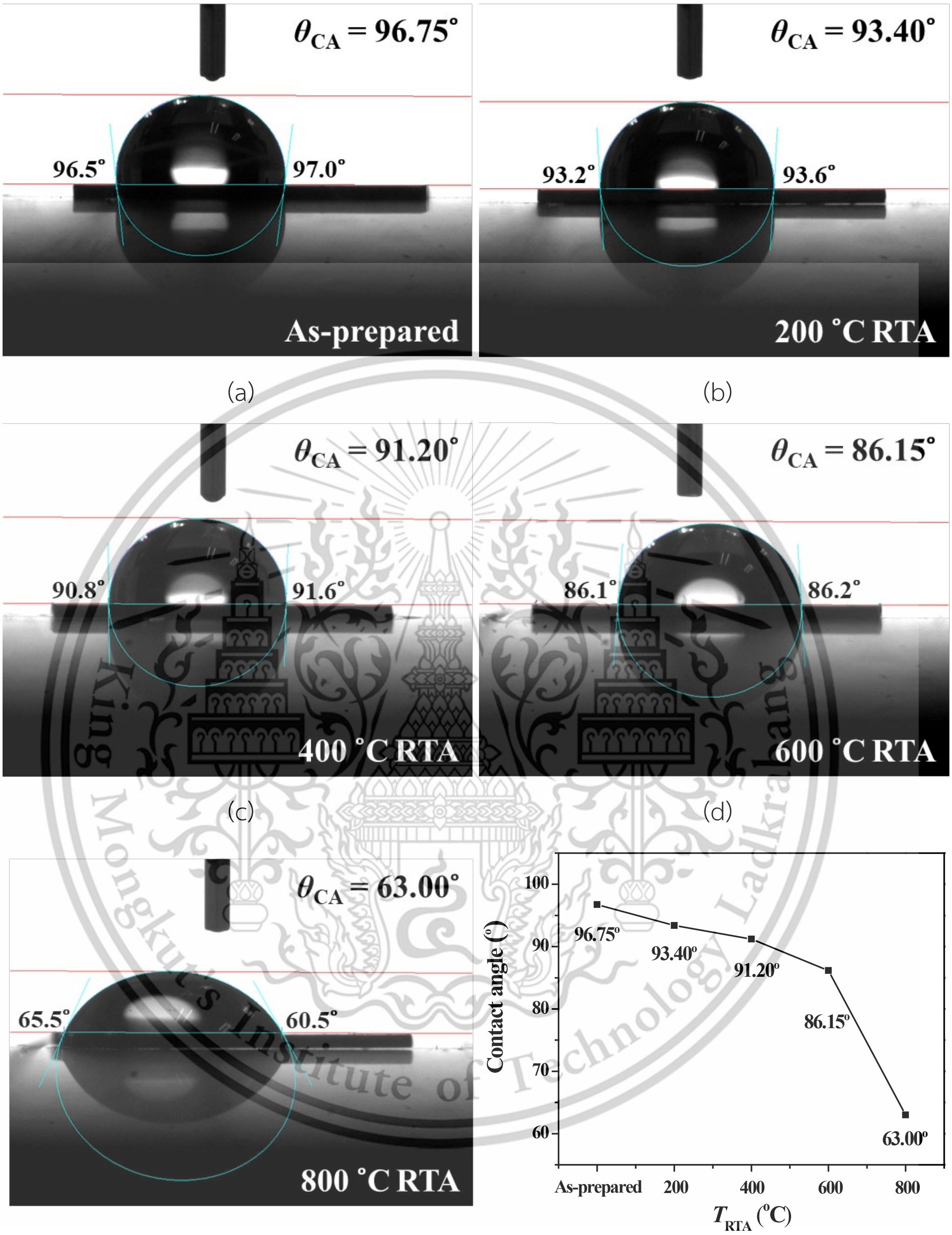

(a) (b)

(c) (d)

(e) (f)

Figure S.6 The θ_{CA} results using a deionized water testing solution for β-$FeSi_2$ layers as-created and after being rapidly annealed under different T_{RTA} ranges from 200 °C to 800 °C.

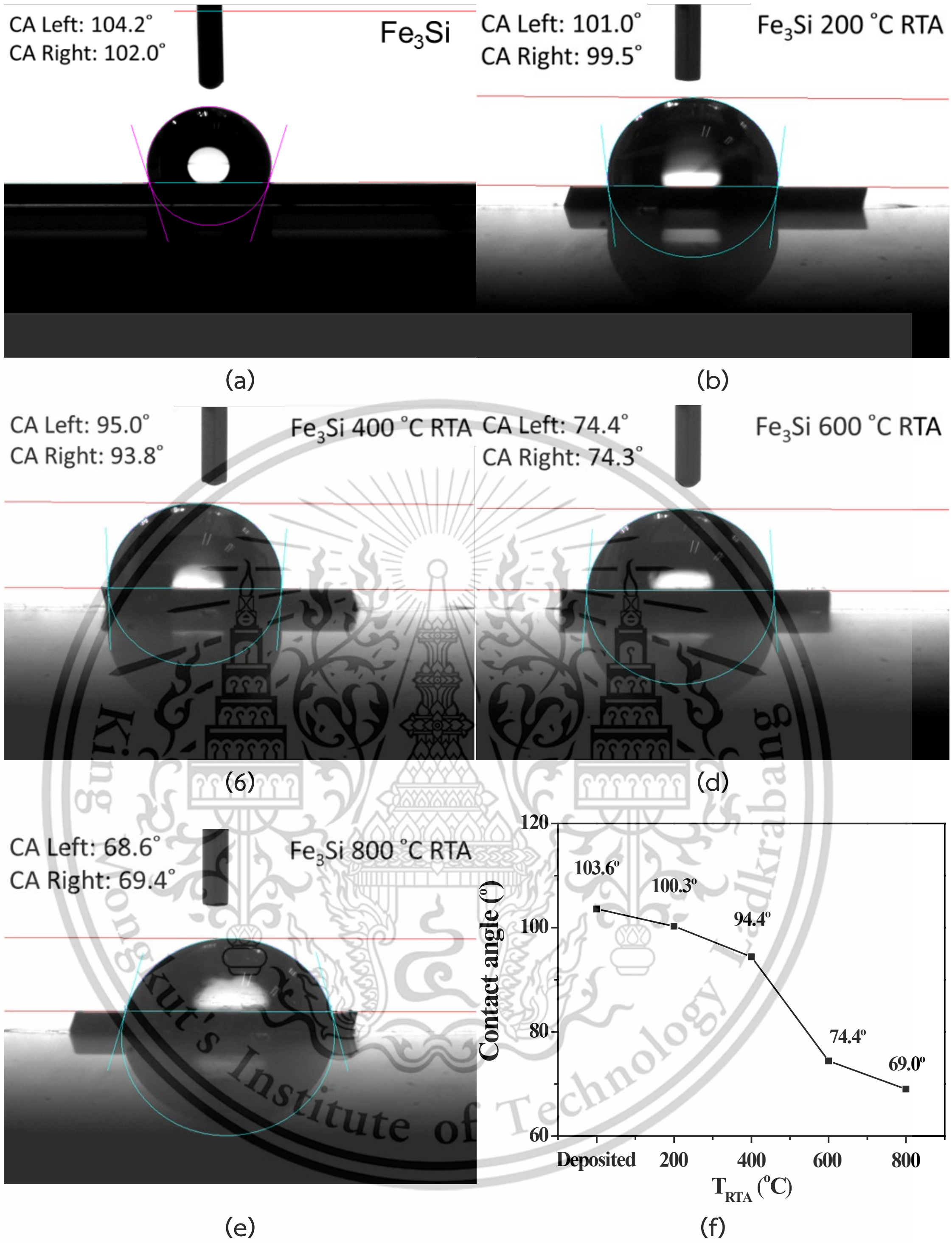

Figure S.7 (a) Contact angle images of the DWN droplet on as-created film's surfaces and film's surfaces after RTA at different T_{RTA} values of (b) 200, (c) 400, (d) 600, and (e) 800 °C and 6f-the trend line between contact angles and T_{RTA}.

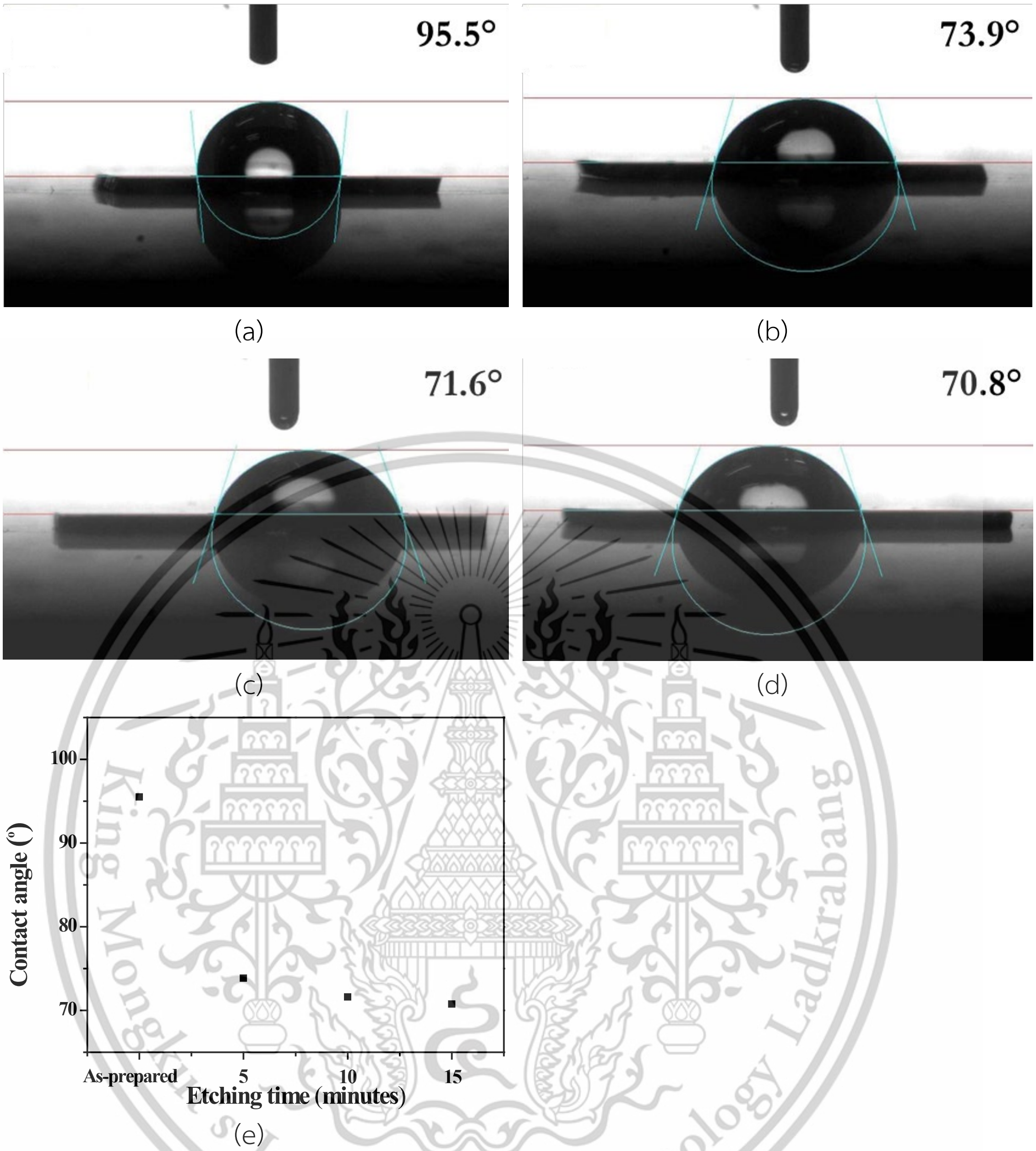

(a) (b)

(c) (d)

(e)

Figure S.8 Images of the surface contact between DI water and β-$FeSi_2$ films in the case of (a) as-coated β-$FeSi_2$ films, (b) after 5 minutes of etching, (c) after 10 minutes of etching, and (d) after 15 minutes of etching.

S.6 Load-depth plot

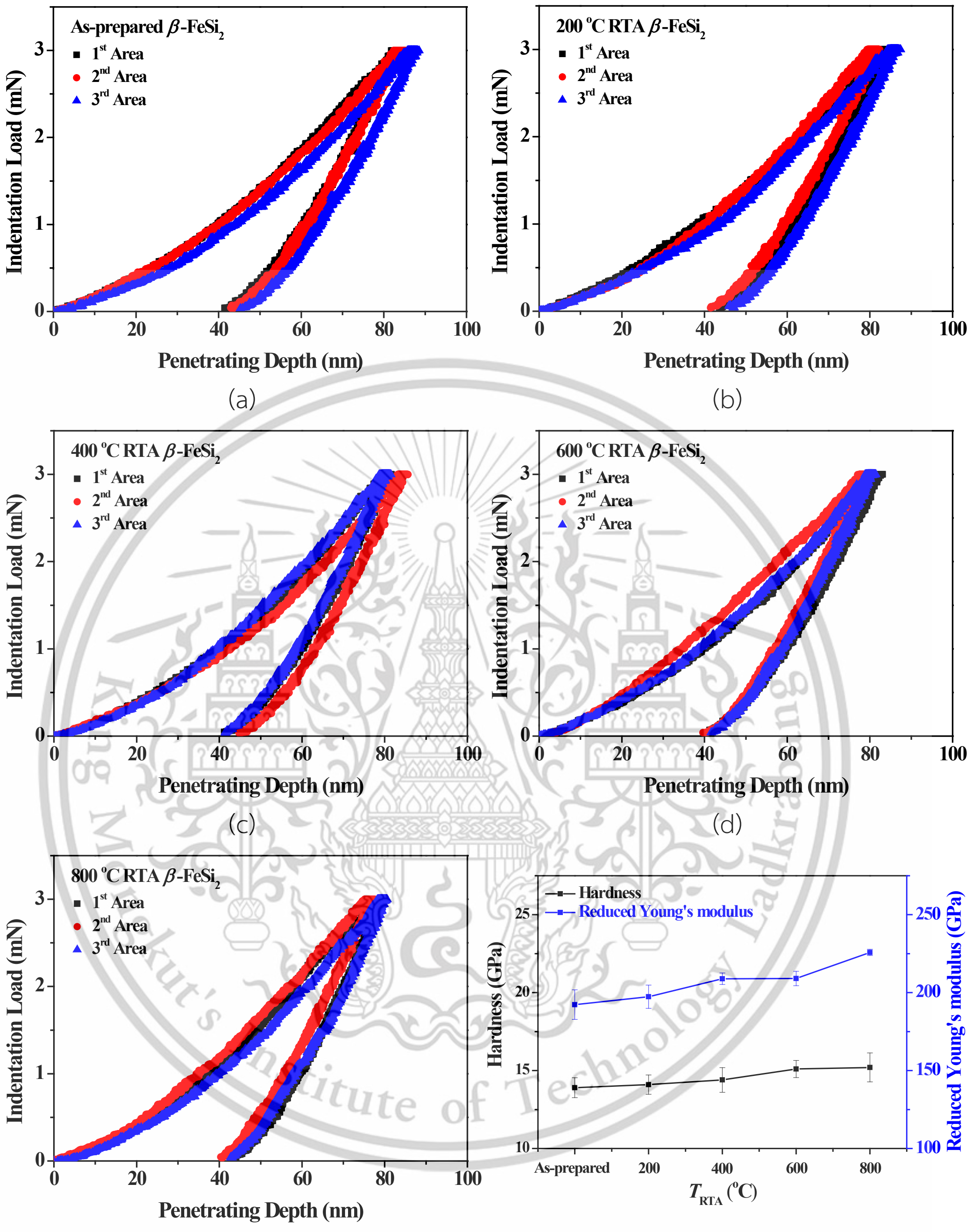

(a) (b) (c) (d) (e) (f)

Figure S.9 (a-e) Mechanical properties presented in the form of an indentation load and penetrating depth plot of β-FeSi$_2$ layers as-prepared and after being rapidly annealed at different T_{RTA} of 200 °C to 800 °C. (f) Trend of hardness and reduced Young's modulus observed through different T_{RTA} values.

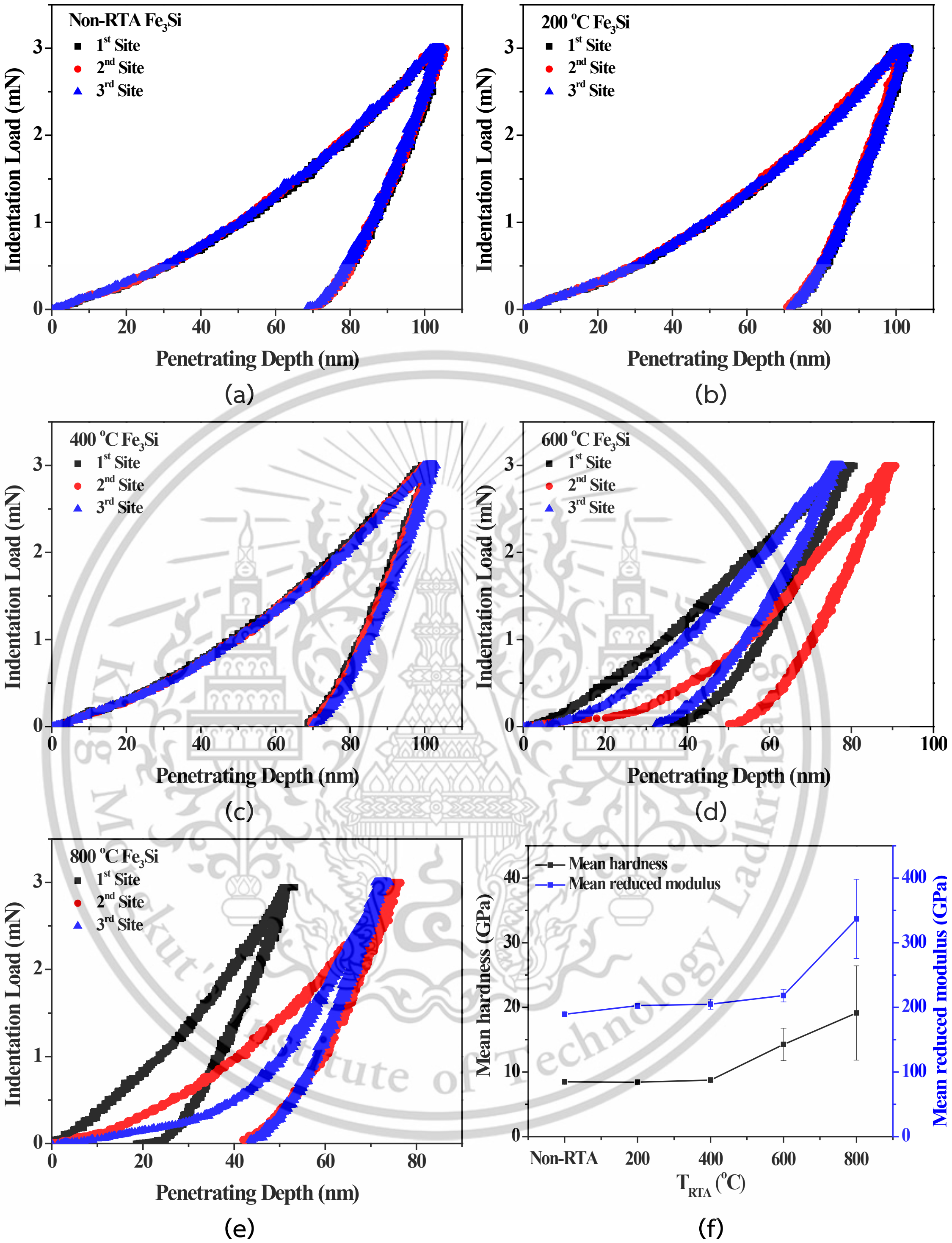

(a) (b) (c) (d) (e) (f)

Figure S.10 Penetrate depth versus load of (a) pre-RTA and (b-e) post-RTA Fe_3Si films at 200 °C, 400 °C, 600 °C, and 800 °C, in order. The Figure (f) is plot of derived H and E_r results against T_{RTA}.

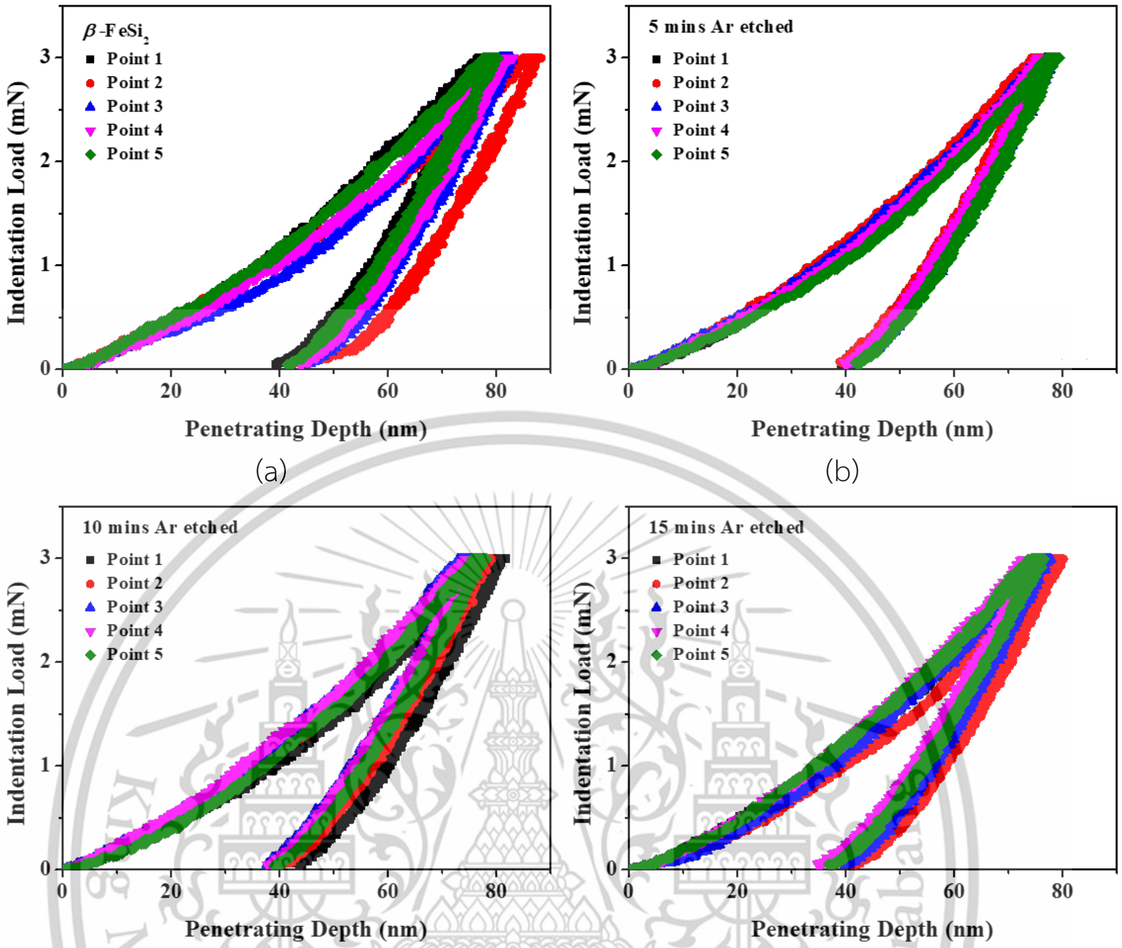

(a) (b) (c) (d)

Figure S.11 Load-depth plots for each β-FeSi$_2$ film in the case of (a) as-coated β-FeSi$_2$ films, (b) after 5 minutes of etching, (c) after 10 minutes of etching, and (d) after 15 minutes of etching.